DESIGN PROCESS OF AN ADDITIVELY MANUFACTURED REGENERATIVELY COOLED ROCKET ENGINE FOR LAB USE

A Thesis

presented to

the Faculty of California Polytechnic State University,

San Luis Obispo

In Partial Fulfillment

Of the Requirements for the Degree

Master of Science in Aerospace Engineering

by

Alec Matthew Fisher Bluhm

September 2021

COMMITTEE MEMBERSHIP

TITLE: Using Additive Manufacturing to Produce a Regeneratively Cooled Rocket Engine for Laboratory Use

AUTHOR: Alec Matthew Fisher Bluhm

DATE SUBMITTED: August 2021

COMMITTEE CHAIR: Dianne DeTurris, Ph.D.
Professor of Aerospace Engineering

COMMITTEE MEMBER: Arnold Deffo, Ph.D.
Professor of Aerospace Engineering

COMMITTEE MEMBER: Amelia Greig, Ph.D.
Professor of Aerospace Engineering

COMMITTEE MEMBER: Elias Wilson, MS
Director of Engineering from Exquadrum, Inc.
Adelanto, California

Abstract

A step-by-step engine design process for a liquid rocket engine is laid out alongside an example engine that aims to provide a low-cost option for universities looking to expand their propulsion labs. There is currently an absence of an affordable way to teach students about additive manufacturing and regenerative cooling in a lab setting. Developing an engine that is low cost, easy to operate, easy to maintain, uses non-hazardous propellants and can output useful data for analysis in a lab is of the utmost importance for teaching emerging technologies in chemical propulsion. An in-depth theoretical analysis has been implemented alongside a software suite to develop the most realistic model without running physical tests. Propellants of nitrous oxide and an ethanol water mixture were used in the development of the modeling of a characteristic length range for a 100 pounds force engine. This resulted in an engine chamber that implemented additive manufacturing to use regenerative, film and dump cooling that could be completely assembled with supporting plumbing for just over 15,000 dollars. The engine, as designed, serves as a ready to print, preliminary design for fine tuning of the system. This should open doors to universities looking to expand their propulsion ground testing capabilities. In addition, there is little to no published data on characteristic length determination of nitrous oxide with an ethanol water mixture available. The modeling of the propellant pair should open doors to university design teams that want to work with this easy to store propellant pair.

Acknowledgements

I would like to thank Dr. DeTurris for helping me through the process of my Master's project and telling me when enough was enough and to accept the level of analysis I was at. I would also like to thank the other members of my committee for aiding along the way.

I couldn't have gotten where I am today without the other members of Cal Poly Space Systems, thank you for giving me somewhere to go where everyone was just as excited about rocketry as I was. And thank you to the friends I made in college that gave me a place to go when I wanted to talk about anything besides my academics. Especially my roommates through my Master's project who made living through the COVID-19 quarantine bearable, thank you Eric Venenga, Kirwan Bonifas, Damien Horton and Andrew Yazghur.

Lastly thank you to my family for giving me a place to go home to when the pandemic changed my internship plans and for always being there to support me when my project got strenuous and I needed help getting back on track.

Contents

Table of Figures

Nomenclature

Variables

Symbol	Units	Descriptor
L^*	Meters	Characteristic Length
$\dot{m}$	Kilograms/second	Mass flow rate
ρ	Kilograms/meter^3	Density
A	Meters^2	Area
t	Seconds	Time
F	Newtons	Force
V	Meters / second	Velocity
γ	Unitless	Ratio of Specific Heats
$\bar{R}$	Joules / (mole*Kelvin)	Specific Gas Constant
T	Kelvin	Temperature
P	Pascal	Pressure
M	Kilograms/mole	Molar Mass
OF	Unitless	Oxidizer Fuel Ratio
r	Meters	Radius
D	Meters	Diameter
N	Unitless	Number of Injection Ports
Re	Unitless	Reynolds Number
μ	Pascal*Second	Dynamic Viscosity
φ	Unitless	Ratio
S	Kelvin	Sutherland's Constant

SF	Unitless	Scale Factor
σ	Newtons/Meter	Surface Tension
MMD	Meters	Median Mass Diameter
SMD	Meters	Sauter mean diameter
We	Unitless	Weber Number
L	meters	Droplet Breakup Length
Γ	Unitless	Fuel Vapor Pressure Mass Fraction
B	Unitless	Transfer Number
Nu	Unitless	Nusselt Number
h	Watts / (Meter^2* Kelvin)	Convective Heat Transfer Coefficient
k	Watts / (Meter* Kelvin)	Thermal Conductivity
m	Kilograms	Mass
bara	Atmospheric Bar	pressure

Subscripts

Symbol	**Descriptor**
T	Thrust
g	Gas
e	Exit
c	Combustion
f	Fuel
ox	Oxidizer

cc	Combustion Chamber
t	Throat
0	Initial
v	Vapor
s	Surface
b	Boiling
st	Steady
tot	Total
d	Droplet
inj	Injection
M	Mass transfer
T	Heat transfer
∞	Free Stream

1 Introduction

Rocket engine engineering in industry is moving towards using additive manufacturing to aid regenerative cooling, which has been an integral part of liquid engine design for decades. As additive manufacturing becomes more widely available to all aerospace companies, it will likely see increased use to save cost on complex designs. With this, it is increasingly important that college students are able to attain a better understanding of how these technologies work and the complexity associated with them.

Designing an engine for ground testing comes with its own set of challenges and allowances. The most important factor in designing an engine for college lab use is safety. This immediately brings propellants to the forefront of the design process. Propellants that can be stored without cooling like Hydrazine and Dinitrogen Tetroxide are not feasible for lab use as they are incredibly toxic [1]. Cryogenic propellants like liquid hydrogen and liquid oxygen bring a suite of issues related to cryogenic cooling and storage which cannot be circumvented without substantial cost to the university. This brings fuels similar to RP-1 to the spotlight but the use of regenerative cooling makes the complex hydrocarbons in RP-1 undesirable as coking (buildup of carbon deposits in cooling lines) is likely to occur over prolonged engine use. These constraints lead to a propellant pairing that is fairly inert, easy to store and non-toxic to any students that may make mistakes. N_2O (Nitrous Oxide) is an oxidizer that will be liquid on injection similar to most bipropellant engines in industry and is easily storable in a typical laboratory as a bottle under pressure at room temperature. As far as fuels are concerned, a mixture of ethanol and water is capable of providing adequate cooling in the regenerative cooling lines and is capable of being stored easily in a typical lab environment as well.

Another consideration when sizing an engine for ground testing is that, due to size constraints, a relatively low maximum thrust is on the order of a few hundred pounds of thrust. But designing for in lab use allows for the addition of several sensor ports for data collection and high factors of safety that would not be possible with flight hardware due to weight restrictions.

With the above fuel pair of N_2O and an ethanol water mixture, the main issue becomes lack of documentation available on the propellant pair. The pair does not bring a large I_{sp} to the table, sitting in the low 200 second range, which means that it does not have the decades of published constants and analysis that common propellants have. The biggest hurdle this brings is the absence of a well-defined range of characteristic lengths (L*) that would normally be a simple table lookup. The only published value for the combustion of N_2O and ethanol/water comes from a Master's thesis written by Stewart Youngblood at 6.6 meters [2]. This is considerably higher than most propellant pairs that typically range from 0.8 - 3 meters. The bulk of this thesis aims to demonstrate an engine design process that can, in this case, determine a range of L* for N_2O and ethanol/water. After the range of L* is determined, a ground test engine will be designed based off of a specific L* value within the solved range. Typically, L* is determined through physical testing but due to the pandemic, L* will be solved using fluid mechanics and thermodynamics.

Several simplifications had to be made to the fluid mechanics of the system to allow the solved L* value to provide an accurate estimation of an engine's true characteristic length. From an engine design perspective, the most apparent consequence of these simplifications is the use of a showerhead style injector plate similar to that pictured in Figure 1. This injector design atomizes

the injected fluid by allowing the jet to naturally break up in the combustion chamber without the aid of impinging jets or a physical spray plate.

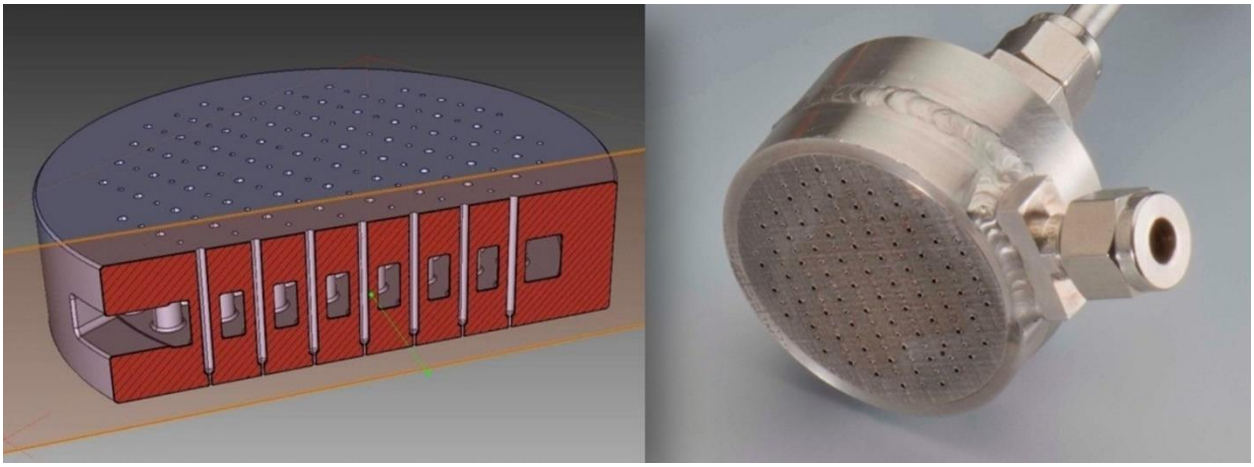

Figure 1: Sample showerhead injector from the European space agency [3]

While this injector style is typically only used for film cooling around the central injector ports it is still fully capable of functioning as an injector plate. The use of a showerhead style design allows for more straightforward fluid mechanical analysis than that of impinging or pintle injector designs. The process of droplet formation is one of three modeled processes that are used to determine the characteristic length of a fuel pair and adding these fluid interactions fell outside of the realistic scope of this project.

There are three main phases of engine development. The first phase, which is expanded upon heavily in this thesis, is the conceptual design. The process of creating and testing the engine should then concentrate most of the complexity in this development phase. The second phase is assembly, which includes the assembly of the system, purchasing of the required parts and materials, and the integration of the system into an existing facility. This phase includes the manufacturing of the parts designed within the thesis and this would likely have to be performed by a professional machinist due to tight tolerancing and complex geometries within the injector. The third phase is operations. This phase will be performed by undergraduate and graduate

students in the lab and will include preparing the engine, running the experiment, recording data and cleaning out the system for storage. This phase should be designed to be the most straightforward, as misuse can heavily damage the system. An important safety note that was taken in account during design is that there should be no point where a person operating the system needs to enter the test area to move pressure lines to ready the system for a nitrogen flush after a test is completed. This should aid in making sure that the system is properly prepared for storage.

1.1 Goals

The current cost of an additively manufactured rocket engine is prohibitively expensive and a model designed for ground testing at the university level is not readily available. The eventual goal with this project is to create and demonstrate liquid engine design process that will be made available to universities to facilitate the addition of a low-cost engine to aid in the teaching of students. This would drive university costs down and allow for more students to have access to well designed and reliable rocket engines in their labs.

2 Background in Cooling Methods

During a firing procedure, a rocket engine produces high amounts of heat that, if left alone, will result in a failure of the combustion chamber and nozzle. There are several ways to circumvent this heating problem that have been developed over the course of modern rocketry.

The simplest method is a consumable liner along the combustion chamber and nozzle walls, commonly referred to as an ablative material. This material pulls heat out of the system by burning away during the fire. The main drawback to this is that it must be consistently replaced for any ground testing and may prove to be excessively heavy for flight applications. Ablative cooling aside, there are several methods of passive cooling of an engine that use the on-board propellants as coolants.

Fluid cooling systems use primarily the on-board fuel as coolant rather than the oxidizer, which is typically more volatile and reactive to heating. Of the coolant flow styles of heat management there are film cooling and transpiration cooling. Both of which inject fuel to the chamber wall with film cooling injecting at the top and transpiration cooling, being injected by a porous media along the sides of the chamber. Both of these methods rely on the propellant pulling in the heat before leaving the system, which eliminates the heat transfer to the walls from the main combustion region.

Other common methods include dump cooling and regenerative cooling. Both of these methods run the cooling propellant through tubes along the side walls of the combustion chamber and nozzle to pull the heat out of the metal. Coolant continues along the wall with the most heat typically being pulled from the throat of the nozzle where the maximum heat flux occurs. Dump cooling, as it sounds, pulls the heat into the cooling propellant then proceeds to dump the propellant out of a port in the coolant line which results in a loss of fuel and payload capacity for orbital and sounding rockets.

This leaves regenerative cooling, which pulls the heat out of the system through the chamber walls while continuing to move the propellant towards and into the combustion chamber itself. This cooling scheme, while being the most lucrative as it wastes no fuel, comes with a host of issues ranging from exhaustive design considerations to complex design complications for traditional regenerative cooling lines.

A comparison of ablative, film, dump and regenerative cooling can be seen in Table 1.

Table 1:Cooling Method Pros and Cons

	Ablative	Film	Dump	Regenerative
Pros	Insulates engine Easy to design for	Creates insulating layer in combustion chamber Typically augments regenerative cooling	No upper limit on coolant mass flow rate High heat transfer capacity	Increases injected fuel temperature Does not use any additional resources when cooling
Cons	Uses expendable inserts Does not teach liquid cooling methods Changes chamber geometry during burn	Can't easily be used in supersonic flow Changes combustion chamber ambient conditions	Ejects fuel from system after use Requires secondary fuel line	Complex design process Mass flow rate of coolant is low in small engines

2.1 Ablative Cooling

Ablative cooling encompasses the use of a burnable material being added between the hot gas area of the engine and the sidewall [4]. The burning of the ablative material both wicks heat by removing the hot material from the system and insulates the sidewall. Ablative cooling can prove to be a valuable cooling resource for short durations firing of small engines that cannot be liquid cooled due to mass flow rate or plumbing restrictions and is used extensively in solid rocket motors [4]. Ablative cooling, however, does not demonstrate fluid cooling technologies and is disregarded during the example design laid out for ground testing in later sections.

2.2 Film Cooling

Film cooling is the practice of injecting a liquid or gaseous film layer into the combustion chamber along the hot gas side of the chamber wall to insulate the chamber [4]. This allows for the engine

run time to be dictated by the fuel tanks rather than the size and burn rate of an ablative material. Note that this remains true for all fluid based cooling methods. Fuel is typically used for this role over oxidizer as a heated oxidizer runs the risk of using the engine wall as fuel for combustion. The use of film cooling will decrease the specific impulse of an engine as the drift in oxidizer to fuel ratio will have adverse effects. This tends to reduce the Isp by 0.5% to 2% in modern engine designs [4]. In terms of total fuel consumption, about 1% to 6% of the total fuel mass flow rate is used for film cooling when applied to an engine for flight [4]. Note that film cooling differs from transpiration cooling in that the coolant is delivered through rings of injection ports as opposed to a porous engine wall that allows coolant to sweat into the combustion chamber [4].

2.3 Dump Cooling

Dump cooling uses a propellant to cool the combustion chamber wall by running fluid bypass interface of coolant on the outside of the chamber and then releasing the coolant overboard [4]. This method can be used to cool the entirety or a section of the combustion chamber. The inherent issue with the use of dump cooling lies in the loss of the propellant after ejection. Due to the loss in propellant this method of cooling has limited use cases [5]. The example engine design laid out in later sections utilizes dump cooling due to material and mass flow rate limitations. Dump cooling can be quite useful in ground testing as the dumped propellant can be collected and used later.

2.3.1 Fluid Bypass Heat Transfer Regimes

When the propellant is pulling heat out of a system in fluid bypass cooling there are different regimes of heat transfer between the hot wall interior and the flowing fluid. This can be seen below noted in Figure 2 which denotes these heat transfer regimes by the different films that appear at given temperature differentials. The forced convection zone is noted by the heat transferring to the flowing propellant and increasing the temperature with no phase change. This method is simple and was the first method used in fluid bypass cooling because it was easier to quantify and create. The obvious drawback of using this simpler method is that the maximum heat that can be pulled out of the system this way is much lower than if the next regime is implemented. The nucleate boiling regime is when enough heat is being transferred into the cooling propellant that small bubbles form due to a localized phase change from liquid to gas. This is caused by the coolant side hot wall temperature being higher than the boiling temperature of the coolant at the current pressure. These bubbles then move from the hot surface to a point further from the hot wall in the coolant line. This method is used increasingly often now as it allows for maximum heat transfer to be achieved in the regenerative cooling system (noted as point C in Figure 2). In the region between C and D is the unstable gas film region, in which the bubbles that began to form in the nucleate boiling regime begin to become too prevalent and a gas layer forms along the hot wall surface.

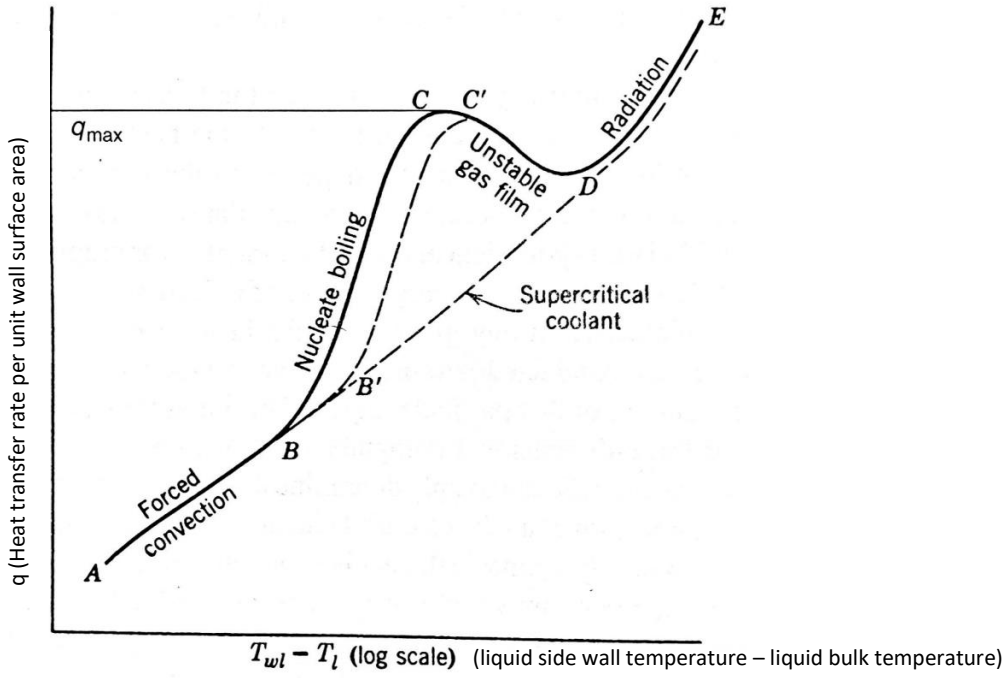

Figure 2: Regimes in heat transfer between a hot wall and flowing boiling liquid [4]

This gas layer will have a much poorer heat transfer to the rest of the coolant as it begins to act as an insulating layer as seen below in Figure 3 which came from a NASA study on ethanol cooled cooling circuit [6]. This will likely cause the interior engine wall to fail. After this is the radiation heat transfer regime if the wall temperature continues to rise but this is not useful for a fluid bypass cooling system. These regimes are also applicable in regenerative cooling methods.

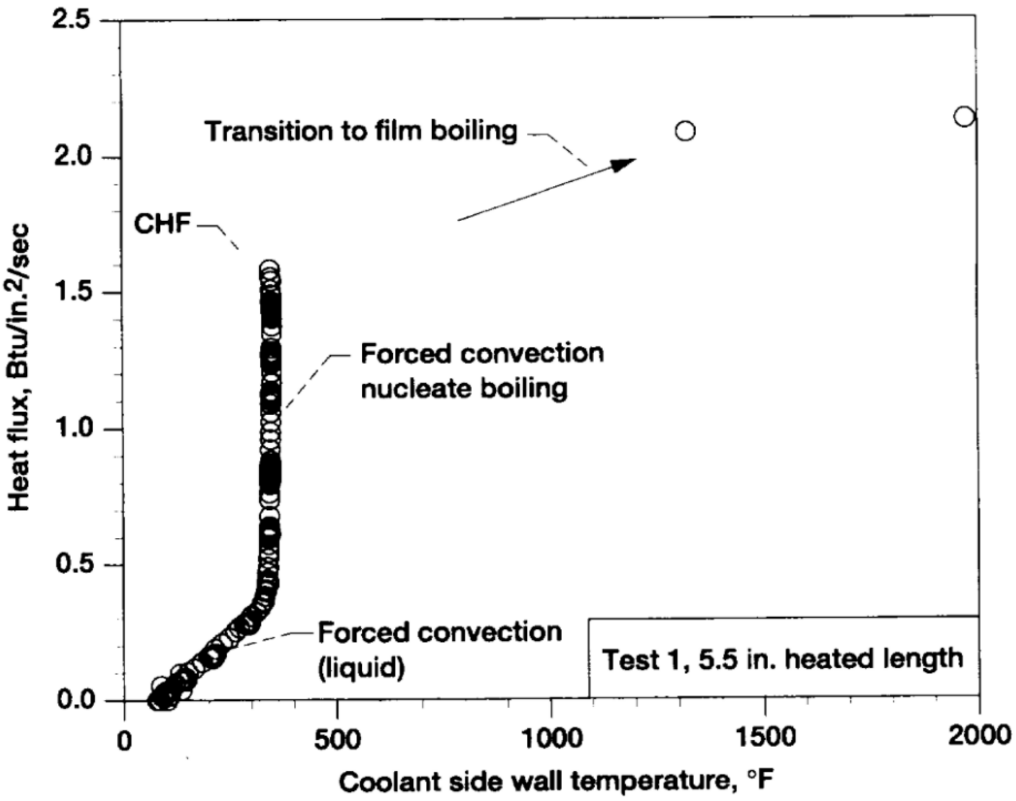

Figure 3: Heat flux vs coolant side wall temperature example [6]

2.3.2 Limitations of Fluid Bypass Cooling

While fluid bypass cooling is very promising it is still bounded in its capabilities. The maximum heat that a coolant can pull out of the combustion chamber wall and nozzle is in part controlled by the wall thickness between the coolant flow path and the combustion. As this wall thickness decreases to allow for more heat to transfer to the coolant the issue of material strength becomes more prevalent. This give and take relationship can be seen in Figure 4. The cross hatched region represents the region that fluid bypass cooling is a viable option as a cooling system. This minimum wall thickness is determined by the compressive strength of the material making up the hot wall of the coolant line which is experiencing both a high temperature differential and high pressures on both sides. The metal does not have a chance to deflect at all while in the forced convection state mentioned above but there is not a clear answer during the state of nucleate

boiling. While the fluid is mostly liquid in the nucleate boiling state, the small gas bubble may prove to dramatically lessen the minimum allowable wall thickness. These limitations apply to both dump cooling and regenerative cooling.

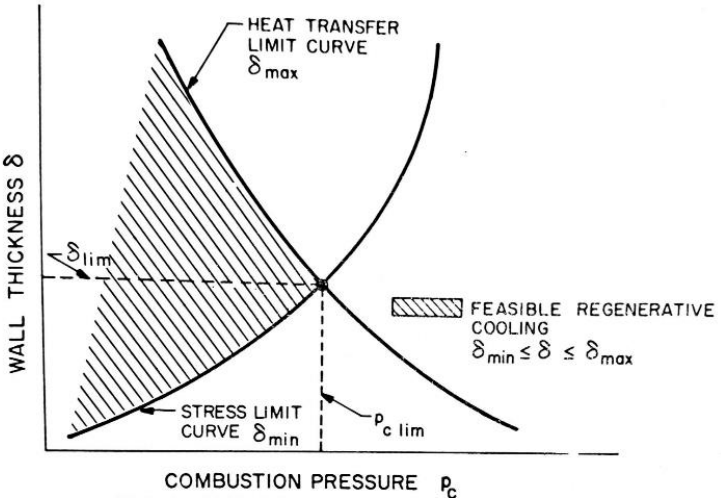

Figure 4: Fluid bypass cooling feasibility limit chart [7]

2.4 Regenerative Cooling

Regenerative cooling is a cooling scheme that allows for a rocket engine to experience prolonged burns without the use of an ablative material or a radiating surface. This cooling effect is created by running propellant, typically a fuel, through tubing along the edge wall of the combustion chamber so the cold propellant can absorb the heat from the engine wall to keep the metal surface temperature low. This warmed propellant is then injected into the combustion chamber and can increase the I_{sp} of the engine very slightly. This is especially useful in the throat of the nozzle as the heat flux is high and an ablative material is not desirable in a throat. The increasing the cross-sectional area during the burn causes losses in efficiency and power in the engine. The total heat that can be pulled out of the system can be solved for using Equation 1. Here Q is the heat absorbed in the system, $\dot{m}$ is the coolant mass flow rate, T is the coolant temperature before and after cooling occurs and c_p is the specific heat of the coolant at constant pressure. Equation 1 helps in early phase design when a mass flow rate is being chosen as it can be varied accordingly to meet needed

heat transfer requirements to keep the combustion chamber walls at a low enough temperature to continue firing.

$$Q_{absorbed} = \dot{m}_{coolant} * \left(c_p * T_{out} - c_p * T_{in}\right) \quad (1)$$

Equation 1:Heat Absorption

2.4.1 Pressure Drop

Outside of manufacturing difficulties, another point of interest is that the propellant will lose pressure between the cooling line inlet and outlet. This is not an issue in cooling systems like dump cooling because the final pressure only has to exceed ambient pressure but in a regenerative cooling system this final pressure must be able to be injected into the combustion chamber. Equation 2 below gives an estimated pressure drop for a fluid line with ΔP being the change in pressure, f being the friction factor for the tube, ρ being the fluid density, V being the fluid velocity and D being the hydraulic diameter [5].

$$\Delta P = f * \frac{\rho * L * V^2}{2 * D} \quad (2)$$

Equation 2: Pressure Drop

This equation is useful for preliminary design as the channel designs may not be circular but will follow a similar trend to the circular lines assumed in Equation 2. After initial design a more advanced estimate must be produced through CFD. The best ways to reduce pressure drop in the cooling lines are to decrease the length of the fluid cooling lines and to decrease the surface roughness. A decrease in length is accomplished by making the coolant lines run parallel to the direction of travel of the combustion gasses. However, a decreasing amount of heat can be pulled out of the system due to the fluid spending less time being passed along the hot wall. The friction

factor, however, does not have this potential drawback and so a lower friction factor is always desirable. The relationship between surface roughness in an additively manufactured part and pressure drop is explored more in section 3.5. For preliminary design phases the pressure drop in a regenerative cooling system can be expected to be between 10% and 20% of the combustion chamber pressure [8]. Upon further development, the pressure drop along a regenerative cooling line can utilize a program such as Rocket Propulsion Analysis for a more detailed pressure loss assessment.

2.4.2 Fluid Cooling Circuits

There are three broad options when creating a cooling circuit, meaning the cooling pathways along the chamber and nozzle walls. For single circuit cooling loops, the fluid can either run in the same direction as the combustion gasses or in the opposite direction. This leaves the third option of a dual cooling circuit setup where the coolant is injected at the throat and then runs counter flow along the combustion chamber or with the flow down the nozzle. An example of single circuit and dual circuit cooling pathways can be seen below in Figure 5. The dual flow cooling loop has been shown to decrease the chances of coking in the coolant lines and decreases the coolant wall temperature as well [9]. The only disadvantage of using dual circuits is the increase in manufacturing cost and complexity due to the system being constructed with traditional manufacturing. The system would, in turn, become much more desirable with the use of additive manufacturing as the manufacturing complexity is less of a contributing design factor.

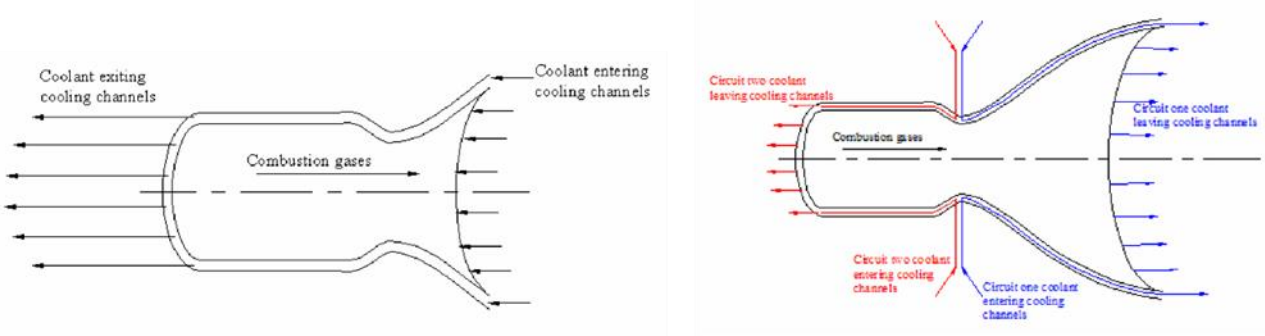

Figure 5: Cooling circuit example, single circuit counter flowing (left) & dual circuit (right) [9]

3 Background in Additive Manufacturing

The issues regarding manufacturability arise when the scale of the engine decreases or the cooling channels required cannot be traditionally manufactured by lathe and mill work. The decrease in size results in the need for small, complex shaped tubes that can easily be bent or blocked during transport. These manufacturing issues can be solved through the use of additive manufacturing.

Additive manufacturing is a surprisingly broad term which essentially means a part can be produced by adding material instead of reducing the amount of material similar to the aforementioned lathe or mill. This includes processes similar to what the layman may describe as 3D printing of plastics, as this has become more popular over recent years, and also includes metal printing, which has several different techniques. The Laser Wire Direct Closeout (LWDC) is controlled by a high-powered laser and inert gas nozzle that aim towards a wire that moves to

create a shell layer by layer quickly but does not produce a smooth surface. This method is pictured in Figure 6.

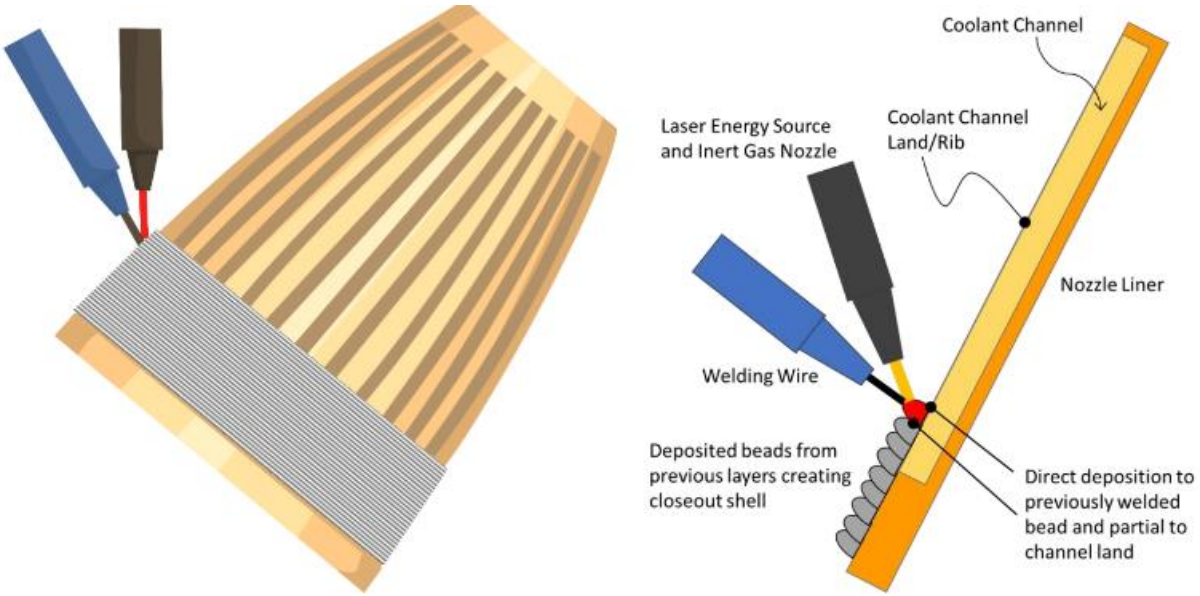

Figure 6: Laser wire direct closeout [10]

The second common additive manufacturing method is powder blown direct energy deposition (DED) which looks similar to a desktop 3D printer and functions by blowing a metal powder into a high energy electron beam or laser which melts the new powder onto the part as it passes as pictured in Figure 7. This method produces a better surface finish than LWDC and is only limited by the size of the print arms used to blow the powder into the model.

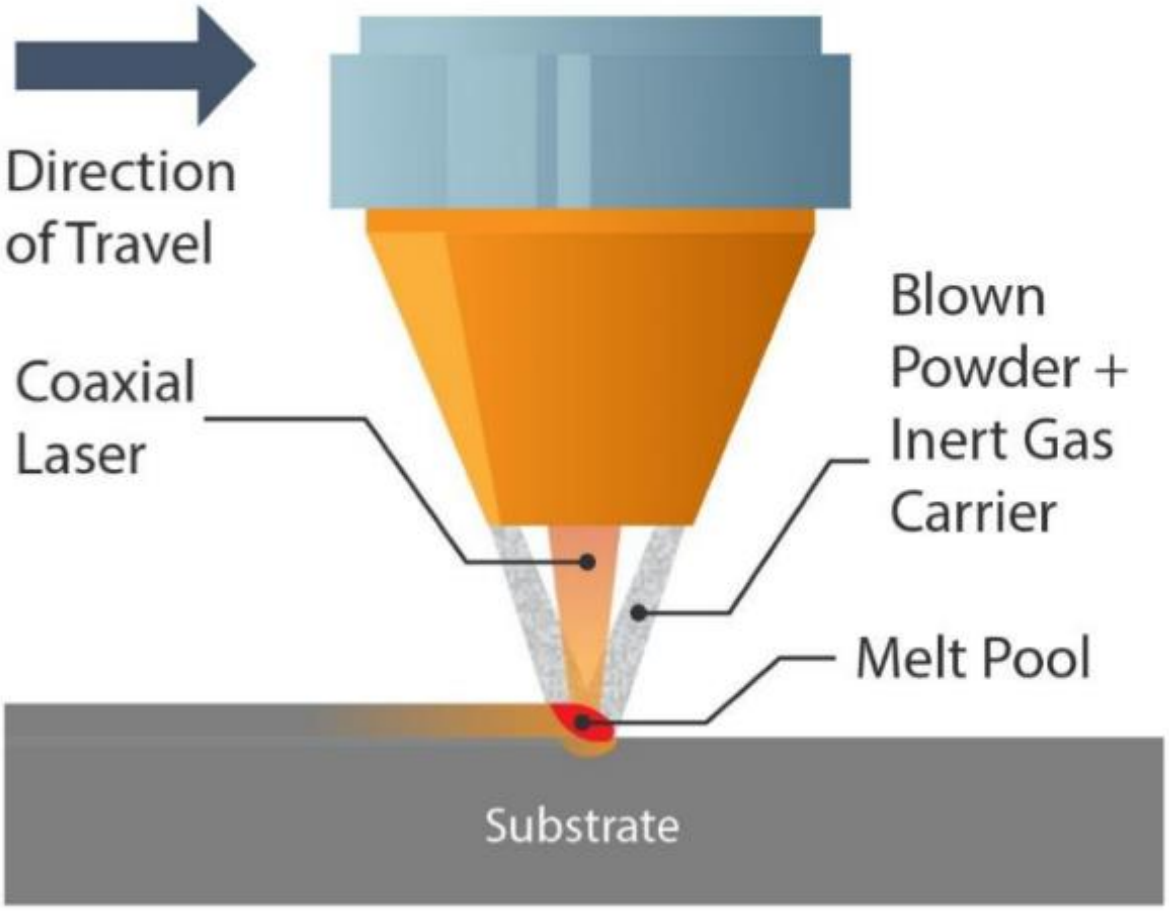

Figure 7: Directed energy deposition [11]

The third common printing methods is selective laser sintering (SLS), which is also commonly referred to as selective laser melting or powder bed printing. Note that this process shown in Figure 8 is actually melting the metal powder but the term sintering is most commonly used due to being the oldest reference. This method uses a print box and fills with the metal powder, layer by layer, while a high-power laser melts each new layer before adding more powder. This method provides the highest quality surface finish at the cost of time and print volume as the system must fill entirely with the powder, and for that reason the print boxes typically range on the scale of ten to twenty inches in side wall length.

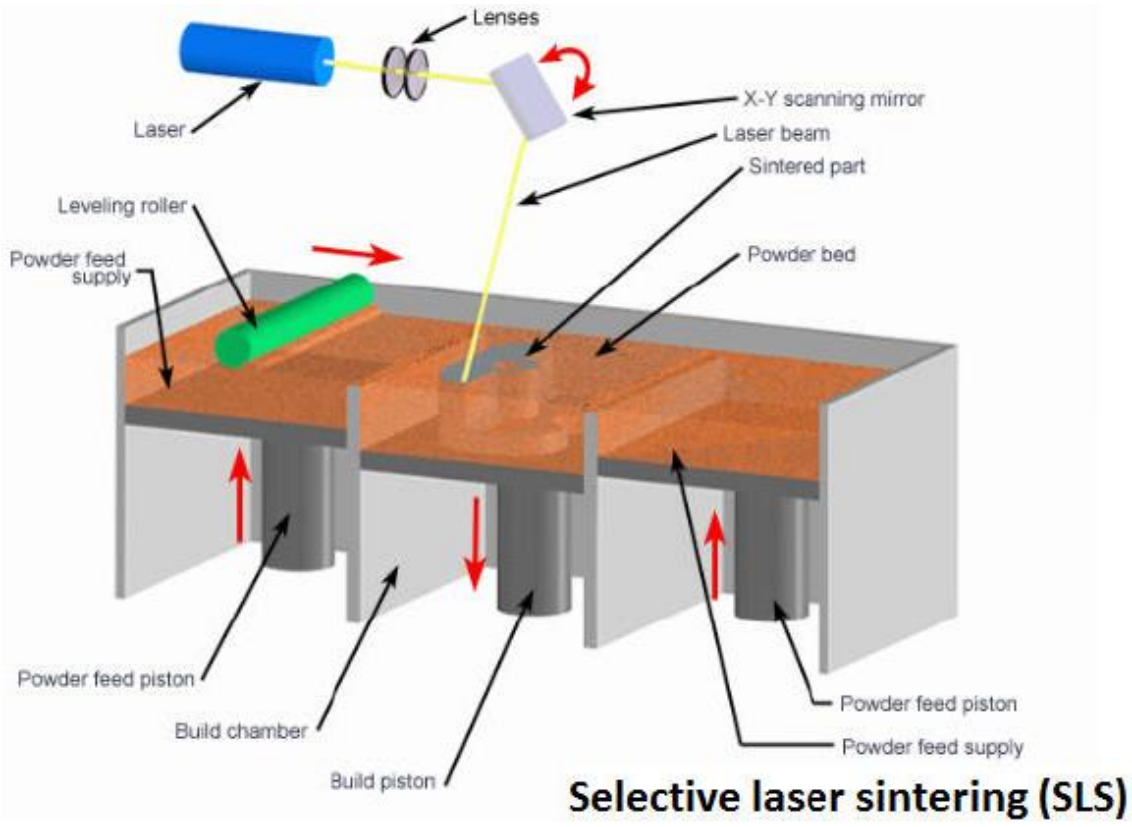

Figure 8: Selective laser sintering [12]

For the sake of comparison Figure 9 shows SLM print boxes in relation to several rocket engines.

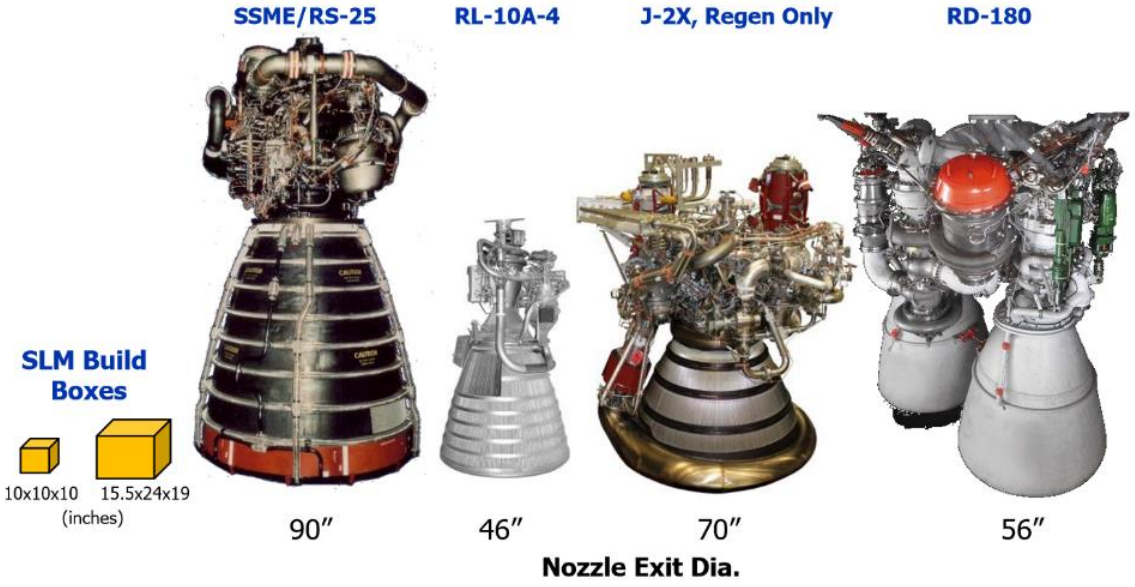

Figure 9: SLM print box comparison [13]

3.1 Current Printed Engines

As a manufacturing method that is new relative to its traditional counterparts, only a few companies have made it their goal to print rocket engines for flight. These companies include Relativity, Launcher and Ursa Major Technologies, all of which have made their primary goal to fully realize the use of additive manufacturing in the rocket engine development world. These companies' engines are pictured in Figure 10.

Figure 10: Launcher, Relativity, and Ursa Major Technologies (left to right) [14] [15] [16]

This is not to say that all use the same additive manufacturing technology. Relativity boasts that their DED printer, named Stargate, is the largest on the planet and they aim to print the entire rocket, not just the engine, using Stargate. Note that the relativity engine pictured above, named Aeon, has been post processed and does not come out of the printer with that high-quality finish. This is compared to the more textured finish of the Launcher and Ursa Major Technologies engines which use SLM to produce their engines. These different methods being used side by side in industry help to illuminate that there is still far from a clear-cut answer as to what printing method is best. This being said, the existence of these companies shows that there is reason beyond the academic to pursue this method of rocket engine design in production. Outside of these companies,

several test engines have been produced and fired by NASA since 2013 [11] as shown below in Figure 11 where a DED nozzle is being fired for 15 seconds while implementing regenerative cooling.

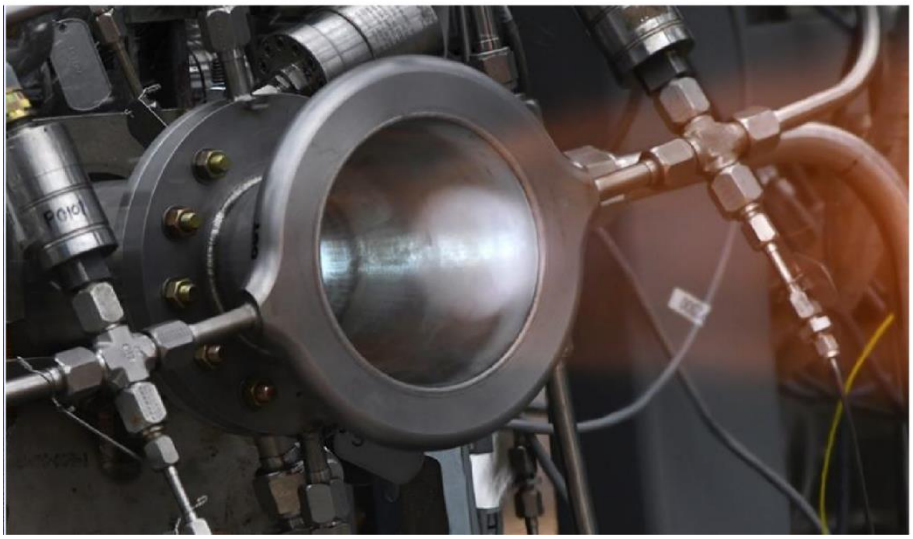

Figure 11: DED nozzle during test fire [11]

3.2 Selective Laser Melting

Selective laser melting uses a powder bed and a high-powered laser to melt individual layers together to form the final part. This method's surface roughness is the lowest of all forms of metal based additive manufacturing, ranging from 5-35 μm [17]. This range of surface roughness is determined by the curvature of the part, the material being used and the quality of the SLM printer. The curvature stair stepping effect can be seen below in Figure 12. The material effect on surface roughness is determined by the powder size of the material in question. As the powder size decreases the minimum layer thickness required in the powder bed decreases as well and can result in a lower surface roughness. The final factor, the quality of the machine is determined by the manufacturer of the machine and cannot be changed by the design engineer but rather is a tradeoff between required surface roughness and associated cost of machine time.

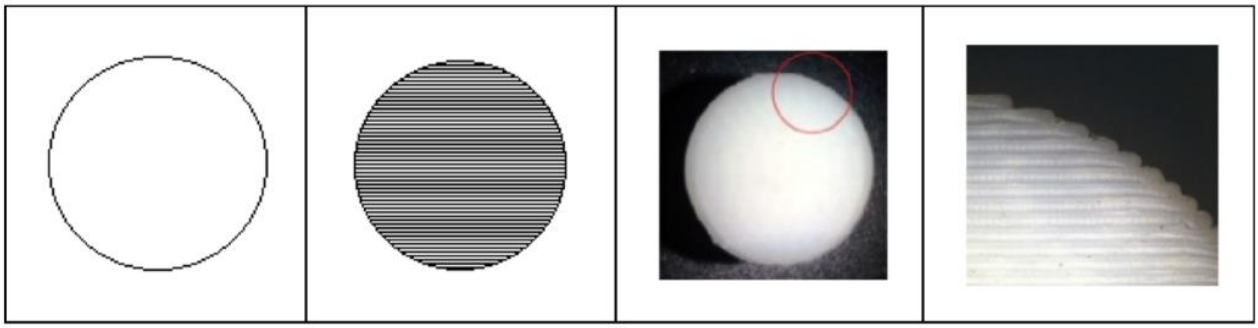

Figure 12: Example part in CAD, sliced model, real output and a zoom in on the stair stepping effect (left to right) [17]

3.3 Post Processing

Several post processing techniques exist to make the surface finish of an additively manufactured part more presentable. The simplest of these is traditional machining where a part can be placed on a mill and have its outer layers cut away by a drill head to reveal a smooth surface underneath. Unfortunately, this method is not acceptable for the post processing required to smoothen cooling channels as there is no way to access the internal features of the engine. The same issue befalls hot cutter machining, optical polishing, and vibratory bowl abrasion [17].

There are some non-conventional techniques that are currently being researched that may prove useful for coolant line post processing, including ultrasonic abrasion, chemical post-processing treatment and electrochemical polishing [17]. Ultrasonic abrasion blasts the part with ultrasonic sound waves and this decreases the surface roughness significantly, being recorded as a 74% reduction in surface roughness [17]. Interestingly this method also has been recorded to decrease the surface roughness of interior surfaces as stated by Dr. Wang in the Cal Poly IME department. The ultrasonic abrasion also proved to condense the printed metal and give it a higher material strength. Unfortunately, this method is still very experimental and not reliable enough to warrant use in rocketry as of yet. Chemical post processing is also still in early stages of development and

cannot guarantee a uniform surface finish. This also goes for electrochemical polishing as there is still a lot of work to be done in this field. There is also a possibility of flowing an abrasive fluid through the cooling channels [17] but this would have to be tested on the print metal beforehand to ensure a predictable surface reduction.

3.4 Printable Material Options

There are numerous choices of metal powders that can be used in additive manufacturing. The GRCop series of powders, an Aluminum powder alloy called $AlSi_{10}Mg$ and Inconel 625 are expanded upon. In the following sections these three powder types offer a wide range of characteristics and should offer a decent sample of currently available.

3.4.1 GRCop-42 and GRCop-84

GRCop-42 and GRCop-84 are both copper alloys consisting of copper, chromium, and niobium developed under NASA in 1987 with the sole purpose of being used in rocket engine development. Of the two, GRCop-84 displayed more favorable mechanical properties and GRCop-42 traded some of its mechanical strength for higher thermal conductivity, giving it about an 11% increase in thermal conductivity at room temperature [18]. These alloys are the ideal metals to be used in combustion chamber liners and are fantastic for additive manufacturing. Unfortunately, this is expensive, with kilograms of the powder costing thousands of dollars, and along with this, the favorable material properties have resulted in very long lead times on printed parts. This lead time can delay a project for months to over a year depending on the backlog of parts a company is being asked to produce. The powder form composition of GRCop-42 and GRCop-84 can be found in Table 2. The data in this table may prove important when design constraints prohibit the use of certain elements.

Table 2: Powder Chemistry Comparison of GRCop-42 with GRCop-84 [18]

Element	GRCop-42 Wt %	GRCop-84 Wt %
Cr	3.1 – 3.4	6.2 – 6.8
Nb	2.7 – 3.0	5.4 – 6.0
Fe	Target <50 ppm	Target <50 ppm
O	Target <400 ppm	Target <400 ppm
Al	<50 ppm	<50 ppm
Si	<50 ppm	<50 ppm
Cu	Balance	Balance
Cr:Nb Ratio	1.12 – 1.15	1.12 – 1.15

3.4.2 Aluminum Alloys

Aluminum powders offer a high thermal conductivity and a large abundance of powder manufacturers with several alloys to choose from, $AlSi_{10}Mg$ being the most common in additive manufacturing. This aluminum powder must be printed in a facility designed to handle aluminum powder as it is incredibly flammable to the point that it is used as a doping agent in solid rocket propellants. This flammability is due to the size of the aluminum powder itself, which can be found as small at 25 μm [19]. Though aluminum has a lower melting point than the other metals that are available, due to its thermal properties and the ease of access this will likely be the metal type used in this project.

3.4.3 Inconel 625

Inconel 625 is a super alloy with a percent weight composition shown on the right in Table 3 [11] to give a more detailed makeup of this version of Inconel. The Inconel 625 superalloy has been selected by NASA for use with kerosene coolants which is also a hydrocarbon like the ethanol being used in this project. It also offers the capability of a printed layer thickness between 30 and 60 μm [19]. Unfortunately, although Inconel can withstand incredibly high temperatures, it has a thermal conductivity comparable to that of steel, being incredibly poor when compared to either

the GRCop family or the aluminum alloy families. This may not be an issue for engine development due to the higher heat load capabilities as this may require less heat be pulled from the combustion chamber walls. However, this is not what this project is aiming to demonstrate as a metal that can withstand the heat of combustion may not need to be cooled beyond convection and radiation with the surrounding lab. The data in Table 3 aims to provide the makeup of the alloy in the event that design constraints prohibit certain elements.

Table 3: Elemental Composition of Inconel 625 by Percent

	Inconel 625
Nickel	58.0 min
Chromium	20.0 - 23.0
Iron	5.0 max
Molybdenum	8.0 - 10.0
Niobium	3.15 - 4.15
Carbon	0.10 max.
Manganese	0.50 max.
Silicon	0.50 max.
Phosphorus	0.015 max.
Sulfur	0.015 max.
Aluminum	0.40 max.
Titanium	0.40 max.
Cobalt	1.0 max.

3.5 Surface Roughness and Pressure Drop

With so many unknowns in the post processing finish, due to no one method being decided upon, assuming a high the surface roughness would help yield a conservative estimate for supply pressure. As a lab-based engine, a higher supply pressure that would be required for minimal post processing is allowable through a change in the feed system design as weight is not a controlling factor.

4 Background in Propellants

This section analyzes the mixture of ethanol and water as well as the inherent safety of N_2O and ethanol being used as propellants. A brief mention of coking is brought to attention as well which, while not analyzed further, may have an effect on the longevity of the engine when real world testing is performed.

4.1 Reasoning Behind Fluid Mixture

The mixture of N_2O and the ethanol water slurry was driven mainly by a safety and storage perspective as both are non-toxic and can be held in storage inside of an indoor facility quite easily. N_2O poses the largest potential risk as an oxidizer that sits just below it's critical temperature of 309.4 Kelvin at room temperature. The propellant pair yields a reasonably high Isp of 215 seconds and a combustion temperature of just over 3000 Kelvin [20]. The main draw for adding water to the ethanol fuel comes from implementing regenerative cooling as water is more capable of holding high heat loads than ethanol [21], the specifics of which will be outlined in the Engine Development section. This addition of water also aids in lowering the heat generated during combustion as the water acts as an inert substance [20].

4.2 Nitrous Oxide and Ethanol Fuel Pair

The current fuel pair being examined is a liquid nitrous oxide and liquid ethanol fuel pair. This fuel pair is one that the Cal Poly propulsion lab is currently equipped to handle as both nitrous oxide and a diluted ethanol have been used in the lab in the last year. Both of these propellants are safe to handle without hazmat suits and are stable under standard lab conditions. This assumes that the nitrous oxide is being kept at room temperature and not in direct sunlight. The nitrous oxide will only stay in liquid form under pressure so accommodations must be met for storage and use but the Cal Poly propulsion lab is more than equipped to handle pressurized vessels. This makes

the fuel pair favorable as any university with a propulsion lab could test this engine without major lab changes.

4.2.1 Coking

Coking is the formation of solid carbon resulting from the pyrolysis of a hydrocarbon, in this case ethanol [22]. This carbon residue can be deposited on the hot wall side of a cooling channel and decrease the effectiveness of the heat transfer across the wall to the cooling fluid. In a paper published by the Journal of Analytical and Applied Pyrolysis a detectable amount of coking was witnessed at 3.5 MPa at just under 1000 K [22]. The coking was observed to have become 4.4 times more prevalent on the regenerative cooling surface with an increase from 0.7 to 3.5 MPa. While this hydrocarbon is not the same one being used in this project, the trend is important to note. The coking layers that are deposited are likely not a problem for individual short duration test fires but under prolonged exposure to a pyrolyzing ethanol over the course of repeated firing a significant layer may occur. This coking issue is less important if the system does not allow for the coke to deposit in the cooling channels. In the event that the engine designed in this forthcoming analysis experiences coking during testing further research will have to be done on measures to prevent coking.

5 Engine Design Process

Before delving into the detailed process of engine design a general framework is necessary to aid in understanding why each part of the engine design process is necessary.

Beginning the design process requires the setting of design constraints, this includes thrust, propellants, thrust, oxidizer to fuel ratio, chamber pressure, designed exit pressure and a range or injector port diameters and the number of said injector ports. If additional design constraints exist these should be defined at this stage. With these values defined a simulation of combustion can be

performed using the NASA chemical equilibrium applications software (NASA CEA). The outputs from the NASA CEA software are then available to be used in combustion chamber sizing.

The geometry of the chamber is defined using the area of the throat, the ratio of the throat to the nozzle, the length and radius of the main combustion chamber. The throat area and expansion ratio can be solved using outputs from a NASA CEA software but the length and radius are dependent on the NASA CEA software outputs and the characteristic length of the combustion chamber. The characteristic length can be determined by finding the residence time of the injected fuel in the combustion chamber. This residence time (the time it takes for fuel to complete combustion) is found by independently solving the found phases of residence time, being time of droplet formation, time of droplet heating, time of droplet evaporation and time of combustion.

Once characteristic length is found, all values needed to generate an engine geometry are accounted for and can be used in an engine modeling software (Rocket Propulsion Analysis in the case of this project). At this stage heat transfer simulations need to show a closed heating loop, if the engine edge wall does not stay sufficiently cool, one or more cooling methods must be implemented. Note that at this point, if film or transpiration cooling are used the previous steps must be repeated to account for the changing oxidizer to fuel ratio of the engine. After sufficient cooling has been established the geometry can be passed to a 3D modeling software for visualization and structural testing. At this point the engine design is ready for manufacture and testing.

An in-depth flowchart of this design process can be found in the appendix in section 12.8 and is described in section 6 and 7.

6 Combustion Chamber Sizing Process

This section details the segmented analysis of characteristic length, and sizing of the combustion chamber. The characteristic length estimation is broken into residence time segments being the amount of time required for a droplet to form, time required to heat said droplet to its boiling point and time required for this boiling to completely convert the liquid droplet to a gas.

6.1 Engine Design Constraints

Before injection can be simulated, some aspects of the combustion chamber need to be chosen to determine propellant mass flow rates and injection velocities. Using NASA CEA an estimate for thermophysical properties of the combusted gas in the combustion chamber, throat and nozzle exit plane should be found.

The mass flow rate is determined by relations of the thrust, ratio of specific heats, combustion temperature, combustion static pressure, exit static pressure and molecular density of the combusting gas. This is done by substituting Equation 3 for exit velocity in Equation 4 to yield Equation 5 [4]. In these equations, F is thrust, $\dot{m}$ is mass flowrate, V_e is exit velocity, γ is the ratio of specific heats, $\bar{R}$ is the universal gas constant, M_g is the molecular mass of the exhausted gas, T is temperature, and P is pressure. Note that Equation 4 assumes perfect expansion of the nozzle [4].

$$V_e = \sqrt{\frac{2 * \gamma}{\gamma - 1} * \frac{\bar{R}}{M_g} * T_c * \left(1 - \frac{P_e}{P_c}\right)^{\frac{\gamma-1}{\gamma}}} \tag{3}$$

Equation 3: Exhaust Velocity Based on Gas Dynamics

$$F_T = \dot{m} * V_e \tag{4}$$

Equation 4: Basic Thrust

$$\dot{m} = \frac{F_T}{\sqrt{\frac{2 * \gamma}{\gamma - 1} * \frac{\bar{R}}{M_g} * T_c * \left(1 - \frac{P_e}{P_c}\right)^{\frac{\gamma-1}{\gamma}}}} \tag{5}$$

Equation 5: Propellant Flow Rate

Here $\dot{m}_f$ is the fuel mass flow rate, $\dot{m}_{tot}$ is the total mass flow rate, and *OF* is the oxidizer fuel ratio.

$$\dot{m}_f = \frac{\dot{m}_{tot}}{1 + OF} \tag{6}$$

Equation 6: Fuel Mass Flow Rate

The oxidizer mass flow rate is then found by using Equation 7 with the solved total mass flow rate and fuel mass flow rate.

$$\dot{m}_{ox} = \dot{m}_{tot} - \dot{m}_f \tag{7}$$

Equation 7: Oxidizer Mass Flow Rate

Once all mass flow rates are calculated a throat area and a throat radius are determined using Equation 8 and Equation 9 respectively, wherein A_t is the area of the throat and r_t is the radius of the throat [8].

$$A_t = \frac{\dot{m}}{P_c * \gamma * \sqrt{\frac{1}{\gamma * \frac{\bar{R}}{M_g} * T_c} * \left(\frac{2}{\gamma + 1}\right)^{\frac{\gamma+1}{\gamma-1}}}} \tag{8}$$

Equation 8: Area of Throat

$$r_t = \sqrt{\frac{A_t}{\pi}} \tag{9}$$

Equation 9: Radius of Throat

With these values defined the process of determining the characteristic length for the particular propellant pair can begin.

6.2 Breaking L* into Base Parts

Developing a workable characteristic length is typically achieved through physical testing. The determination of L* can also be completed by modeling the fluid flow of the injected fuel and following its path until combustion occurs. This relationship is represented by Equation 10, adapted from *Modern Engineering for Design of Liquid-Propellant Rocket Engines* [5] where t_{stay} represents the residence time or stay time of an injected droplet of fuel, ρ_g is the gas density and L^* is the characteristic length.

$$L^* = \frac{\dot{m} * t_{stay}}{\rho_g * A_t} \tag{10}$$

Equation 10: Characteristic Length from Residence Time

This residence time is derived from the addition of four phases of the droplets lifetime before combustion has completed, shown in Equation 11 [23].

$$t_{stay} = t_{breakup} + t_{heating} + t_{evaporation} + t_{combustion} \tag{11}$$

Equation 11: Total Residence Time

Each of these time segments is explored in more detail in a later section exploring the development of each individually.

6.3 Droplet Formation

The first segment of residence time is based on the formation of a droplet from an injection jet. With no defined fuel injector port diameters, a range of total diameters should be used to generate a visual when performing analysis. The actual port size diameters are calculated using Equation

12 and Equation 13 to solve for port area and port diameter respectively. In these equations A_{port} is the port area of a single injector port, $D_{inj\ total}$ is the total diameter of injector ports and N is the number of injector ports and D_{port} is the diameter of a single injector port. Note that the total diameter is the diameter of an equivalent area injector port to all relevant injector ports.

$$A_{port} = \frac{\pi * \left(\frac{D_{inj\ total}}{2}\right)^2}{N} \tag{12}$$

Equation 12: Total Injector Port Area

$$D_{port} = \frac{D_{inj\ total}}{\sqrt{N}} \tag{13}$$

Equation 13: Injector Port Diameter

With port diameter and fuel mass flow rate defined, the injection velocity is solved for by rearranging the traditional mass flow rate equation as Equation 14 adapted from the mass flow rate equation from *Rocket Propulsion Elements* [4]. Where V_{inj} is the injection velocity of the fuel.

$$V_{inj} = \frac{\dot{m}_f}{\rho_f * A_{port}} \tag{14}$$

Equation 14: Fuel Injection Velocity

Next, Reynolds number of each flow point has to be calculated. This is to ensure that later analysis can assume the flow is turbulent after injection. Reynolds number for the flow is calculated using Equation 15 where Re_{inj} is the injecting fluid's Reynolds number and μ_f is dynamic viscosity the of the fuel [5].

$$Re_{inj} = \frac{\rho_f * V_{inj} * D_{port}}{\mu_f} \quad (15)$$

Equation 15: Reynolds Number

With injection velocity and port diameter defined the fuel density and fuel dynamic viscosity are solved for next. These variables are determined by taking a weighted average of the characteristics for ethanol and water using Equation 16 to determine density of the fuel [21], where φ_{mix} is the ratio of ethanol to water in the mixture. The weighted averaging of densities for this mixture of pure components should not yield any significant percent error [21].

$$\rho_f = \rho_{C_2H_5OH} * \varphi_{mix} + \rho_{H_2O} * (1 - \varphi_{mix}) \quad (16)$$

Equation 16: Density Weighted Average

A weighted average is not typically desired for viscosity analysis of a mixture of fluids but is an acceptable method. Using this weighted average method, depicted in Equation 17, typically yields a maximum of 15% error in absence of physical testing [21].

$$\mu_f = \mu_{C_2H_5OH} * \varphi_{mix} + \mu_{H_2O} * (1 - \varphi_{mix}) \quad (17)$$

Equation 17: Dynamic Viscosity Weighted Average

The final thermophysical properties of the system that needs to be determined before droplet formation can be analyzed is the dynamic viscosity of the combusting gas and the surface tension of the ethanol water mixture. The dynamic viscosity of the combusting gas can be estimated by relating the combusting gas to high temperature, high pressure air as shown in Equation 18 where S_μ is the Sutherland constant for air, T_0 and T are the initial and final temperature respectively and μ_0 and μ are the initial and final dynamic viscosities respectively [24].

$$\frac{\mu}{\mu_0} = \left(\frac{T}{T_0}\right)^{\frac{3}{2}} * \frac{T_0 + S_\mu}{T + S_\mu} \tag{18}$$

Equation 18: Sutherland's Law

The air viscosity can then be multiplied by a scale factor based on the ratio of the gas constants of the combusting gas and air, reflected in Equation 19. This scale factor should be a reasonable approximation of the similarities between air and the combusting gas given the closeness if their respective gas constants.

$$SF = \frac{\bar{R}_g}{\bar{R}_{air}} \tag{19}$$

Equation 19: Combustion Chamber Scale Factor

The surface tension of the injected ethanol water mixture can then be determined with use of weighted averaging. Surface tensions for the pure components can be based on surface tension values from the Dortmund Databank, an online resource for thermophysical properties of different fluids [25]. The estimate of the surface tension of the mixture is shown in Equation 20, where σ denotes the surface tension of the referenced fluid. Using this method of weighted averages may yield error of up to 10% [21].

$$\sigma_f = \sigma_{C_2H_5OH} * \varphi_{mix} + \sigma_{H_2O} * (1 - \varphi_{mix}) \tag{20}$$

Equation 20: Fuel Surface Tension Weighted Average

With the thermophysical properties of the system defined, fuel droplet formation can now begin being modeled. The first step is determining the droplet size and shape which then leads to determining breakup time. The shape of the droplets will be assumed to be perfectly spherical and

of equal size between droplets. This simplification and comparison to more realistic droplet shapes shown in Figure 13.

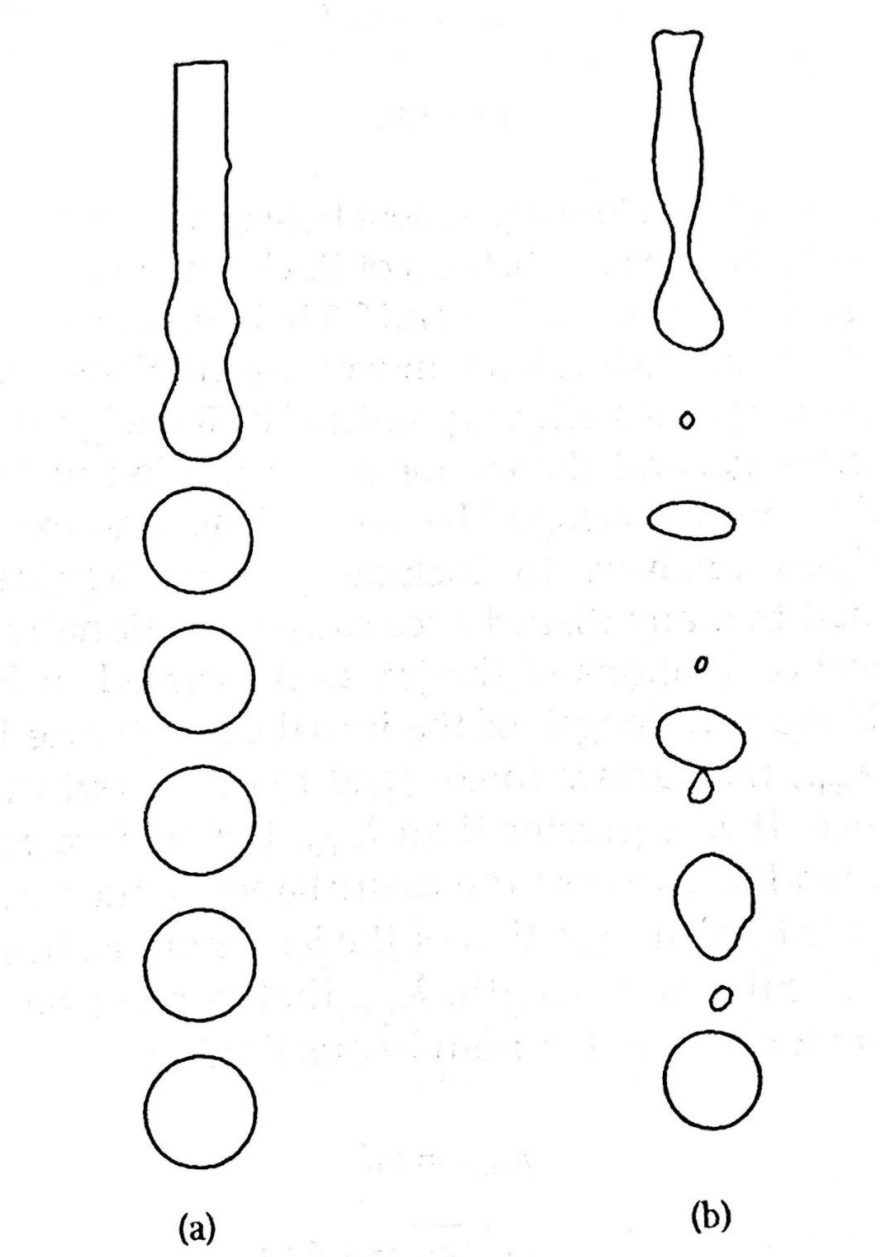

Figure 13: Ideal(a) vs realistic(b) droplet formation based on high-speed photography [23]

This estimation of droplet shape and regularity will yield an over estimation of characteristic length as smaller droplets required less time to fully progress to the combustion stage. There are two main

options when estimating droplet diameter, either the median mass diameter (MMD) or the Sauter mean diameter (SMD). Of these, the SMD is a much better estimation of droplet diameters as MMD is estimated using Equation 21 which only takes the injection port diameter and injection Reynolds number in to account whereas the SMD takes several fluid characteristics into account and can be approached [23]. Where Re_L is the Reynolds number of the injected liquid.

$$MMD = 6 * D_{inj} * {Re_L}^{-.15} \tag{21}$$

Equation 21: Median Mass Diameter

Along with this the equation for estimating MMD is bound between Reynolds numbers of 1,000 and 12,000 which makes it inviable for use in many design cases. SMD is simulated using Equation 22 , adapted from *Atomization and Sprays* [23] where both the fluid properties of the injected fluid and the combusting gas are taken into account. Note the subscript, $_L$ represents the properties of the fuel droplet, $_g$ represents the properties of the combusting gas, and $_0$ represents the droplet initial state.

$$SMD = 330 * {d_0}^{0.3} * {\mu_L}^{0.07} * {\rho_L}^{-0.684} * {\sigma_L}^{-0.15} * {V_L}^{-0.55} * {\mu_g}^{0.78} * {\rho_g}^{-0.052} \tag{22}$$

Equation 22: Sauter Mean Diameter

This is one of several estimations for the SMD of an injected fluid. Unfortunately, despite over a century of study, a singular equation is yet to be developed to estimate droplet formation diameters. Equation 21 and Equation 22 reflect the use of a shower head injector and injecting into quiescent air. While a combustion chamber does have a near-zero gas velocity, the combustion taking place forces turbulent conditions in the combustion chamber. Unfortunately, due to inherent difficulties of taking measurements in combustion chambers there exists very little data specific to SMD on

the inside of a combustion chamber so the error introduced into the system cannot be estimated for this step without further research and testing. Typically, SMD calculations are based on curve fitting to observable droplet formation of water jets into high pressure air. An example of the relationship between liquid viscosity and SMD can be seen in Figure 14.

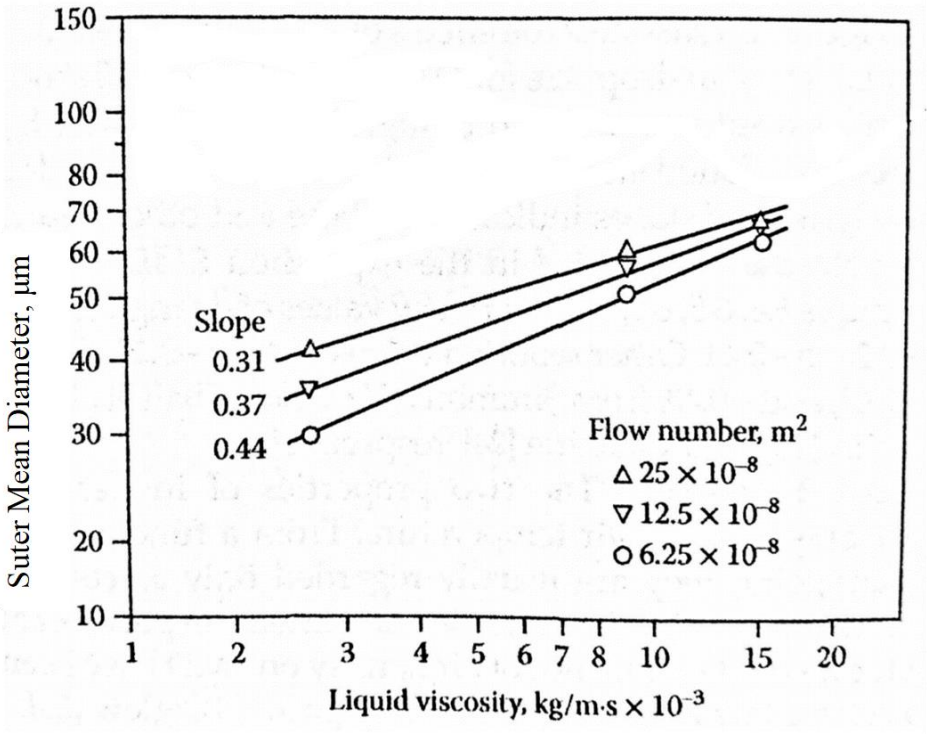

Figure 14: Influence of viscosity on SMD for liquid water [23]

At this juncture one more variable is required before the droplet breakup length can be estimated, the Weber number of the fuel droplet. The droplet Weber number is determined using Equation 23 where D_0 is defined as the droplet SMD [23].

$$We = \frac{\rho_f * {V_f}^2 * D_{drop}}{\sigma_f} \tag{23}$$

Equation 23: Weber Number

With the Weber number for the droplet defined an estimation of the droplet breakup length can be determined.

There exist district regions, outlined in Figure 15, that relate internal turbulence/jet velocity to jet breakup length. The analysis process that follows will design for the turbulent flow region between points C and D.

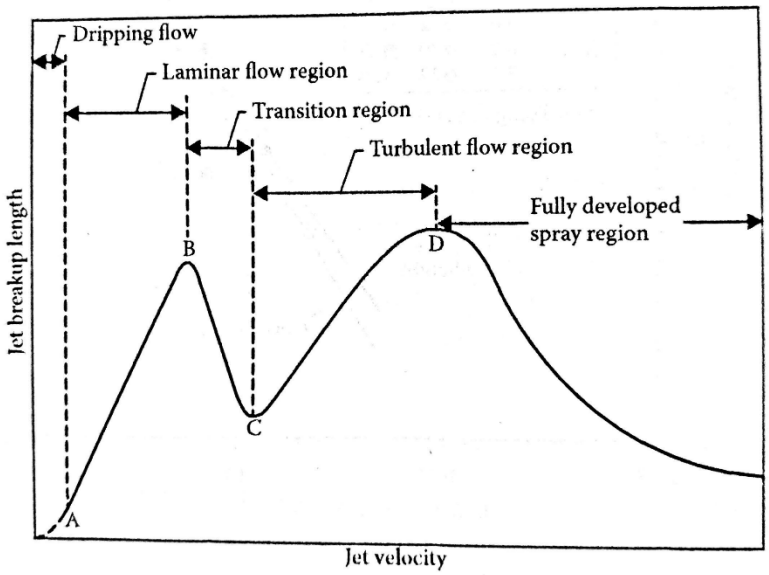

Figure 15:Jet stability curve [23]

Two estimations exist for droplets breakup length in the turbulent flow region, the Grant-Middleman estimation and the Baron estimation shown in Equation 24 and Equation 25 respectively [23], where L is the estimated breakup distance, D_0 is the injection diameter and We is the Weber number.

$$L = 8.51 * D_0 * We^{0.32} \tag{24}$$

Equation 24: Break Up Length Grant-Middleman Estimation

$$L = 538 * D_0 * We^{0.5} * Re^{-0.625} \quad (25)$$

Equation 25: Breakup Up Length Baron Estimation

Both of these estimations assume a long smooth tube to perform injection where the ratio of port diameter to port length is substantial. These estimations are fit to a data set from Miesse's water data [23] that recorded the atomization of water injection. By combining the estimated jet breakup length and the injection velocity of the fuel in Equation 26, a jet breakup time can be developed.

$$t_{breakup} = \frac{L}{V_{inj}} \quad (26)$$

Equation 26: Time for Breakup to Occur

With this first segment of the total residence time fully defined and the next estimation of droplet evaporation can begin.

6.4 Droplet Heating

In order to simplify the problem further, the injected fuel is assumed to stay at its injection temperature until the droplet has been formed. This is done because the equations to track droplet heating are built around the heat up of a spherical droplet as explored below. Other assumptions for the droplet heating phase include that the droplet is spherical, the fuel is a pure liquid with a defined boiling point and that radiative heat transfer is negligible [23]. Similar to the droplet breakup analysis, there is a substantial amount of setup that had to be completed before droplet heat up analysis could occur.

Vapor pressure is one of these necessary variables that needed to be produced, functioning as the pressure at which a liquid will sit in an enclosed container at the specific temperature. This value will control the pressure that the droplet would naturally be during the heat up and evaporation

process. The vapor pressure of the fuel droplet is determined by use of a weighted average, as done previously, through use of Equation 27. To determine the vapor pressure for a fuel Antione's equation, shown in Equation 28 as adapted from Lange's Handbook of Chemistry [26], can be applied where the values for *A*, *B*, and *C* are constants typically found using a reference text [27]. Note that P_v is the vapor pressure of the referenced fluid and *T* is the temperature of the fluid in question. The use of a weighted average of the fuel vapor pressures can be attributed to Dalton's Law of Partial Pressures [28].

$$P_{vf} = P_{v\,C_2H_5OH} * \varphi_{mix} + P_{v_{H_2O}} * (1 - \varphi_{mix}) \tag{27}$$

Equation 27: Vapor Pressure Weighted Average

$$\log P_v = A - \frac{B}{T + C} \tag{28}$$

Equation 28: Antione's Equation

The vapor pressure of water, if being used in the propellant pair, is determined using Tetens' equation, show in Equation 29, which was built specifically for estimating the vapor pressure of water *[29]*. Typically, this equation is only used between 0º and 35º Celsius but upon expanding the temperature range there is a slight loss in accuracy as shown in Table 4.

$$P_v = .61078 * e^{\frac{17.27*T}{T+237.3}} \tag{29}$$

Equation 29: Tetens' Water Vapor Pressure Equation

Table 4: Tetens Water Vapor Estimation Comparison

Temperature [C]	Tetens' Estimation [mmHg]	Recorded Vapor Pressure [27]	Percent Error
5	6.543	6.543	0.00%
25	23.760	23.756	-0.01%
50	92.53	92.51	-0.02%
100	766.66	760.00	-0.87%
120	1513.44	1489.14	-1.63%

The fuel droplet vapor pressure is then used in Equation 30 as adapted from *Atomization and Sprays* [23] to solve for the mass fraction of the fuel vapor at the surface with reference to the combustion chamber gas. Note that M_f and M_g are the molecular densities of the fuel and combustion chamber gas respectively, P_{cc} and P_{vf} are the pressure of the combustion chamber and liquid fuel vapor pressure respectively and Γ_{fs} is the fuel vapor mass fraction at the surface of the droplet.

$$\Gamma_{fs} = \frac{1}{1 + \left(\frac{P_{cc}}{P_{vf}} - 1\right) * \frac{M_g}{M_f}} \tag{30}$$

Equation 30: Fuel Vapor Mass Fraction

With this vapor pressure mass fraction, the mass transfer number can be calculated using Equation 31 adapted from Atomization and Sprays [23]. This mass transfer value is then used in Equation 32 to estimate the Nusselt number around the injected droplet for the purpose of eventually solving for the convective heat transfer coefficient of the combusting gas. Note that B_M is the mass transfer number of the droplet.

$$B_M = \frac{\Gamma_{fs}}{1 - \Gamma_{fs}} \tag{31}$$

Equation 31: Mass Transfer Number

To find this Nusselt number Equation 32 was adapted from *Atomization and Sprays* [23]. Once the Nusselt number is solved for, the determining of the convective heat transfer coefficient of the combusting gas is possible. In which *Nu* is the Nusselt number, *h* is the convective heat transfer coefficient and k_g is the thermal conductivity of the gas.

$$Nu = \frac{h * D}{k_g} = 2 * \frac{\ln(1 + B_M)}{B_M} \tag{32}$$

Equation 32: Nusselt Number Equality

At this point Nusselt number and droplet diameter were defined and an estimate for the thermal conductivity of the combusting gas was needed. This value can be estimated using a simulation of high pressure and temperature air in absence of real-world measurements. Several reference points, taken off of Figure 16, can be used to create a fitted curve with a 1st degree polynomial to derive an estimated for thermal conductivity at the estimated combustion temperature. Note that the units of bara in Figure 16 refer to pressure in atmospheric bar.

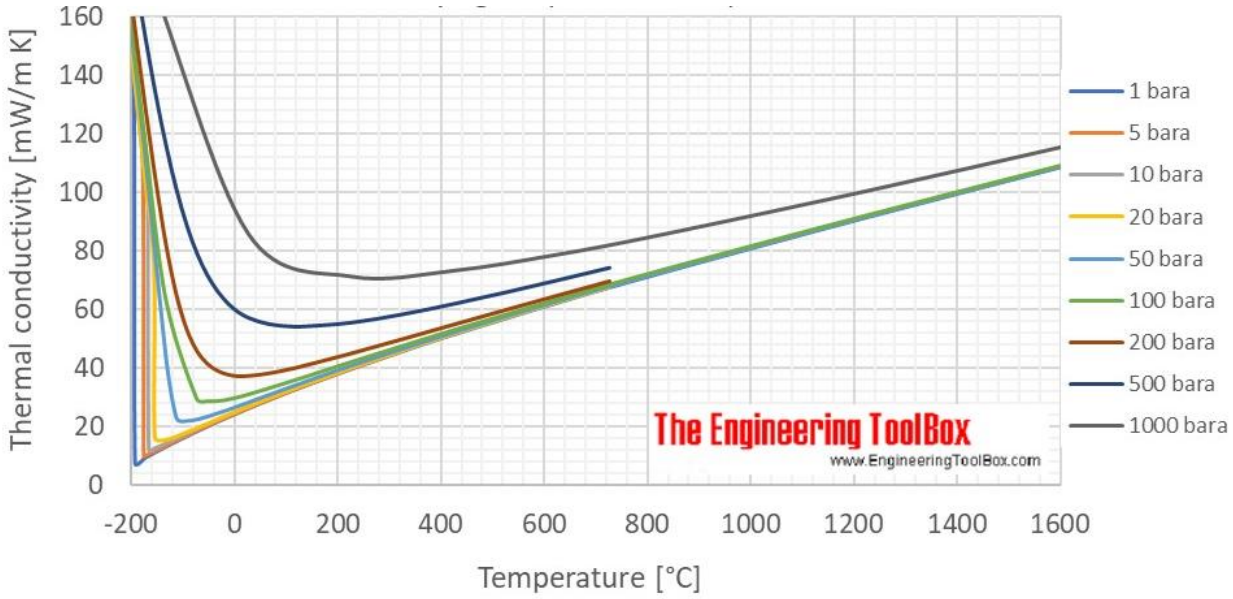

Figure 16: Air thermal conductivity at varying temperature and pressure [30]

With the convective heat transfer coefficient of the gas solved for, the heat transfer into the droplet from the surrounding environment estimation is made possible using Equation 33 adapted from *Atomization and Sprays* [23] to solve the heat flow into the droplet per unit time to allow for an iterative solution instead of a single estimation. Note that $\dot{Q}$ is the heat flowing into the system per difference in heat

$$\dot{Q} = \frac{\pi * D^2 * h * (T_\infty - T_s)}{t_{step}} \tag{33}$$

Equation 33: Heat Inflow to the Droplet

To calculate the rise in temperature of the droplet, Equation 34, adapted from *Atomization and Sprays* [23], was used in the same iterative loop. Note that m_d is the mass of the droplet and is determined before heating using Equation 35 adapted from *Atomization and Sprays* [23], where c_p is the coefficient of specific heat at constant pressure and T_s is the droplet surface temperature.

$$T_s = \frac{\dot{Q}}{c_{p_f} * m_d} + T_s \tag{34}$$

Equation 34: Droplet Temperature

$$m_d = \rho_f * {}^4/_3 * \pi * \left(\frac{SMD}{2}\right)^3 \tag{35}$$

Equation 35: Droplet Mass

At this point the boiling point of the propellant mixture is determined by, once again, taking a weighted average of the boiling point of each component at the combustion pressure. This weighted average is shown in Equation 36, where T_b is the boiling temperatures for the respective fluids [21]. As an azeotropic mixture ethanol and water will not boil separately so the weighted average will still be applicable. Note that a weighted average is not applicable for an ethanol water mixture with 95% ethanol due to a phenomena of boiling point minimum wherein the boiling point is lower than either fluid independently [31]. But even then, the difference in boiling points does not exceed more than 5% along the real boiling point line [31].

$$T_{b_f} = T_{b\,C_2H_5OH} * \varphi_{mix} + T_{b_{H_2O}} * (1 - \varphi_{mix}) \tag{36}$$

Equation 36: Fuel Droplet Boiling Point Weighted Average

This boiling point temperature was used as a termination point for the iterative method of heat addition to the system. Note that once boiling point has been achieved the mass transfer number B_M is equal to the transfer number B as shown in Equation 37 [23]. Typically, the density of the fuel droplet needs to be reassessed during each loop to account for change in fuel density during the heat up phase but as the fuel is being used for regenerative cooling it was injected at a

temperature very close to its boiling point which allows for a constant density to be assumed without much loss in accuracy.

6.5 Droplet Evaporation

At this point the mass transfer number solved above is reassessed to account for the change in temperature between injection and heat up using Equation 33, a large increase in the mass transfer number here is attributed to the fuel attaining its boiling point. Note that there exists a thermal transfer number as well, B_T, but this number is primarily used when using non-iterative methods of droplet heating. This distinction between the mass transfer number (B_M) and the thermal transfer number (B_T) is rendered moot once steady state evaporation begins, as once the boiling point of the droplet is reached both are equal to the transfer number, referred to as B [23]. With the transfer number now defined as in Equation 37 the evaporation constant can be solved using Equation 38, adapted from *Atomization and Sprays* [23], using the c_p of the combusting gas, the average fuel droplet density and the thermal conductivity of the combusting gas. Also note that λ_{st} denotes that the evaporation constant [23]. At this point an iterative loop is constructed to solve for the time required for a droplet to fully evaporate.

$$B = B_M = B_T \tag{37}$$

Equation 37: Transfer Number Equality

$$\lambda_{st} = \frac{8 * k_g * \ln(1 + B)}{c_{p_g} * \rho_f} \tag{38}$$

Equation 38: Evaporation Constant

This loop tracks the fuel droplet mass and the rate at which the droplet losses said mass. The truncation of this loop occurs at the point where the droplet mass drops to zero. The droplet initial

mass is equal to the droplet mass solved for in Equation 35. The change in fuel mass is determined using Equation 39 adapted from *Atomization and Sprays* [23] with the droplet diameter term, D_d, changing with each iteration.

$$\dot{m}_f = {}^{\pi}/_{4} * \rho_f * \lambda_{st} * D_d(i) \tag{39}$$

Equation 39: Droplet Evaporation Rate

The new droplet mass is calculated by implementing the droplet mass expulsion rate from Equation 39 into Equation 40, as adapted from *Atomization and Sprays* [23] and with this new mass the revised droplet diameter is calculated for input into Equation 39. The equation used to solve for the new droplet diameter is shown in Equation 41.

$$m_d = m_d - \dot{m}_d \tag{40}$$

Equation 40: Change in Droplet Mass

$$D_d = 2 * \sqrt[3]{\frac{m_d * 3}{\rho_f * \pi * 4}} \tag{41}$$

Equation 41: New Droplet Diameter

Each iteration adds to the previous timer count by the time step variable as shown in Equation 42 with the final value representing the evaporation term needed to find residence time.

$$t_{evaporation} = t_{evaporation} + t_{step} \tag{42}$$

Equation 42: Iterative Evaporation Time

6.6 Combustion

The last factor that could contribute to total residence time is the time required for combustion to occur. This factor can be ignored during determination of residence time as the combustion process is significantly faster than the previous three steps. In “Principles of Combustion” [32] under a list of common assumptions it is noted that the combustion chemistry is “infinitely fast”. Also, in *Rocket Propulsion Elements* [4], when looking at factors that can influence residence time, it is stated that “[gaseous] mixing is enabled by three-dimensional turbulent diffusion within the gas flows” and that “any liquid droplets that still persist in the upstream portion of the rapid combustion zone cannot follow the gas flow quickly”. These statements coupled together suggest that any atomized fuel particles that may still exist in liquid form will remain in the chamber until reacting with the gaseous oxidizer so long as combustion is occurring internally. As the effective flow speed inside of a combustion chamber is typically treated as stagnant or having a low axial flow speed until the converging diverging nozzle at the base it is reasonable to suggest that $t_{combustion}$ is effectively zero seconds and will be considered negligible in the characteristic length estimation. Note that this is not to say that the propagation of the flame front is infinitely fast but rather that the chemical process of combustion for any one molecule of fuel completes chemical combustion infinitely fast.

6.7 Characteristic Length

With all of the subsegment residence times determined, a total residence time is calculated using Equation 10 with the used residence time being the summation of all droplet phase times as shown in Equation 11, as adapted from *Modern Engineering for Design of Liquid-Propellant Rocket Engines* [5].

Note that another bounding factor is the minimum combustor length which denotes the length at which a particle of fuel would travel before completely combusting as shown in Equation 43. This must be taken into consideration when sizing the combustion chamber of an engine.

$$L_{min} = t_{stay} * V_{inj} \tag{43}$$

Equation 43: Minimum Chamber Length

For reference, characteristic length estimations for some typical propellant pairs are shown in Table 5 from *Modern Engineering for Design of Liquid-Propellant Rocket Engines* [5].

Table 5: Typical Combustion Chamber for Various Propellant Combinations

Propellant Combination	Combustion Chamber Characteristic Length (L*), in.
Chlorine trifluoride/hydrazine-base fuel	20-35
Liquid fluorine/hydrazine	24-28
Liquid flourine/liquid hydrogen (GH_2 injection)	22-26
Liquid fluorine/liquid hydrogen (LH_2 injection)	25-30
Hydrogen peroxide/RP-1 (including catalyst bed)	60-70
Nitric acid/hydrazine-base fuel	30-35
Nitrogen tetroxide/hydrazine-base fuel	30-35
Liquid oxygen/ammonia	30-40
Liquid oxygen/liquid hydrogen (GH_2 injection)	22-28
Liquid oxygen/liquid hydrogen (LH_2 injection)	30-40
Liquid oxygen/RP-1	40-50

What follows is an example of this process used to design a low-cost engine for ground testing in universities for the purpose of teaching.

7 Hephaestus Combustion Chamber Sizing

This section details the design constraints, segmented analysis of characteristic length, and sizing of the combustion chamber of Hephaestus. The characteristic length estimation using residence time is described as follows; the amount of time required for a droplet to form, the time required to heat said droplet to its boiling point, the time required for this boiling to completely convert the liquid droplet to a gas and the time required to combust the fuel.

7.1 Engine Design Constraints Example

Given that this engine is designed for use in the laboratory setting a moderate thrust of 100 pounds force or 444.8 Newtons was chosen. An Engine of this thrust level should be able to be mounted easily in a ground testing facility. Using NASA CEA an estimate for thermophysical properties of the combusted gas in the combustion chamber, throat and nozzle exit plane are shown in Table 6.

Table 6: NASA CEA Thermophysical Outputs

	Combustion Chamber	Throat	Nozzle Exit
Pressure [Ba]	34.474	19.846	0.97218
Temperature [K]	3055.76	2879.7	1899.01
Density [kg/m^3]	3.4925	2.1544	0.16443
Molar Density [g/mol]	25.74	25.992	26.706
Cp [kJ/(kg*K)]	3.9602	3.7027	1.7153
Ratio of specific heats	1.1429	1.1435	1.2236
Sonic Velocity	1062.1	10.26.3	850.5

Using the selected oxidizer fuel ratio of 3.75 and the total mass flow rate of 0.1866 kg/s in Equation 6 the fuel mass flow rate of 0.0393 kg/s was found [4]. The oxidizer mass flow rate of 0.1473 kg/s was then found by using Equation 7 with the solved total mass flow rate and fuel mass flow rate. Once all mass flow rates were calculated a throat area of 84.6 mm^2 and a throat radius of 5.19 mm were determined using Equation 8 and Equation 9 respectively.

7.2 Droplet Formation Example

As this was the beginning of the determination of L^* there was no defined injector port size yet so total fuel injector port diameters ranging from 2 mm to 3 mm were created. Those total injector port sizes were then partitioned into 2, 4, 6, 8, and 10 injector ports.

Fuel injection velocities, solved using Equation 14, in relation to injector port area and number of injector ports are shown in Figure 17. The generated output in Figure 17 can be used to find minimum chamber length as shown in Equation 43.

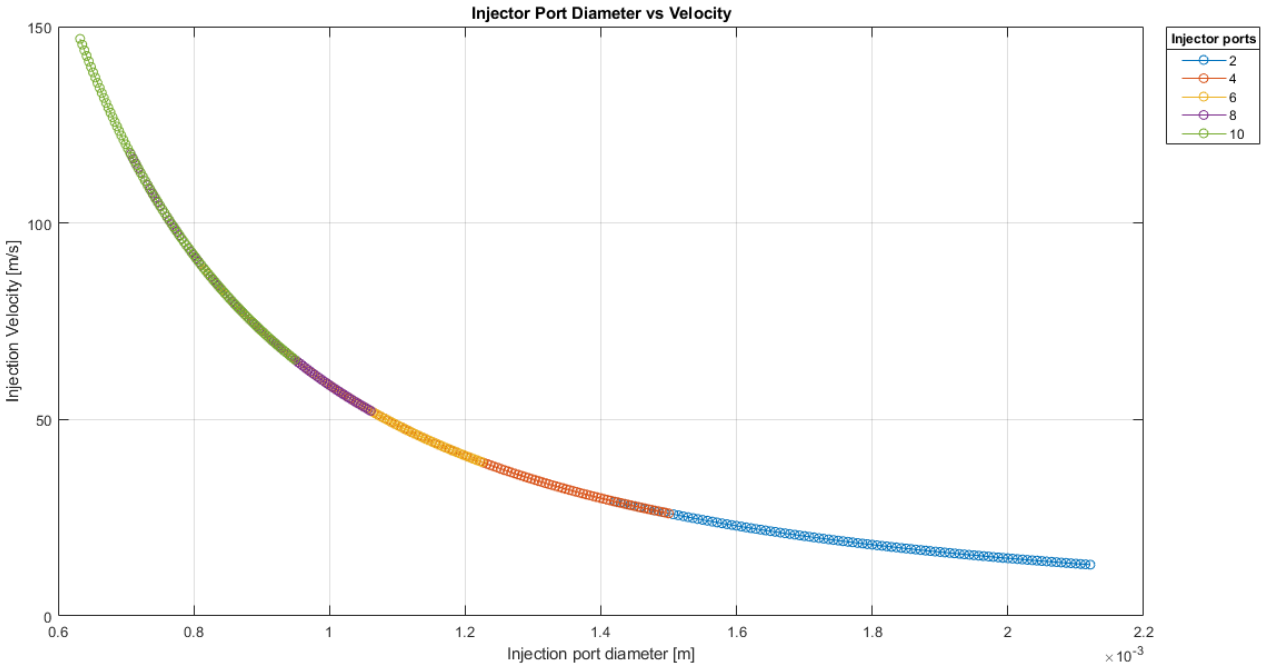

Figure 17: Injection velocity vs injection port diameter

The pure component densities are well defined for ethanol and water so these values are used in Equation 16 to return a fuel density of 851.4 kg/m^3 [21].

Equation 17 was used to determine a fuel dynamic viscosity of 4.897e-5 Pa*s assuming that a weighted average would be sufficient [21].

Using these values, the injection Reynolds numbers are shown on Figure 18. This graph suggests that any choice of orifice size and port number would result in turbulent flow as Reynolds number minimum for turbulent pipe flow is around 5000.

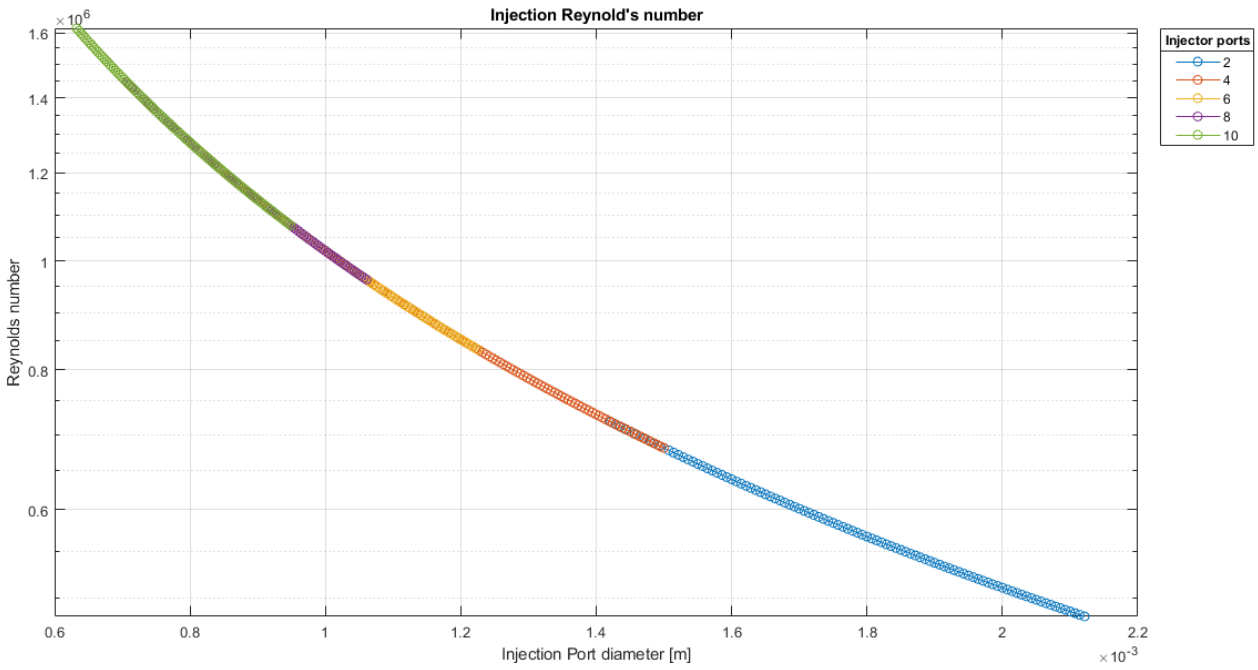

Figure 18: Injection Reynolds number

The dynamic viscosity of the air was taken at 3000 Kelvin and 3,447,400 Pascals and was based off of Sutherland's Law [24] shown in Equation 18.

Equation 19 was used to solve for the specific gas constant of air which was 287 J/(kg*K) and the specific gas constant of the combusting gas which was 323.1 J/(kg*K). The combusting gas was found to have an estimated viscosity of 8.6709e-5 Pa*s.

Equation 20 was used to solve for surface tension with an ethanol surface tension of 0.0041 N/m and a water surface tension of 0.038 N/m, the surface tension of the fuel was estimated at 0.0143 N/m [21].

Estimated SMDs are shown in Figure 19 and following an expected trend as shown in Figure 20 that as the flow rate through a single injector port and injector port area increase, so does the SMD. Along with this, data taken to produce the curves shown in Figure 21 used a relatively low temperature water which tends to have a viscosity an order of magnitude higher than that of the high temperature injected fuel mixture.

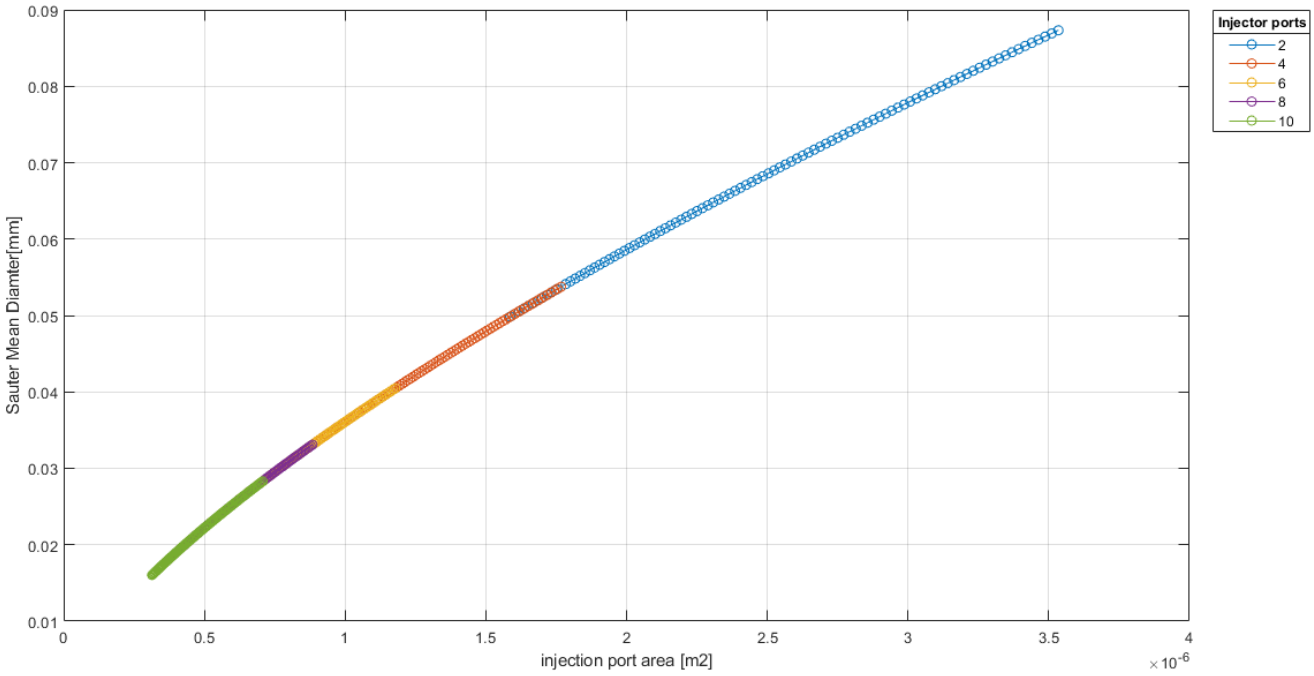

Figure 19: Sauter mean diameter estimation

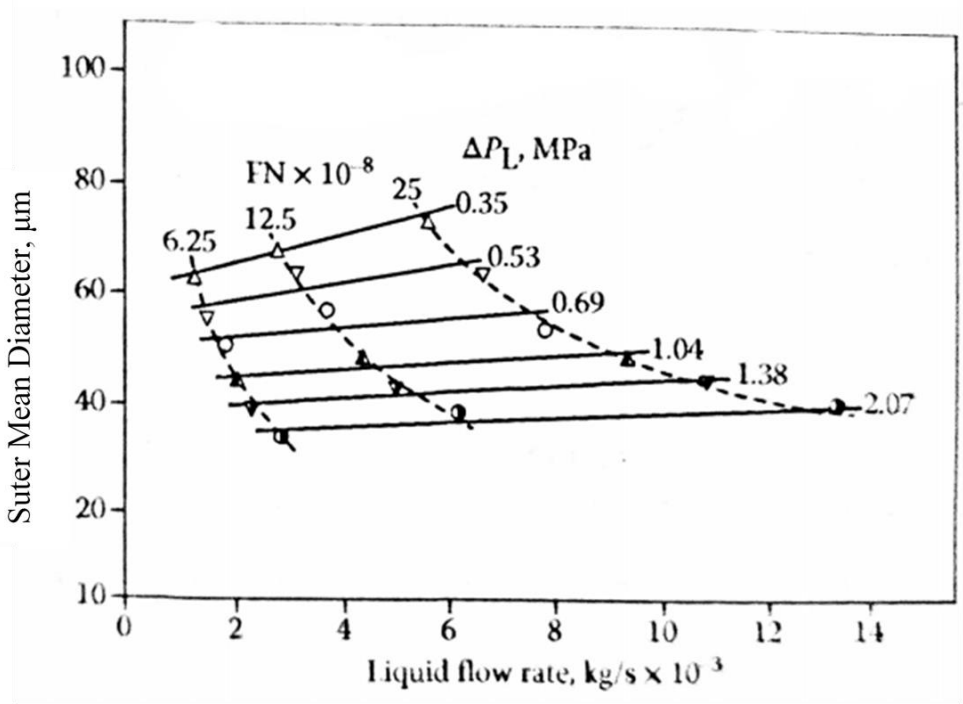

Figure 20: Relationship between SMD and liquid flow rate of water [23]

Applying the Baron correlation, the estimated jet breakup length is defined and was applied to the previously solved outputs to create Figure 21.

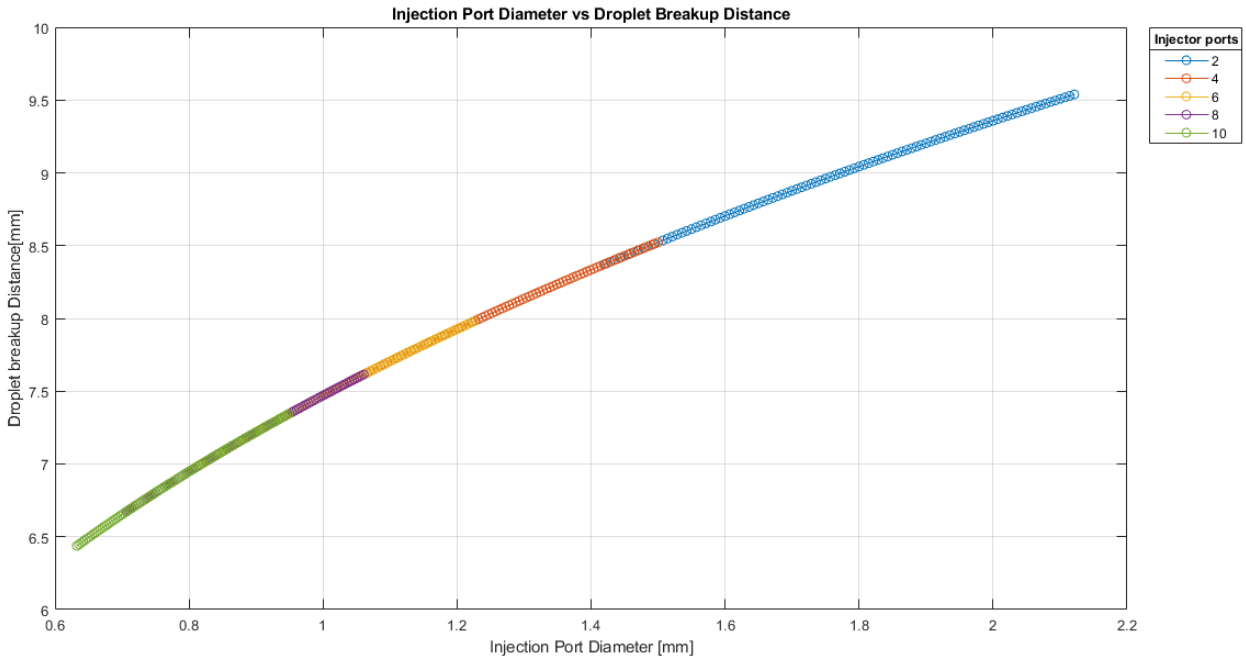

Figure 21: Droplet breakup distance using the Baron correlation

Combing the estimated jet breakup length and the injection velocity of the fuel in Equation 26 resulted in a jet breakup time which is shown in Figure 22. As expected, as droplet size increases with injector port diameter; the time required for the formation of the droplet also increases.

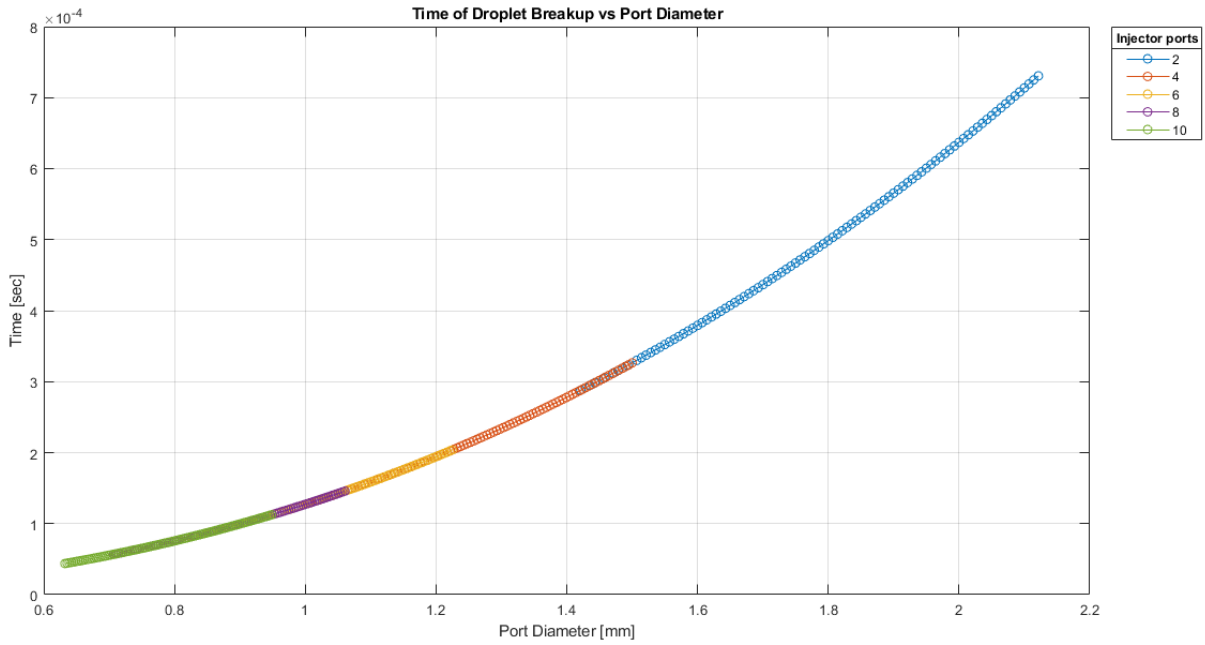

Figure 22: Droplet breakup time

7.3 Droplet Heating Example

To determine the vapor pressure for ethanol, Antione's equation, shown in Equation 28 adapted from Lange's Handbook of Chemistry [26], was applied where the values for *A*, *B*, and *C* are found in Table 7 using values from the National Institute of Standard and Technology (NIST) page on water [27].

Table 7: Antione Equation Variables

Constant	A	B	C
Ethanol	4.92531	1432.526	-61.819

The vapor pressure of ethanol was 2.763 MPa and the vapor pressure for water was 1.640 MPa which when applied in Equation 28, an average fuel vapor pressure of 2.426 MPa was found.

With this vapor pressure mass fraction, the mass transfer number was calculated using Equation 31 adapted from *Atomization and Sprays* [23] with 0.7765 as the fuel vapor pressure mass fraction as solved for in Equation 30. This mass transfer value of 3.474 was used in Equation 32 to estimate the Nusselt number around the injected droplet. This resulted in a Nusselt number of 1.375.

This value was estimated using a simulation of high pressure and temperature air. Several reference points were taken off of Figure 16 to create a fitted curve with a 1^{st} degree polynomial to derive an estimated for thermal conductivity at 3055 K. This resulted in an estimated thermal conductivity of 0.1825 J/(m*s*K). Applying this thermal conductivity value in Equation 32 resulted in Figure 23. The higher thermal conductivity is more favorable here as it should yield a faster droplet heating rate.

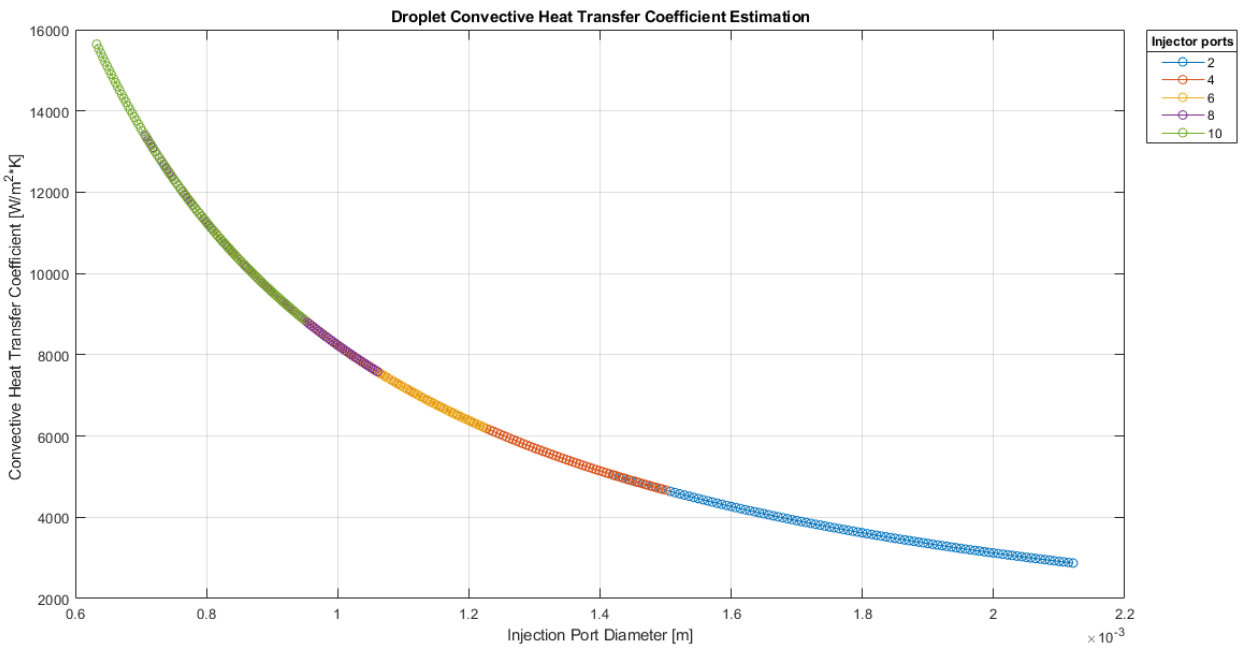

Figure 23: Convective heat transfer coefficient estimation

With boiling temperatures of 514.9 K for water and 479.15 K for ethanol, an effective boiling point of 489.9 K was designated for the ethanol water mixture. The temperature of the injected fuel being relatively close to its boiling point resulted in a fairly short heat up period of the droplet as shown in Figure 24.

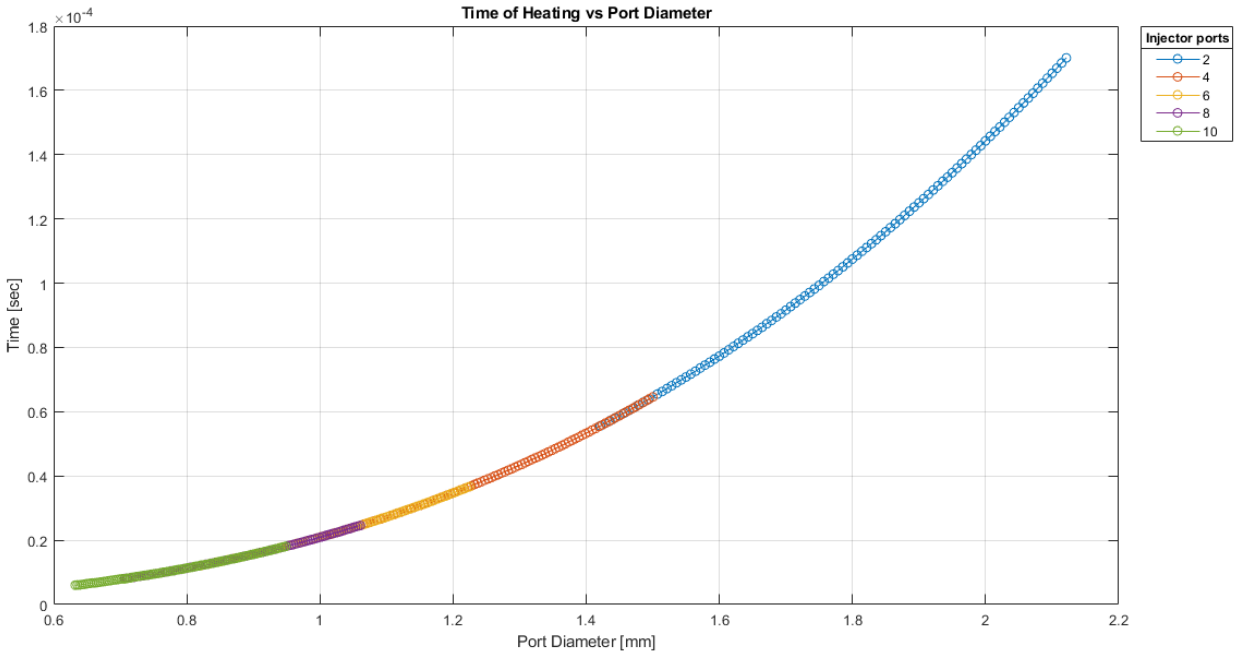

Figure 24: Droplet heat up time

7.4 Droplet Evaporation Example

At this point the previously solved mass transfer number was reassessed to account for the change in temperature between injection and heat up with the new mass transfer number, being 50.568 using Equation 33. The increase in the mass transfer number is due to the fuel attaining its boiling point [23]. This new Mass transfer number is the result of the fuel surface vapor pressure increasing to 0.9806 for the same reason as stated above using Equation 38 the evaporation constant was determined to be 0.6075 mm^2/s. At this point an iterative loop was constructed to solve for the time required for a droplet to fully evaporate. This loop was performed using Equation 39, Equation 40, and Equation 41.

This loop tracked the fuel droplet mass and the rate at which the droplet lost said mass. The truncation of this loop occurred at the point that the droplet mass dropped to zero. The amount of time required for droplet evaporation to occur is outlined in Figure 25. This plot suggests that a larger port diameter increases the amount of time needed for the droplet to evaporate. The

increased evaporation time here is to be expected as a larger port diameter creates a more massive droplet, hence the increased time to evaporate completely.

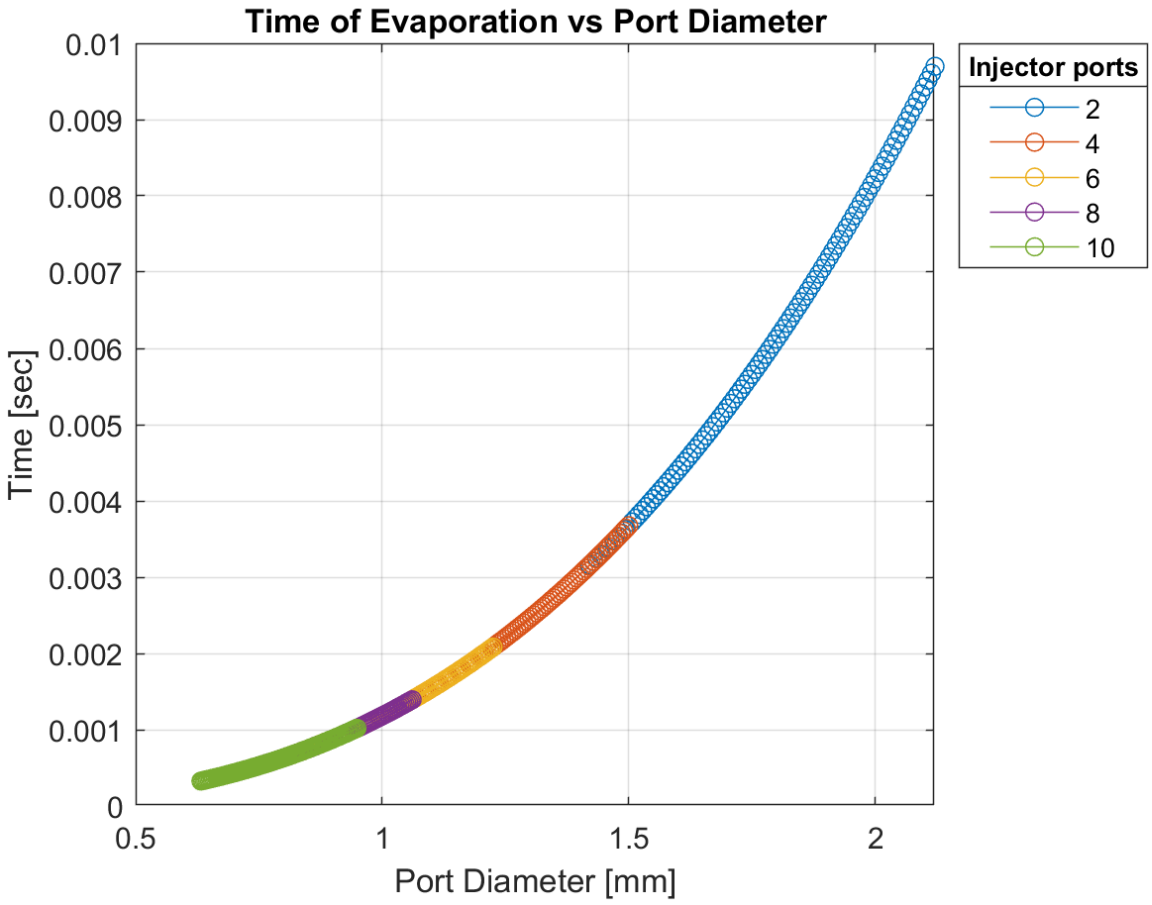

Figure 25: Droplet evaporation time

7.5 Combustion Example

As noted in section 6.6 the combustion time is effectively instantaneous [32].

Note that in order to simplify the chamber design, the ignition process will be started using a small mass of steel wool with electrical leads attached. This steel wool can easily be inserted just before testing begins and doesn't require constant maintenance that a design similar to a spark plug would need.

7.6 Characteristic Length Example

The summation of each portion of residence time is shown as residence time vs injection port diameter in Figure 26. This plot suggests that, with all other things being equal, an increase in injector port sizing causes an increase in residence time.

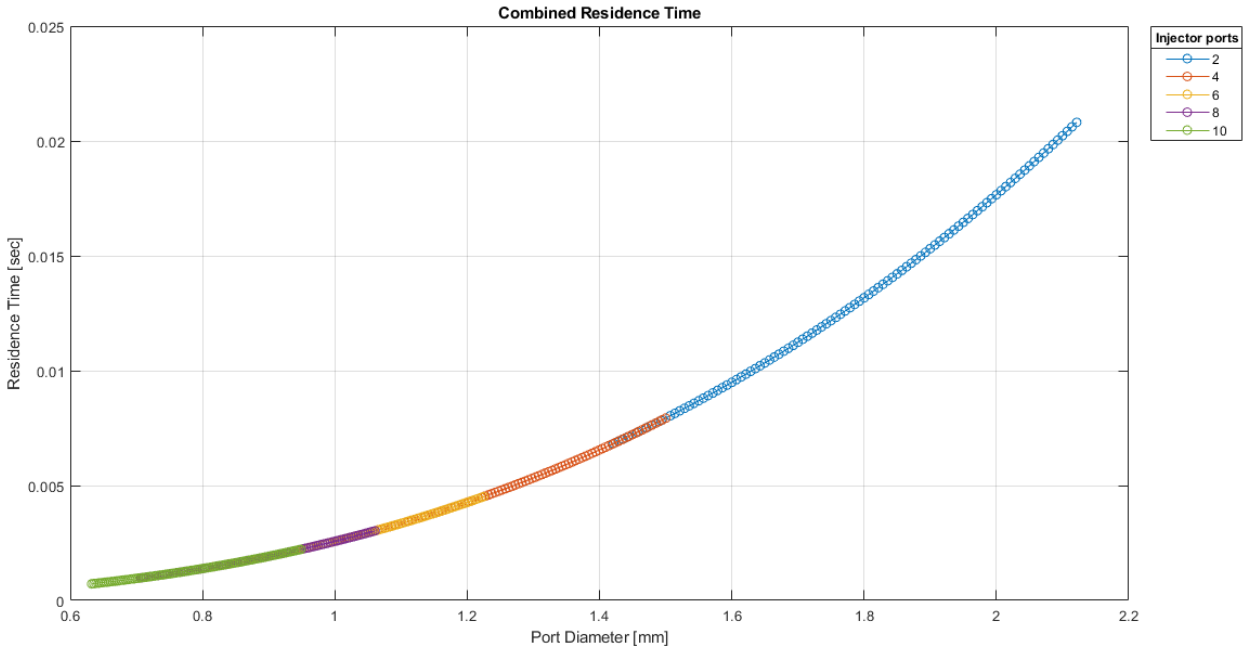

Figure 26: Combined residence time

The characteristic length vs injection port diameter graph in Figure 27 shows the application of Equation 10.

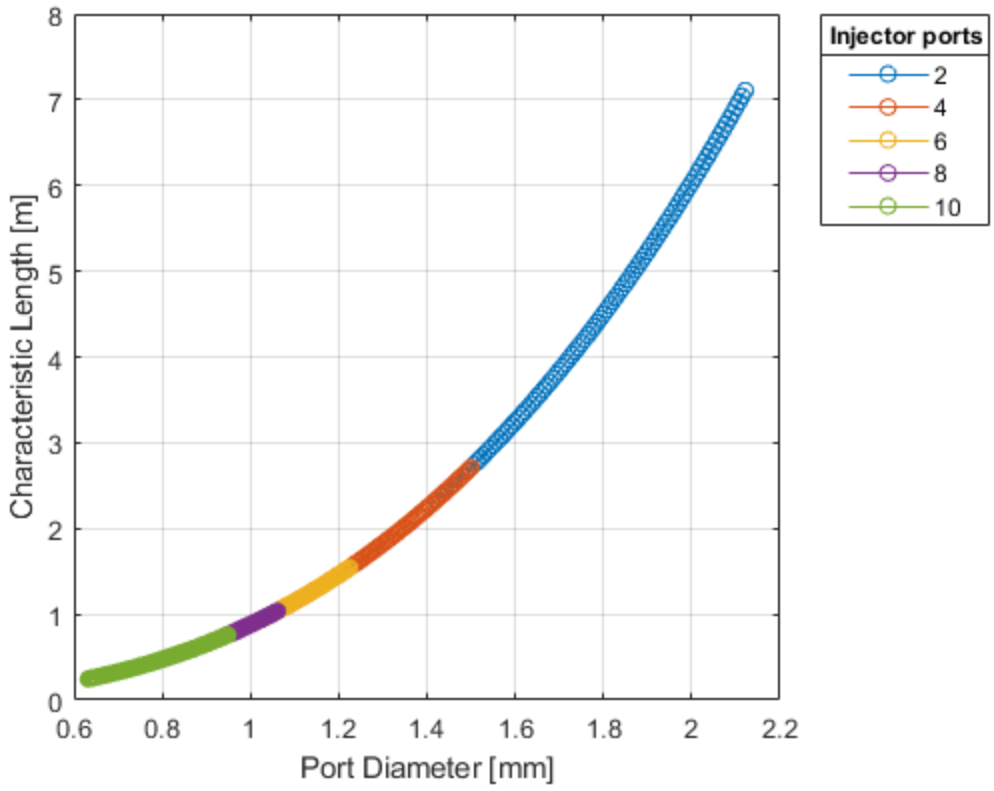

Figure 27: Characteristic length

This characteristic length estimation seems to fall within typical characteristic length estimations for propellant pairs as shown in Table 5 from *Modern Engineering for Design of Liquid-Propellant Rocket Engines* [5] on the bottom end but exceeds typical vales as the injector port diameter increases.

Another note is the only currently published estimation for an ethanol and nitrous oxide propellant pair from Youngblood states a single point characteristic length of 6.6 m [2] which is uncommonly high for a rocket engine as demonstrated in Table 5.

8 Hephaestus Engine Design

This section explores the realization of the design of Hephaestus including the design of the injector ports, how the choice of port size affects the work done in the estimation of L*, and the reasoning behind design choices of the Solidworks model. The design choices made pertaining to the model include the main chamber design, injector manifold, pressure sealant methods, plenum design and flange sizing.

8.1 Injection Port Sizing

With the characteristic length defined for a range of injector ports and port sizes the next step in the process was to choose an engine geometry based off of an L* and work on refining an engine design from there. The main concerns at this point included manufacturability of the injector plate and the effect the injector port sizing has on L*.

Firstly, the main factor of concern for the injector plate design was the injection port diameter for the fuel. Figure 27 suggests that the injector ports can be made to any diameter. While this is technically true, the main design driver that this engine could be produced at a low cost for a university, means that more typical drill sizes need to be used to guarantee no outrageous tool pricing or lead time for specialized drill bits. With an oxidizer constantly flowing through the injector plate in segments there was a need for oxidization resistant materials so SS 304 was chosen as the injector plate material due to its resistance to oxidization as well as its favorable thermal properties and relative strength compared to the printed $AlSi_{10}Mg$. With the material chosen the port diameter had to be determined next. Using Equation 44 adapted from *Rocket Propulsion Elements* [4] the graph seen in Figure 28 was produced.

$$P_{inj_{post}} = P_{inj_{pre}} - \frac{\left(\frac{\dot{m}}{C_d * A_{inj}}\right)^2}{2 * \rho} \tag{44}$$

Equation 44: Pressure Drop Across Injector Plate

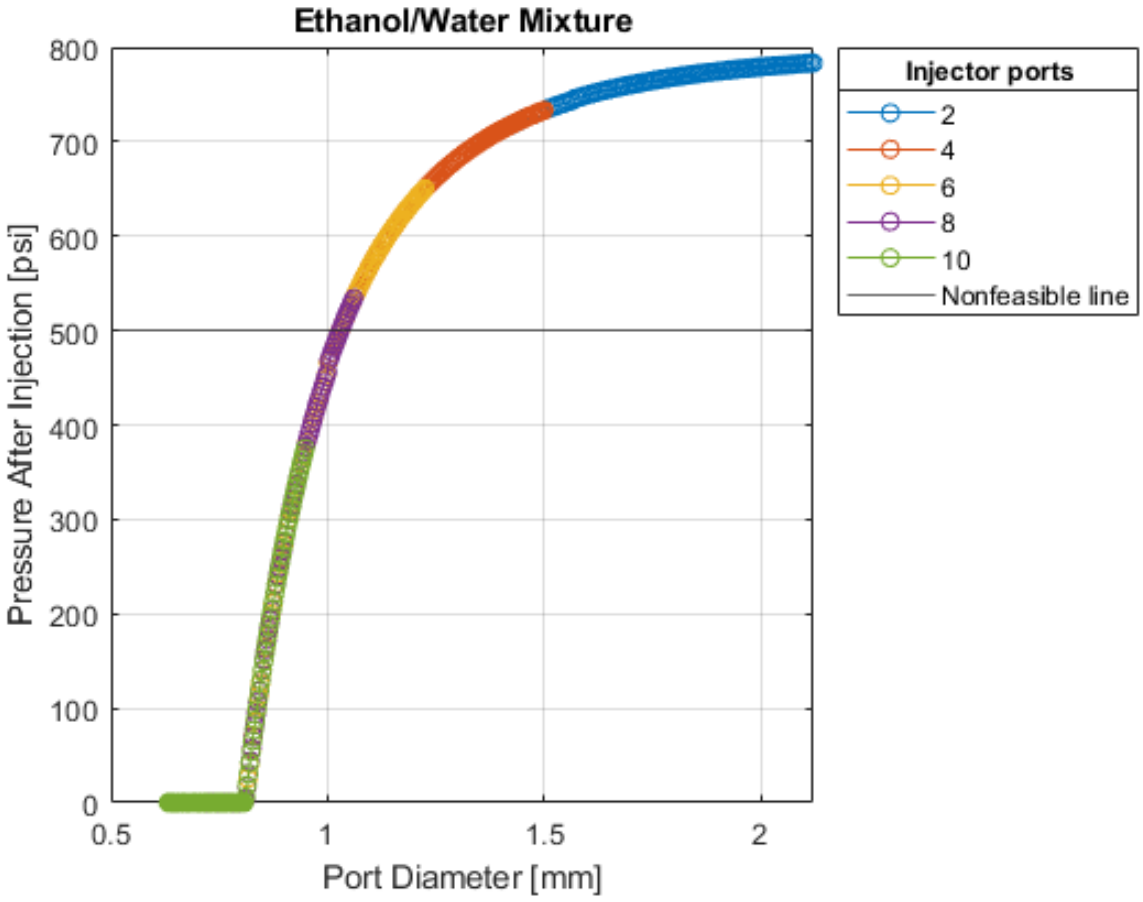

Figure 28: Fuel pressure drop across injector

The black line on this graph represents the combustion pressure and therefore the pressure required for injection to supply enough pressure for steady combustion. Note that a pressure buffer is desired here to mitigate pressure fluctuation complications. The equation breaks down as the ejection pressure approaches and passes 0 Pa but that point is already far past non-feasible conditions of injector.

With this it became clear that all 10 injector port options and most 8 injector port options were infeasible due to the pressure drop. With that information a 6-port injector configuration was chosen with an injection port diameter of 1.2 mm. This value allowed for a standard sized metric drill bit to be used. Next, the L* value was determined to be 1.4591 m based off of Figure 27 for a port diameter of 1.2 mm and 6 injector ports. With 1.2 mm injector ports for the fuel the oxidizer ports were forced to be 2.45 mm with 12 injection ports. These values were determined through an adaptation of Equation 45 from *Rocket Propulsion Elements* [4], wherein ΔP denotes a change in pressure before and after injection, and C_d is the coefficient of discharge of the related propellant.

$$\frac{\dot{m}_{ox}}{\dot{m}_f} = \frac{C_{d_{ox}}}{C_{d_f}} * \frac{A_{ox}}{A_f} * \sqrt{\frac{\rho_{ox}}{\rho_f} * \frac{\Delta P_{ox}}{\Delta P_f}} \tag{45}$$

Equation 45: Pressure Drop Relationships

In Equation 45 the P represents that difference in fluid pressure before and after moving through the injector. This pressure delta was expanded and used to solve for the oxidizer pressure after combustion by solving Equation 45 as shown in Equation 46 [4], where A is the total area of fuel and oxidizer ports.

$$P_{ox_{post}} = P_{ox_{pre}} + \frac{\left(\frac{C_{d_f} * OF * A_f}{C_{d_{ox}}}\right)^2 * \rho_f * \left(P_{f_{post}} - P_{f_{pre}}\right)}{\rho_{ox} * {A_{ox}}^2} \tag{46}$$

Equation 46: Oxidizer Pressure After Injection

This equation yielded the relative pressures shown in Figure 29. Note that the vertical jump from zero is a function of the above outputs in Figure 29 with fuel post injection pressure being zeroed when outputting a negative number to get rid of non-real results.

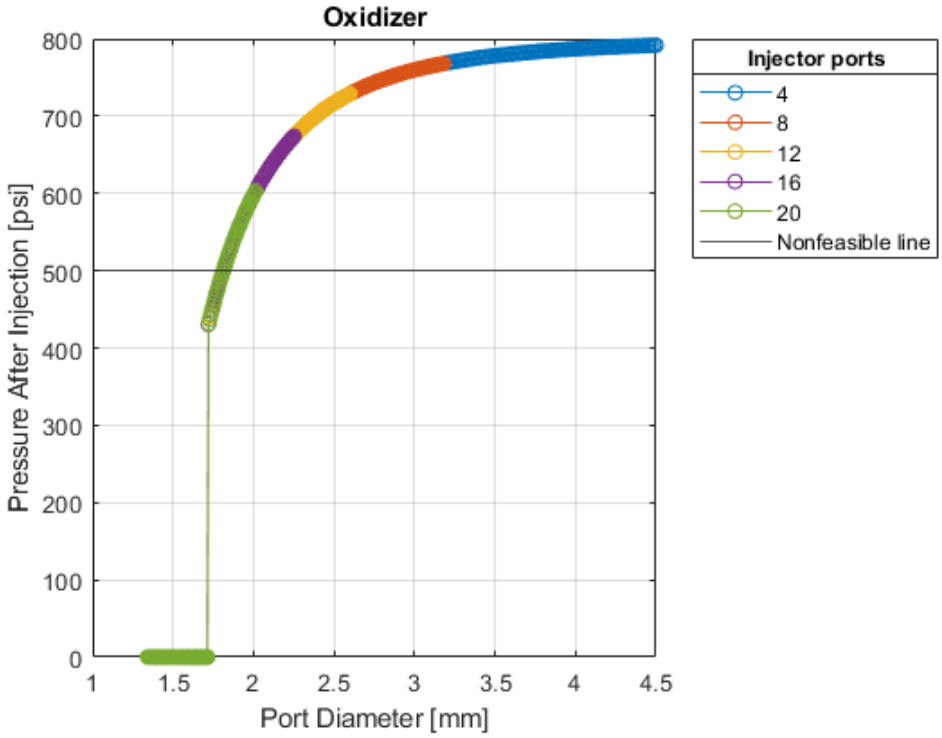

Figure 29: Oxidizer pressure drop across injector

With port diameters and number of ports decided an L* to represent the real engine could be chosen. This value was used as an input for engine sizing in the Rocket Propulsion Analysis software (RPA).

8.2 Solidworks Model

More detail is given in this subsection on the 3D modeling of Hephaestus and all immediately related components in the system. This subsection will include the design choices made for the main engine body, injection manifold, injector plate, pressure sealant methods and any feed line attachments or data acquisition attachments.

8.2.1 Main Engine Body Design

The creation of engine geometry for the internal surface of the engine was performed using RPA, which was exported to Solidworks. This main body curve, meaning the geometry of the innermost wall of the engine before the introduction of film cooling ports to the model, was copied and translated 1.0 mm further from the axial center to create the inner wall of the coolant flow line, and again 0.75 mm further to create the outer wall of the coolant flow line as established in RPA. Another copy was placed 5.0 mm past the outer wall of the coolant flow line to create the outer wall of the engine, this value was chosen to give the engine structural integrity for non-use times as sitting in a ground testing environment will likely yield external wear over time.

8.2.2 Injector Manifold

Typically, film injection at the top of the combustion chamber is included in the injector plate instead of being integrated into the combustion chamber. To facilitate this an additional section was added to the injector manifold to allow for the fuel for film coolant to flow separate from the fuel being used for combustion. The issue of an O-ring groove quickly became apparent as the groove sat in the vertical path for the film injection to flow straight through the injector. This was circumvented by drilling the film injection ports vertically from the top of the injector plate until level with the chamber side of the O-ring groove plate as shown in Figure 30. To complete the flow path a 0.5 mm diameter hole was placed at a 30-degree angle truncating once intersecting with the vertical hole. As shown in Figure 30 the hole in the top side of the injector plate was designed to be drilled in steps. The reason for this is that a drilled hole should not exceed five times its diameter in length [33]. This may however still be an issue in manufacturing as an exceptionally long bit relative to diameter would have to be used very close to the O-ring groove. If this presents itself as the case during manufacturing there are two viable alternate paths.

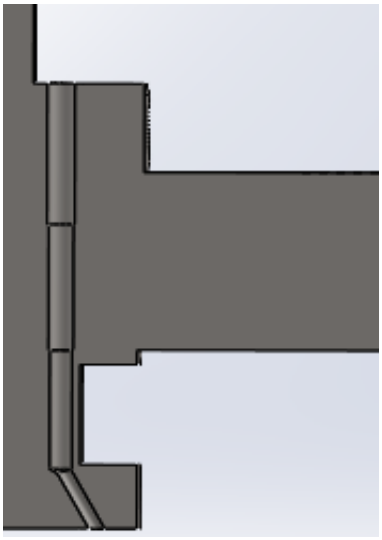

Figure 30: Film coolant injector plate port cutaway

The first would be to implement sinker electrical discharge machining (EDM) to create the vertical hole. This method of manufacturing would allow for the holes to be created without the restrictions of traditional drilling. Unfortunately, sinker EDM is quite expensive and most universities may not have easy access to sinker EDM on campus. While no quote was able to be attained this method is still undesirable due to the design of special tooling for the sinker EDM to be used. The second method of manufacturing would be to implement additive manufacturing again with a printed stainless steel. This process would yield a blank of the stainless steel with the shape of the overall design and the holes for the film cooling built in to the print. The main injection ports for this method cannot be manufactured using additive manufacturing due to the assumption made during the estimation of L* where a smooth injection port was modeled. Using only additive manufacturing for the injector plate may cause the injection ports to be too rough for that to still be a valid assumption.

8.2.3 Pressure Sealant Methods

In order to keep fluids in the correct flow paths, O-rings were implemented where possible. The O-rings allow for a high-pressure differential between any fluid region within the combustion

chamber or external environment. The main difficulty of designing with O-rings as the main pressure sealant is size. Most parts of the injector manifold were able to be sized to allow for the use of O-rings, specifically the required O-ring grooves. These grooves were designed using the Parker O-ring Handbook [34] which gives groove depth and width for each O-ring size available. These O-ring insertions can be seen in Figure 31 as the interfaces between the main chamber and injection manifold as well as between sections of the injection manifold.

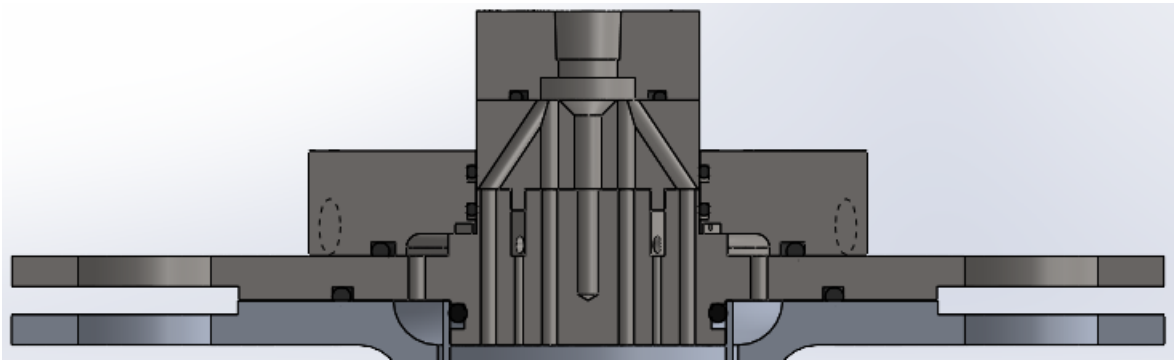

Figure 31: Injector manifold cutaway

Typically, during an engine firing the pressure differential will be nearly zero in between injector manifold sections, around 230 psi for the engine to injector manifold O-ring, and about 730 psi for the injector manifold to ambient conditions. The O-ring between manifold sections exists mainly to ensure that N_2O and the ethanol water mixture do not mix during flow. Note that O-rings are typically designed to handle pressures exceeding 1,000 psi so there is little risk of O-ring Failure [34]. In the case of the interface between the central fuel plenum and the injection lines for the N_2O injection no O-ring could be placed due to size restrictions. Instead, a high-pressure room-temperature-vulcanizing silicone (RTV) should be used for assembly, applied along the red lines shown in Figure 32. This RTV should serve as a strong enough barrier between N_2O and the fuel as the pressure differential during testing is on the scale of tens of psi.

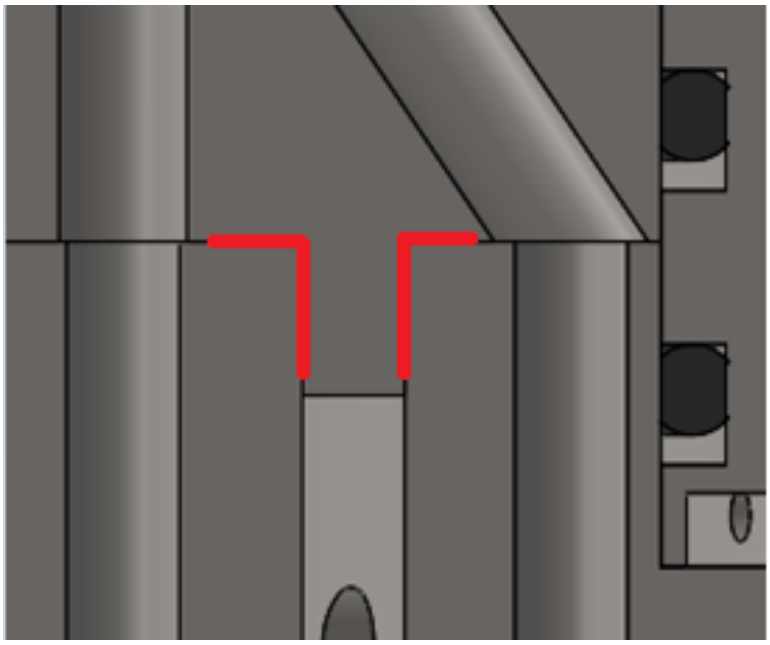

Figure 32: RTV application location in injector manifold

8.2.4 Plenums

As the inside face of the combustion chamber and nozzle are effectively axisymmetric, the flow of fuel through the lines had to be evenly distributed to allow even cooling throughout the engine. The concern with directly injecting to coolant ports and the regenerative cooling jacket was that fuel may favor flowing closer to the injection site, similar to Figure 33 from *Modern Engineering for Design of Liquid-Propellant Rocket Engines* [5] which displays the phenomenon of uneven fluid injection speeds in an injector plate. To avoid this uneven fuel flow, each injection site to a cooling line was accompanied by a plenum as shown in Figure 34. These plenums were sized, such that, the relative flow speed of the introduced fluid would be near zero to allow for even injection into coolant lines. Each plenum feed line was sized with a 1/8 NPT fitting port to allow for all

connections to share the same adapter design. Note that these ports will require post processing as additive manufacturing does not make a smooth enough surface to stop leakage through threading.

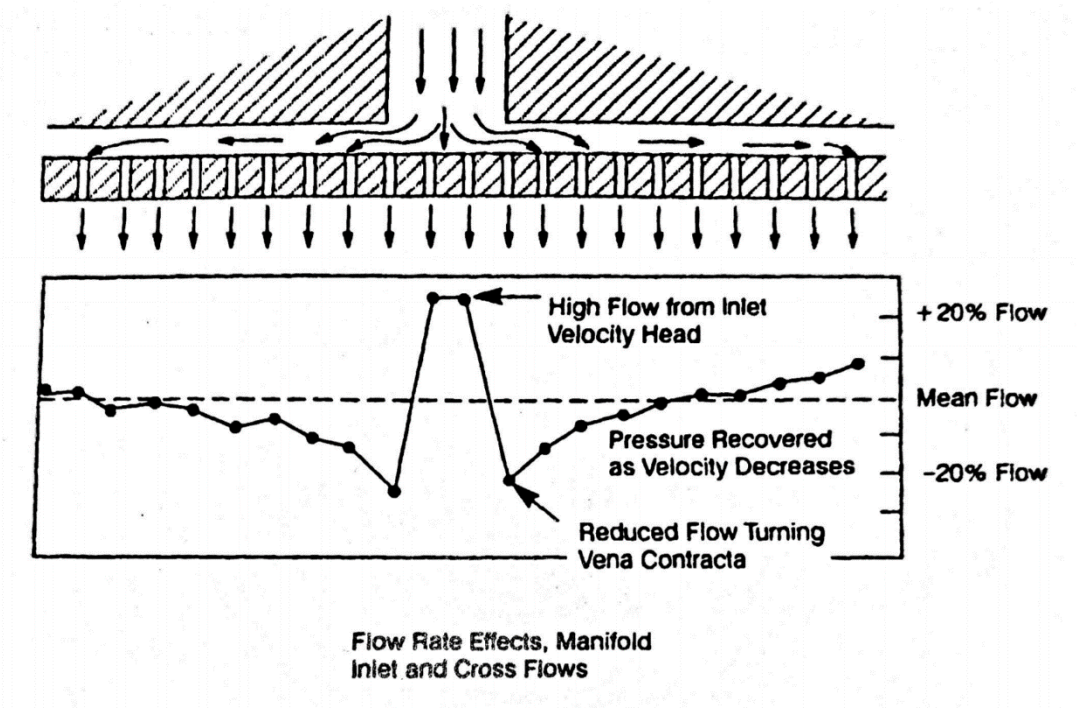

Figure 33: Fluid velocity effects in injector manifolds [5]

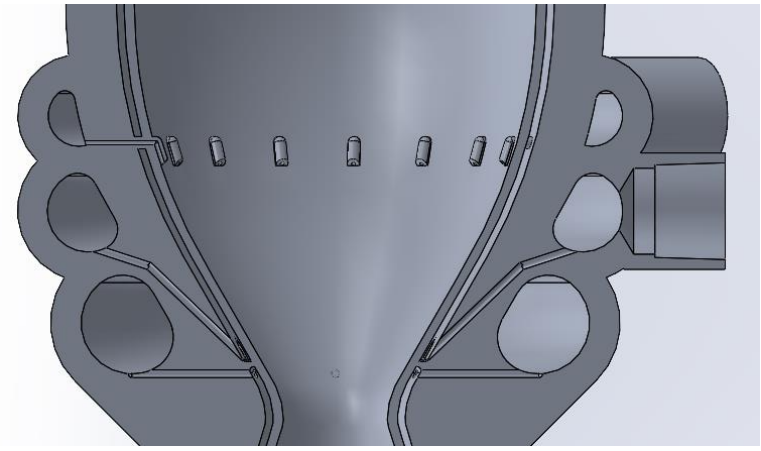

Figure 34: Plenum cutaway

There is an absence of a plenum for the outflow from the dump cooling segment next to the nozzle outlet because of the hot exhaust gasses' proximity to the dump line. To avoid the stagnation of

fluids so close to the plume three 1/8 NPT fittings were evenly spaced at a 45-degree angle pointing away from the plume, one of which is shown in Figure 35.

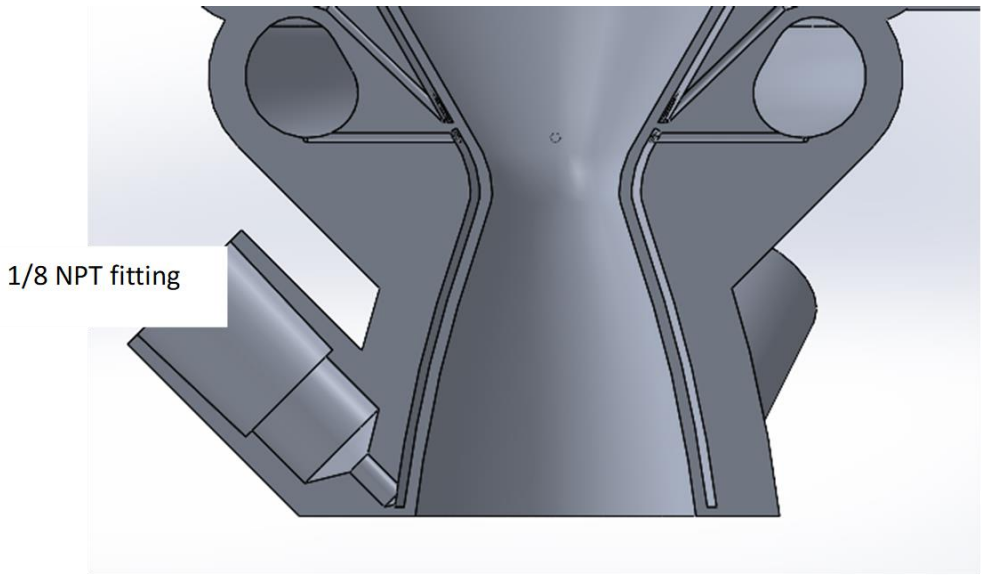

Figure 35: Hephaestus nozzle cutaway

8.2.5 Flange Sizing

The flange used to mate the injector manifold to the main combustion chamber was designed using ASME B16.5, the standard design process for pipe flange and flanged fitting design. Due to time constraints, ASME B16.5 gave a more practical answer than the design of a flange specifically for this engine setup. The chosen flange design was based around a 2-inch diameter flange as this value was the closest allowable to the combustion chamber diameter of 1.555 inches. The flange could not be designed for the smaller 1.5-inch option as undershooting may yield unexpected leakage. Hephaestus used a class 600 flange design as the class 400 flange designs in ASME B16.5 states that any class 400 flange for pipe diameters lower than 4 inches must use a class 600 design [35]. Note that the increase in flange class denotes an increase in maximum allowable flow pressure. As shown in Table 8 the maximum working pressure for a class 400 flange was 68.9 bar or about 1000 psi.

Table 8: ASME B16.5 Table 2-1.2 Working Pressure by Classes

Working Pressure by Classes, bar							
Class Temp., °C	150	300	400	600	900	1500	2500
−29 to 38	19.8	51.7	68.9	103.4	155.1	258.6	430.9
50	19.5	51.7	68.9	103.4	155.1	258.6	430.9
100	17.7	51.5	68.7	103.0	154.6	257.6	429.4
150	15.8	50.2	66.8	100.3	150.5	250.8	418.1
200	13.8	48.6	64.8	97.2	145.8	243.2	405.4
250	12.1	46.3	61.7	92.7	139.0	231.8	386.2
300	10.2	42.9	57.0	85.7	128.6	214.4	357.1
325	9.3	41.4	55.0	82.6	124.0	206.6	344.3
350	8.4	40.0	53.4	80.0	120.1	200.1	333.5
375	7.4	37.8	50.4	75.7	113.5	189.2	315.3
400	6.5	34.7	46.3	69.4	104.2	173.6	289.3
425	5.5	28.8	38.4	57.5	86.3	143.8	239.7
450	4.6	23.0	30.7	46.0	69.0	115.0	191.7
475	3.7	17.1	22.8	34.2	51.3	85.4	142.4
500	2.8	11.6	15.4	23.2	34.7	57.9	96.5
538	1.4	5.9	7.9	11.8	17.7	29.5	49.2

The allowable pressure is then exceeded in the class 600 flange design as that pressure of 103.4 bar or 1,500 psi is nearly double that of the maximum expected pressure in the engine of 730 psi in the propellant flow lines. The class 300 flange working pressure was only 51.7 bar or 750 psi which leaves the system of a factor of safety of only 1.03 which is far too low for a ground testing setup that could accidentally be over pressurized.

In the event that the flange design needs to be improved, *Modern Engineering for Design of Liquid-Propellant Rocket Engines* by Dieter Huzel and David Huang can be referenced, as chapter 9 goes into great detail on rocket engine specific flange design.

A factor that cannot be adequately addressed without a test print is potential warpage of the part due to the addition of a flanged connection. The large cross-sectional area of the flange can lead to warpage of the flange itself during the cooling process which could risk making the part

unusable. There are two possible solutions in the event that severe warpage is observed. The first of which is the thickening of the flange itself as adding more material would allow post processing to apply traditional machining to flatten out the flange top. Unfortunately, this may lead to the part holding internal stresses from the warpage that could affect the longevity of the engine. The second approach is to remove the flange from the additive manufacturing design entirely and use a brazed-on flange instead as suggested in a paper published by NASA on additive manufacturing of liquid rocket engine combustion devices [13]. This paper mainly details the brazed-on flange for engines printed in the GRCop family of powders so adapting this to $AlSi_{10}Mg$ will require additional analysis to be sure the braze behaves similarly.

9 Engine Modeling

This section explores the software used to create an engine model using inputs from MATLAB, NASA CEA and the model created in Solidworks. The heat transfer modeling utilized the Rocket Propulsion Analysis software. For structural modeling Solidworks was used for a preliminary test followed by a fully complex model being put through structural modeling in ANSYS. Some structural aspects that were not covered in the structural testing follow the ANSYS model. Lastly a system cost model was generated based on everything needed to ready the engine for physical testing.

9.1 Rocket Propulsion Analysis Software

The Rocket Propulsion Analysis software was used to generate specific engine geometries as well as to estimate the amount of heat being transferred into the system along the combustion chamber walls. The general inputs for the first iteration of Hephaestus are shown in Table 9.

Table 9: RPA Inputs

Parameter	Units	Input
Chamber Pressure	psi	500
Mass Flow Rate	kg/s	0.2086
Oxidizer Fuel Ratio	NA	3.75
Oxidizer	NA	N_2O (L) 298.15 K
Fuel	NA	C_2H_5OH (L) 70%
Contraction Area Ratio	NA	10
L*	m	2.71
Contraction Angle	Deg	30
Heat Transfer Analysis Type	NA	Ievlev

The ethanol and water mixture of 70% and 30% respectively was chosen as an initial estimate of how much water would be needed to close the heating loop but due to timing constraints and the mixture proving viable other ratios were deemed out of scope for this example of the engine design process. The Ievlev heat transfer analysis type is one of two built in heat transfer analysis types built in to RPA and is the assumed standard in the software. As shown in Figure 36, the Ievlev convective heat transfer analysis model estimates over the wall temperature when compared to the Bartz estimation. With this knowledge Ievlev was used for further analysis to keep the system running in possible higher assumed temperatures. In reality the heat transferred to the chamber wall is likely going to cause a wall temperature somewhere between the two.

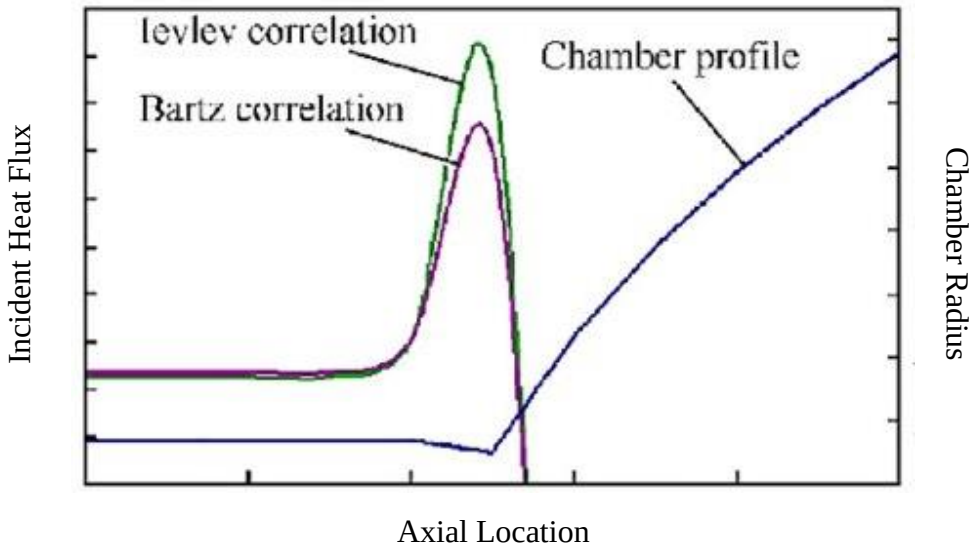

Figure 36: Convective heat transfer estimation Ievlev vs Bartz [36]

With these inputs and only radiative cooling applied to the system Figure 37 was developed to show the need for engine wall cooling. With only natural radiation of the chamber wall material, the wall temperature throughout the combustion section of the engine averaged to about 1,670 K with a large spike at the throat of the nozzle. This spike is to be expected as the nozzle is the location of maximum heat flux. The decrease in wall temperature is due to the decreasing pressure and temperature of the combustion products as the flow speed increases.

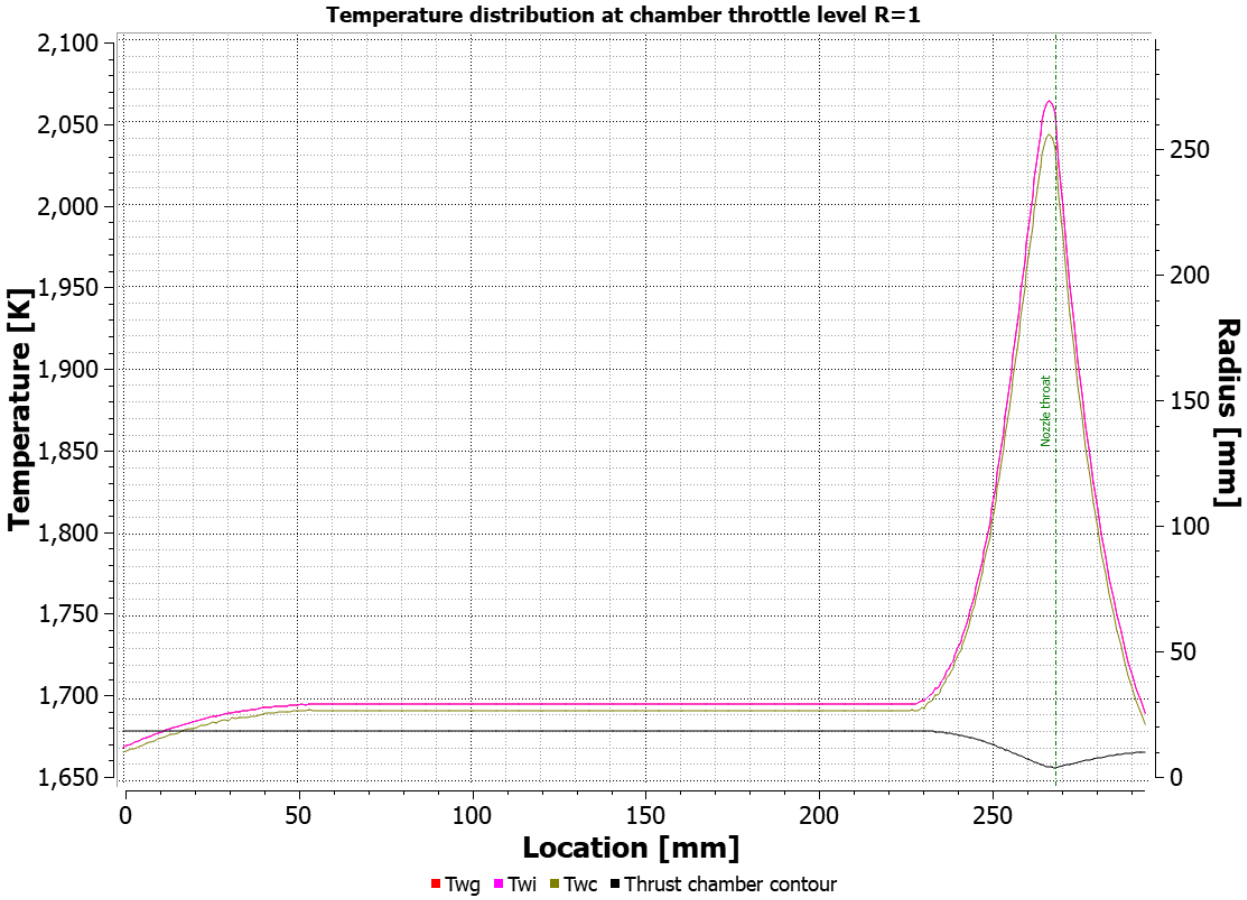

Figure 37: Chamber temperature radiation cooling only

For an example of this decrease in static temperature and pressure see Equation 47 and Equation 48 adapted from *Rocket Propulsion Elements* [4]. Note that the combustion chamber temperature and pressure are treated as the stagnation temperature and pressure due to the effective fluid flow speed being relatively close to zero. Where M is the Mach number of the fluid at the point in question.

$$T_{static} = \frac{T_{cc}}{1 + \frac{\gamma - 1}{2} * M^2} \tag{47}$$

Equation 47: Temperature Isentropic Relation

$$P_{static} = \frac{P_{cc}}{1 + \frac{\gamma - 1}{2} * M^2}^{\frac{\gamma}{\gamma - 1}} \quad (48)$$

Equation 48: Pressure Isentropic Relation

The clear problem presented by Figure 37 is the wall temperature minimum is over 1,650 K while the melting point of $AlSi_{10}Mg$ is 843 K and the material properties begin to degrade far below that temperature. To remedy this a regenerative cooling circuit was added to the system. This regenerative cooling circuit used only the ethanol water mixture as a coolant because N_2O has an incredibly low super critical temperature of 309.4 K [21] and will boil very easily. This combined with the volatility of N_2O made it too risky of a coolant for ground testing.

A coaxial shell was implemented as the shape of the cooling circuit with the coolant flowing against the general combusting gas flow direction. This was done to minimize temperature of the coolant at the throat of the nozzle where the highest heat flux was expected and because the cooling circuit ending at the top of the chamber decreases plumbing complexity near the injector face. An example of this layout is shown in Figure 38 adapted from Bradford's thesis on regeneratively cooled methane nozzles [37].

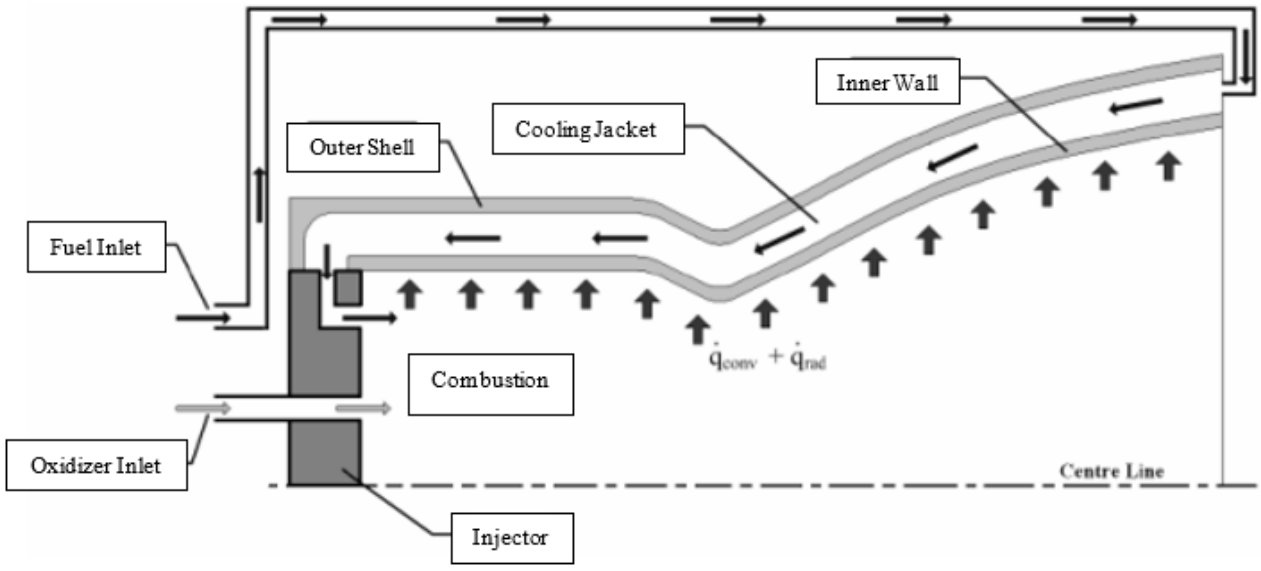

Figure 38: Coaxial regenerative cooling example [37]

With this method employed in RPA with the inputs shown in Table 10, the wall and coolant temperatures along the combustion chamber were determined as shown in Figure 39.

Table 10: Regenerative Cooling RPA Inputs

Parameter	**Units**	**Input**
Location	mm	0
Thermal conductivity of wall material	W/(m*K)	173.0
Inner shell thickness	mm	1.0
Distance between shells	mm	0.75
Coolant 1	NA	C_2H_5OH 70%
Coolant 2	NA	H_2O 30%
Relative mass flow rate	NA	0.208

The coolants were split into 70% ethanol and 30% water due to the fluid libraries in RPA. RPA has recorded data for mixed ethanol and water for the purposes of combustion analysis, but there

is no bank of information for thermophysical properties built in for the mixture. Thankfully pure ethanol and pure water were fully defined and seeing as in the analysis of characteristic length a weighted average was often taken this was not a large deviation from previous practices in this thesis.

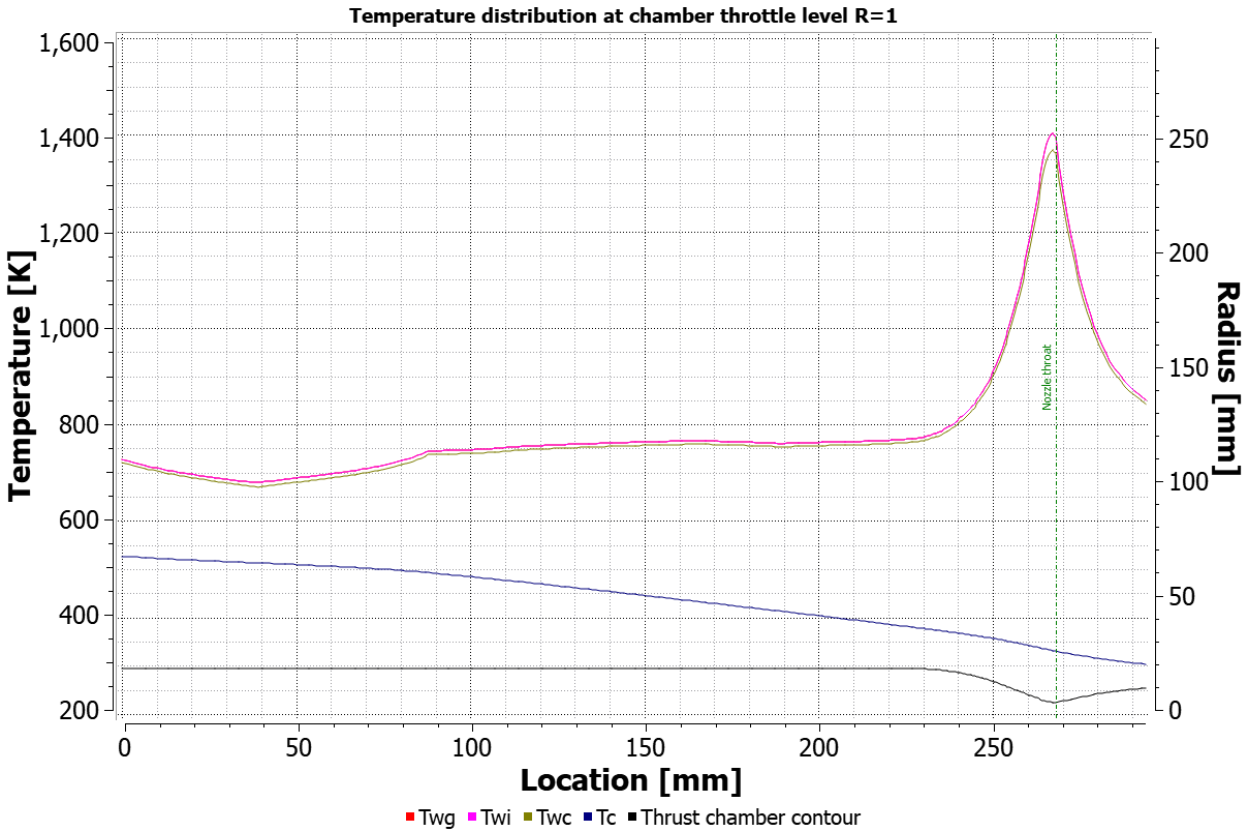

Figure 39: Regenerative cooling RPA temperature outputs

The decrease in wall temperature between 40mm and 90 mm was due to the temperature of the fuel mixture passing its natural boiling point at high temperature, which is referred to as nucleate boiling. This moved the heat transfer regime from forced convection to nucleate boiling as shown in Figure 2. The increase in temperature from 0 mm to 40 mm is due to the formation of the unstable gas film shown in Figure 2. These values are consistent with the estimated boiling point at the cooling line pressure being around 500 K. As the bubbles form from the boiling process the

heat is transferred as latent heat instead of sensible heat but the fluid temperature is low enough overall that the newly formed gas recondenses after leaving the hot surface wall of the chamber adjacent side of the cooling line. As the bulk temperature of the fluid continues to increase the fluid ceases to recondense after boiling off and a gas film forms from increased boiling [4].

The coaxial shell was chosen above other traditional coolant line shapes, namely tubular and channel wall designs, for simplicity of structural analysis. Coaxial shells have fairly axisymmetric thermal loading. In contrast to the coaxial shell thermal analysis, the interactions with nearby cooling channels need to be accounted for in the tubular and channel wall designs.

There was still a large wall temperature issue to address. The minimum wall temperature for the run with only regenerative cooling was around 670 K which, while lower than the melting point of $AlSi_{10}Mg$ was still far too high to maintain a high enough yield strength. Additionally, the peak temperature at the throat was 1,400 K which was still far too high. Another cooling method had to be added to the system as Figure 39 showed that regenerative cooling alone was not able to pull heat from the chamber walls fast enough to stop catastrophic engine failure.

The answer to this excess heating issue was found in the addition of liquid film cooling to the system. After finding that regenerative cooling alone was not sufficient for keeping wall temperatures down, further reading of *Modern Engineering for Design of Liquid-Propellant Rocket Engines* [5] revealed that “regenerative cooling is nearly always supplemented by some form of film cooling” [5]. The introduction of film cooling forces a change in the oxidizer fuel ratio of the combustion chamber. This brought the oxidizer fuel ratio from 3.75 down to 2.16. With this change in Oxidizer to fuel ratio an additional run of NASA CEA had to be performed to gain new combustion characteristics of the reaction which would then be used to determine the new effected characteristic length of the engine.

The same code expanded upon in the previous sections describing the determination of characteristic length was rerun with these updated values and the updated characteristic length was found to reduce from 2.71 m to 1.46 m. This reduction was due to a combination of several variables including the decreased combustion temperature and increased system mass flow rate. The new inputs to RPA for the film cooling segments of analysis are shown in Table 11.

Table 11: Film Cooling Injection Parameters

Parameter	**Units**	**Input**
Location 1	mm	0
Location 2	mm	33
Location 3	mm	90
Relative Mass Flow Rate 1	NA	.05
Relative Mass Flow Rate 2	NA	.05
Relative Mass Flow Rate 3	NA	.028
Coolant 1	NA	C_2H_5OH 70%
Coolant 2	NA	H_2O 30%

Note that location measurements began at the injector plate face. The location of the film coolant was determined by running RPA with only location 1 injection first. This produced a wall temperature plot that displayed a temperature spike where the liquid film atomized and became much less efficient as a cooling system. Gaseous film cooling systems tend to only be implemented in in hydro-lox systems. Gaseous film cooling is used in those systems because injected hydrogen turns gaseous very quickly because of its thermophysical properties as noted in *Modern Engineering for Design of Liquid-Propellant Rocket Engines* [5]. With the injection of the first liquid film layer the wall temperature was sufficiently low before becoming a gas, at which point

there was a sharp increase in temperature. The second film injection point was placed just before the temperature spike to avoid any point along the combustion chamber from not having liquid film cooling. This process was repeated again with third injection location. Applying these liquid film injection points resulted in the temperature graph shown in Figure 40. Note that with the decrease in characteristic length, the overall length of the combustion chamber went from 293 mm to 141 mm. The chamber contraction ratio remained to be 15.

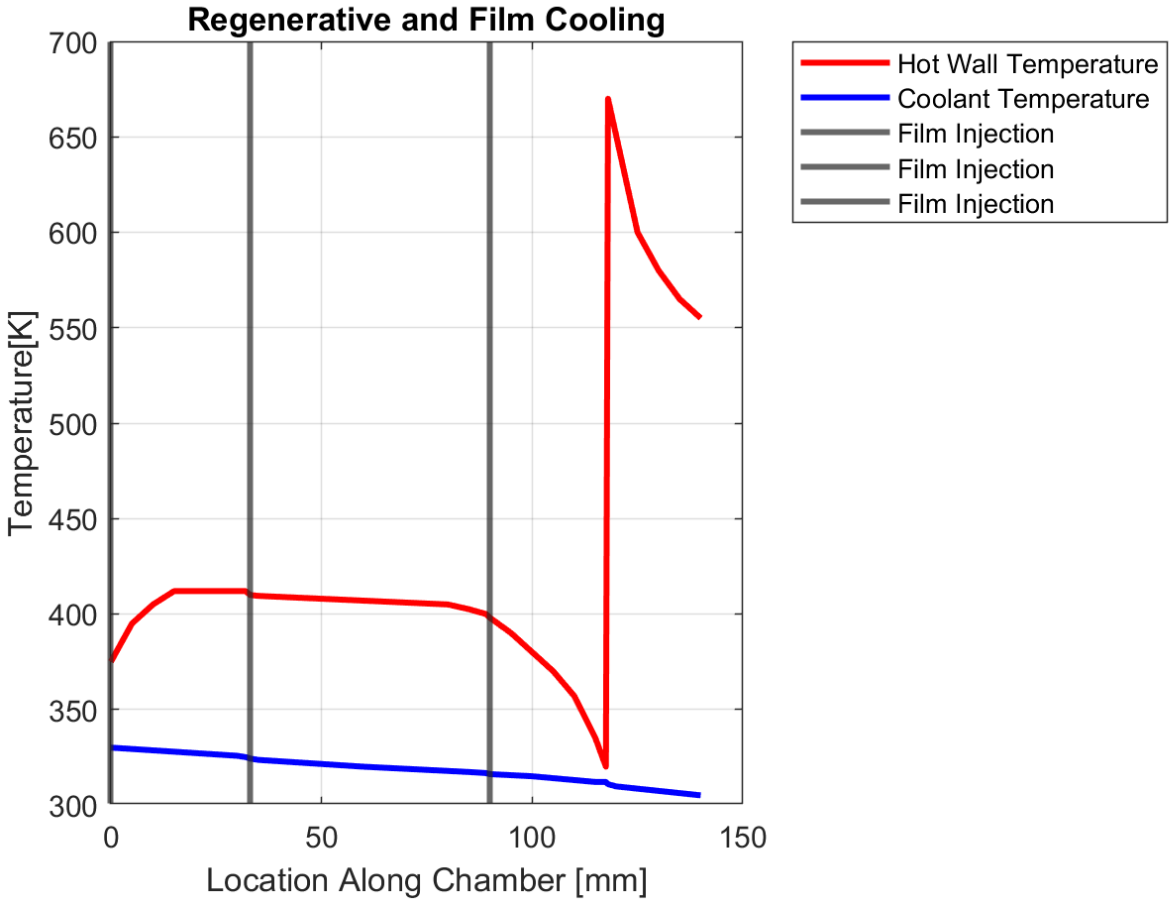

Figure 40: Regenerative and film cooling applied together

While this version of the model keeps the temperature of the chamber wall low enough to maintain structural integrity there was still the issue of the large temperature spike just after the throat. While film cooling proved useful in the main chamber the issue of supersonic flow in the nozzle prevents

its use after the throat due to the risk of introducing shock waves at the film injection ports. Liquid can be injected into the expanding section of a nozzle but only when the introduction of a shock wave is needed for thrust vector controlling and so published work on liquid injection without shock wave introduction is lacking. With this in mind another method of temperature control had to be implemented in this section of the engine. There are two other typical cooling methods that can be implemented. One option is a nozzle extension similar to the methods implemented in high altitude rocket nozzle extensions such as the one shown below from the SpaceX Merlin upper stage engine, pictured in Figure 41.

Figure 41: Merlin engine radiative cooled nozzle extension

Unfortunately, when regenerative cooling was removed from the supersonic nozzle and a tungsten extension was modeled in its place the temperature of the nozzle approached 2,000° C. While this temperature was not too high for the tungsten extension to withstand there would point at the interface with the printed aluminum part that could heat the aluminum beyond its allowable maximum temperature. This would have caused the bottom portion of the print to yield at the interface.

With the nozzle extension being no longer applicable the only other option is dump cooling. Dump cooling, as it sounds, dumps the used coolant off the side of the engine instead of routing the cooling fuel into the combustion chamber. In terms of the method of heat transfer from the chamber wall, dump cooling behaves identically to regenerative cooling. The main draw here is that the amount of fuel passing though the dump cooling line can be much higher than the actual amount of fluid passing into the combustion chamber. Typically, this isn't the case with dump cooling as a flight rocket wants to dump coolant as sparingly as possible but due to the ground test nature of Hephaestus, this is not a problem. The excess fuel used in dump cooling can be recaptured for later use which means that as far as a lab is concerned the dump cooling is a closed system and no fuel is wasted.

RPA does not have a built-in function for dump cooling but because of its similar behavior to regenerative cooling this modeling system could be implemented and the fuel used for this cooling would not be treated as entering the combustion chamber. On top of this issue, RPA is not able to implement several different regenerative cooling sections in a single run, nor is it capable of beginning a cooling circuit in the center of an engine and then running the coolant flow counter to the main engine flow direction. Thankfully this issue could be solved by superimposing two runs over one another, one with the film and regenerative cooling implemented and another with the film and dump cooling implemented. This dump cooling run implemented a coolant mass flow rate equal to the total propellant mass flow rate moving through the combustion chamber. The full implementation list can be seen in Table 12.

Table 12: Dump Cooling Inputs

Parameter	Units	Input
Location	mm	115
Thermal Conductivity of wall material	W/(m*K)	173.0
Inner Shell Thickness	mm	1.0
Distance Between Shells	mm	0.75
Coolant 1	NA	C_2H_5OH 70%
Coolant 2	NA	H_2O 30%
Relative Mass Flow Rate	NA	1.0

These inputs generate the chamber wall temperature output in Figure 42. With the dump cooling run the maximum nozzle wall temperature was found to be just over 500 K which is inside the operating bounds of the printed $AlSi_{10}Mg$ and effectively closed the system cooling. Note that coolant at 0 K is not actually present in the system but is an artifact of how RPA generates plottable data sets.

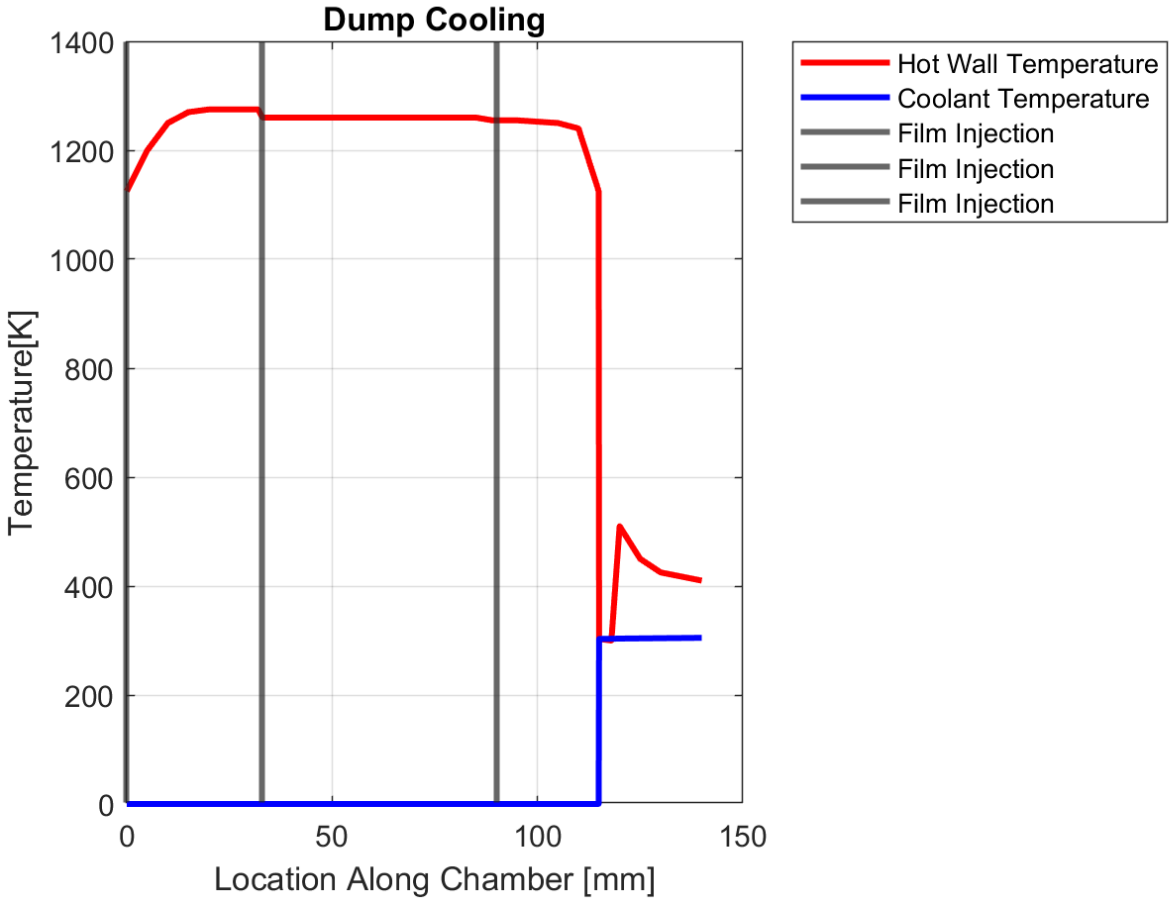

Figure 42: Dump and liquid film cooling RPA output

The combination of both the dump cooling and regenerative cooling circuits being implemented can be seen in Figure 43.

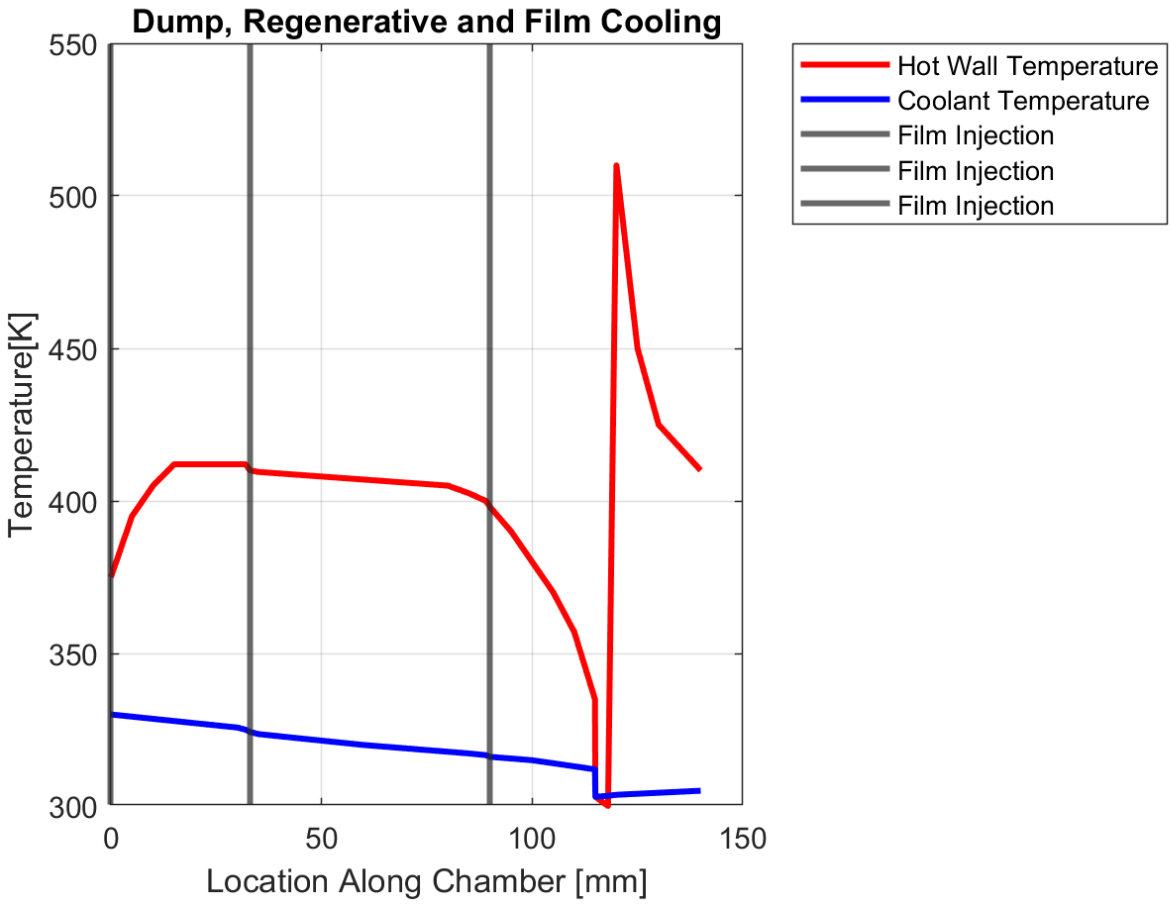

Figure 43: Film cooling applied alongside regenerative and dump cooling

The implementation of film cooling introduced an issue of the actual film coolant injection design. Though there is no published value for an absolute maximum or minimum injection velocity for an injected film coolant, it must stay relatively slow to avoid aerosolizing too quickly and unintentionally converting to a gas film cooling. The maximum allowable injection velocity then was defined as keeping the injected coolant film below a compressible regime at 0.3 Mach. Using a weighted average shown in Equation 49 the sonic velocity of the injected coolant was determined to be 1256 m/s with water having a sonic velocity of 1482 m/s and ethanol having a sonic velocity of 1159 m/s [30]. This Mach number resulted in a maximum injection velocity of 367.8 m/s. This maximum injection velocity, ended up being much higher than the designed injection velocity due

to fabrication limitations on film injection geometries, these limitations will be explored further below. Wherein *M* is the Mach number at injection.

$$M_{1_f} = M_{1_{C_2H_5OH}} * \varphi_{mix} + M_{1_{H_2O}} * (1 - \varphi_{mix}) \tag{49}$$

Equation 49: Liquid Coolant Mach Number Weighted Average

The axial location was determined in Rocket Propulsion Analysis to be at 0 mm, 33 mm and 90 mm from the beginning of the combustion chamber relative to the injector plate. With this knowledge and the geometric output from RPA the radius at the above listed locations were determined to be 19.75 mm, 19.75 mm and 17.23 mm respectively. With the radii known the next step was to determine the sizing and shape of film injection. A design incorporating a slot covering the entire circumference of the film injection site was investigated. With the above radii, the circumference at injection points were found to be 124.01 mm, 124.01 mm and 108.26 mm.

The next value that had to be determined before completing the sizing of the film injection orifice was the injection velocity. Using Equation 50, adapted from *Rocket Propulsion Elements* [4], a relationship between area and injection velocity was created.

$$V_{inj} = \frac{\dot{m}}{\rho_{fuel} * A_{inj_{film}}} \tag{50}$$

Equation 50: Injection Velocity from Mass Flow Rate

Equation 51 solves for the area of the slot film injection using the height and circumference of the slot. Using the circumference and height from Equation 51 the injection velocity was solved as shown in Equation 52 as adapted from the mass flow rate equation in *Rocket Propulsion Elements*

[4]. The outputs of Equation 52 are show in Figure 44. Note that $h_{inj\ film}$ is the height of the film injection slot.

$$A_{inj_{film}} = Circ_{inj_{film}} * h_{inj_{film}} \tag{51}$$

Equation 51: Film Injection Area

$$V_{inj} = \frac{\dot{m}}{\rho_{fuel} * Circ_{inj_{film}} * h_{inj_{film}}} \tag{52}$$

Equation 52: Injection Velocity from Slot Height

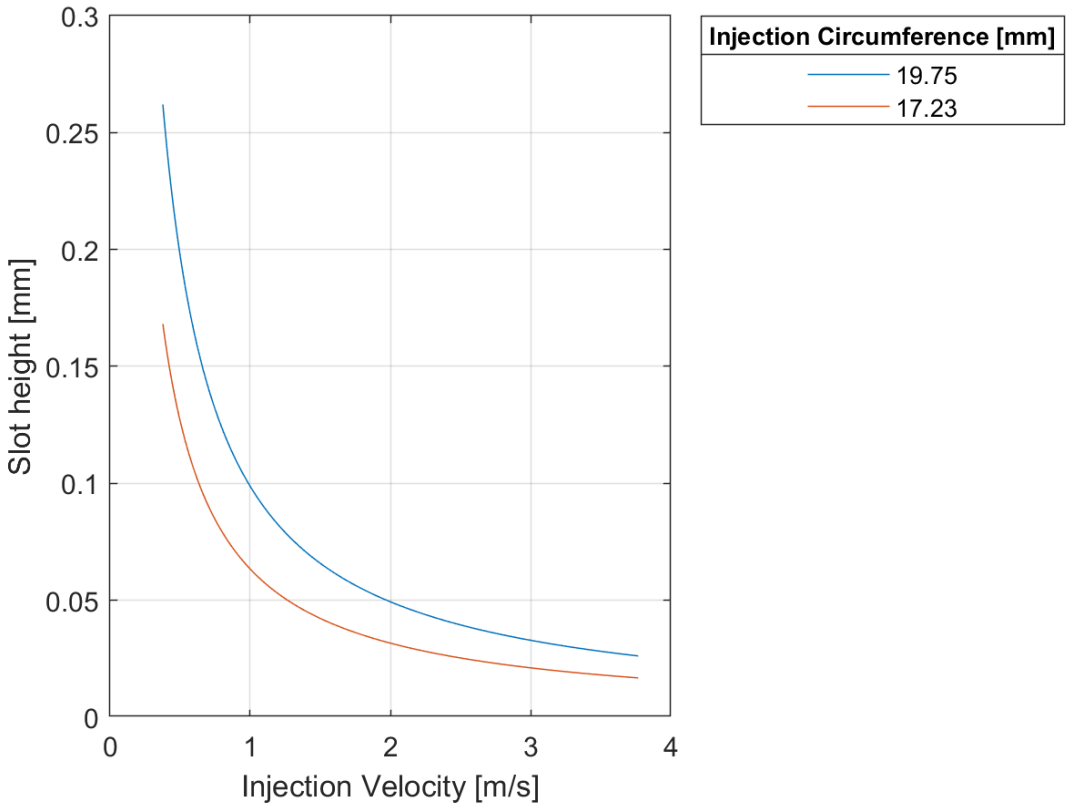

Figure 44: Injection velocity vs injection slot height

Though the injection velocities in Figure 44 fall well within the upper bound of injection velocity there still exists the issue of the manufacturing of the part. If the preferred injection velocity was

1 m/s the slot heights would be about 0.065 mm and 1 mm relative to location along the combustion chamber. While this is above the minimum layer height of 30μm [38] the possible deformation of an unsupported overhang with that large of a radius could result in the creation unintentional and uncontrollable hot sports after injection. With this in mind the use of slot injection for film cooling was abandoned and a more classic injection port design was explored.

Switching from a slot design to a multi-port design allowed for an increase in feature size to increase manufacturability. Equation 50 was used once again but injection area was determined using Equation 53 as the area had changed from the wall of cylinder to the area of multiple circular injector ports where *N* is the number of coolant ports.

$$A_{inj_{film}} = N * \pi * r_{inj_{film}}{}^{2} \tag{53}$$

Equation 53: Area of Multiple Film Injection Ports

Inserting Equation 53 in to Equation 52 yielded Equation 54 where $r_{inj\ film}$ is the radius of the film injection layer as adapted from the mass flow rate equation in *Rocket Propulsion Elements* [4].

$$V_{inj} = \frac{\dot{m}}{\rho_{fuel} * N * \pi * r_{inj_{film}}{}^{2}} \tag{54}$$

Equation 54: Injection Velocity of Circular Port Film Injection

The number of injection ports for each film cooling injection set was found next. Typically, the introduction of film cooling is iterated upon between tests but, as physical testing is out of scope for this thesis, an initial iteration method is all that could be applied. The number of required injection port locations was determined through use of spacing suggested in *NASA Special Publication 8087 Liquid Rocket Engine Fluid-cooled Combustion Chambers* where “it is

recommended that no less flow be used than that controlled by 0.381 mm diameter orifices spaced 7.62 mm apart" [39]. This spacing restriction coupled with the above-mentioned circumferences were implemented in Equation 55 to determine the number of injection ports per film cooling set mentioned above in Equation 53 and Equation 54 where $Circ_{inj\ film}$ is the circumference of the film injection ring of ports.

$$N = \frac{Circ_{inj_{film}}}{7.62} \tag{55}$$

Equation 55: Required Number of Film Injection Ports

In cases where the number of injector ports was not an integer the value should be rounded up to ensure the 7.62 mm spacing was not exceeded. The spacing recommendation resulted in 17 film cooling ports for the film injection sites at 0 mm and 33 mm relative to the injector face and 15 injector ports for the film coolant injection location and 90 mm relative to the injector face. With this number of injection ports Figure 45 shows the film coolant injection velocity relative to the injector port area of a single film coolant port.

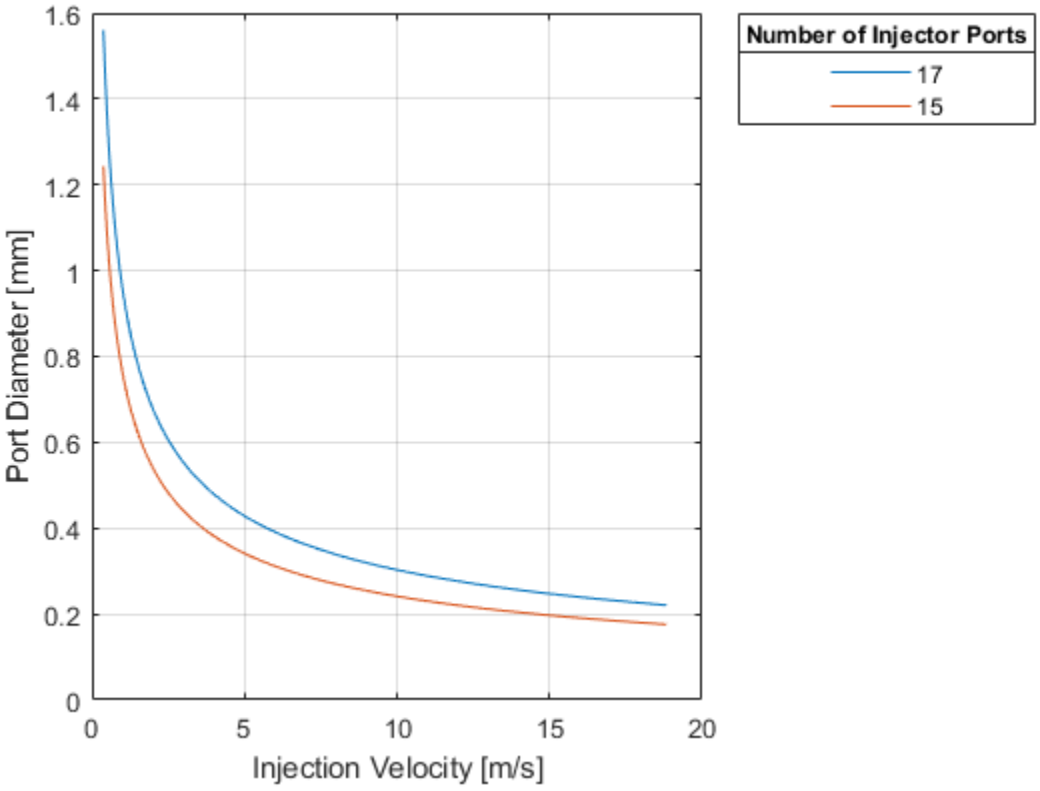

Figure 45: Film injection velocity vs port diameter

To stay within the bounds set forward by NASA SP-8087 a port diameter above 0.381 mm had to be chosen for each port size [39]. This resulted in the lowest set of injection ports having a diameter set to 0.4 mm and the other two sets of injection ports having a diameter of 0.5 mm to best match the injection velocity of the lower film cooling injection ports. With the injection port diameter defined the model was moved to a 3D modeling program to create a usable standard triangle language (STL) file for printing.

9.2 Solidworks Pressure Analysis

Before passing the completed model to ANSYS for a full structural analysis a preliminary test was performed on a simplified model of the combustion chamber to ensure that the model was ready. The simplified model, shown in Figure 46, removed the cooling lines and plenums as the required resolution was beyond what Solidworks could handle relative to building a mesh. Note that the removal of the coolant lines will have an effect on the relative strength as the inside of the chamber wall.

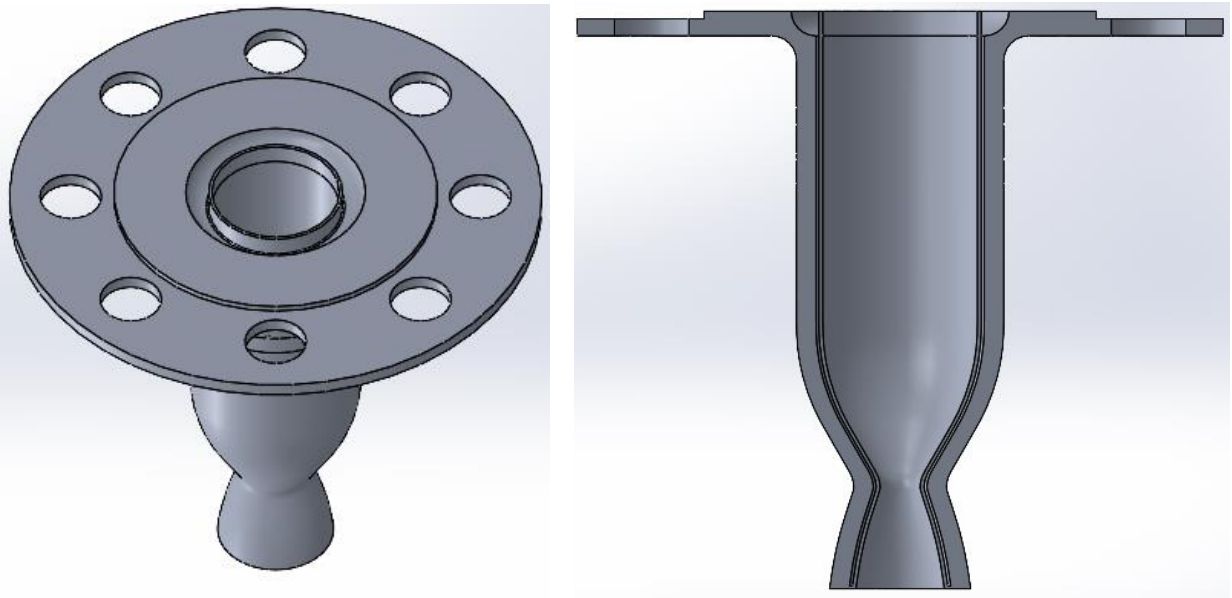

Figure 46: Simplified engine model and cutaway

A pressure load of 730 psi was applied along both sides of the cooling jacket, along with the upper plenum and the small edge wall at the bottom of the chamber. A pressure of 14.7 psi was applied along the inside of the chamber wall to simulate the engine shutting down, as this would be the time with the largest difference in pressure between the two sides of the cooling wall at high temperature. With regards to the fixturing, the engine was held fixed along the thru holes of the flange and the sealing face of the flange while a sliding fixture was applied long the portion of the

chamber inner wall that will be held in place by the injector manifold while assembled. The applied loads are shown in Figure 47.

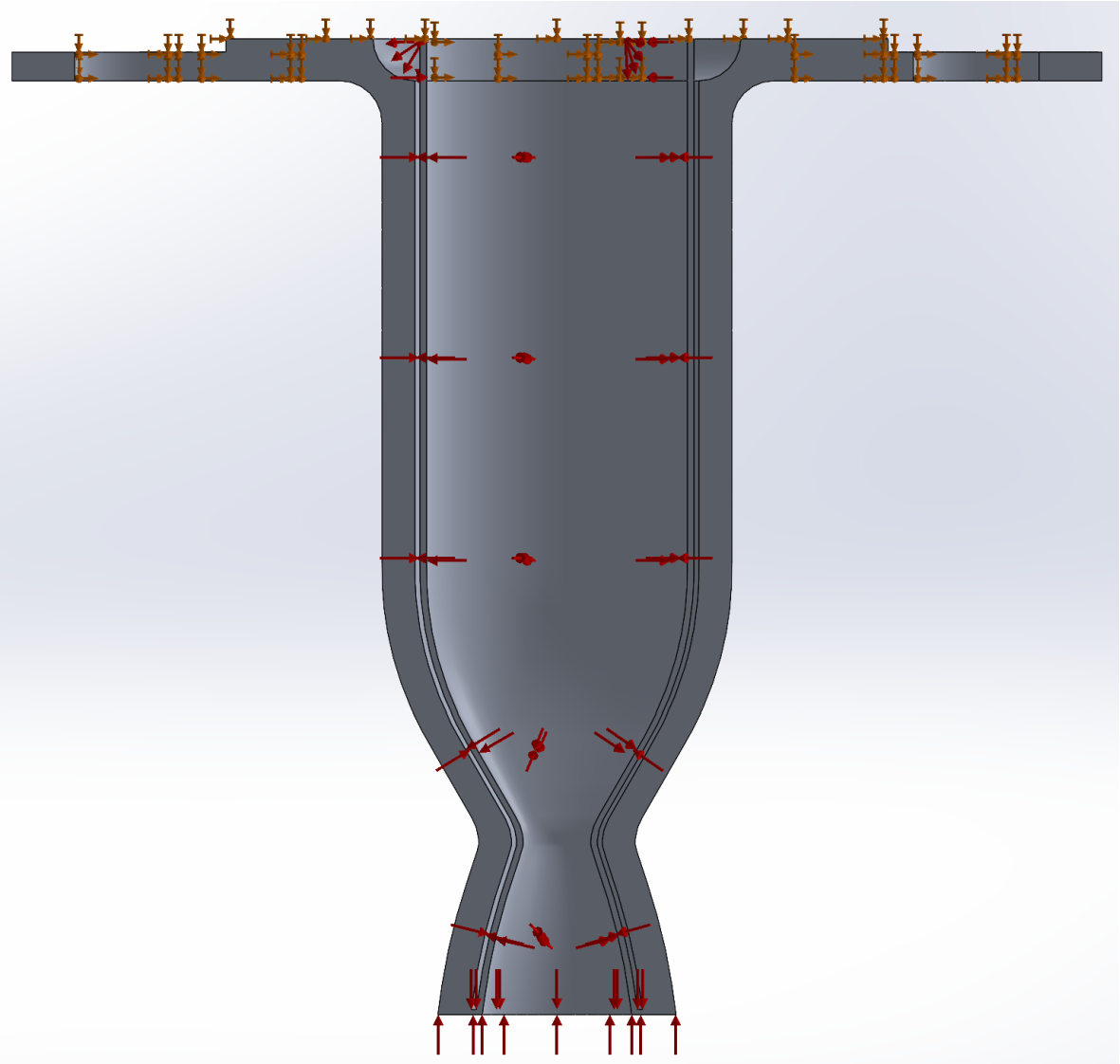

Figure 47: Applied loads in solidworks structural simulation

The output of this analysis is shown in Figure 48. Unfortunately, Solidworks will not allow a cutaway of the simulation to be shown so the full body simulation is shown in Figure 48. The largest estimated stress came out to 104.4 MPa which was located towards the top of the internal section of the combustion chamber which can be seen in Figure 48 in the center of the model.

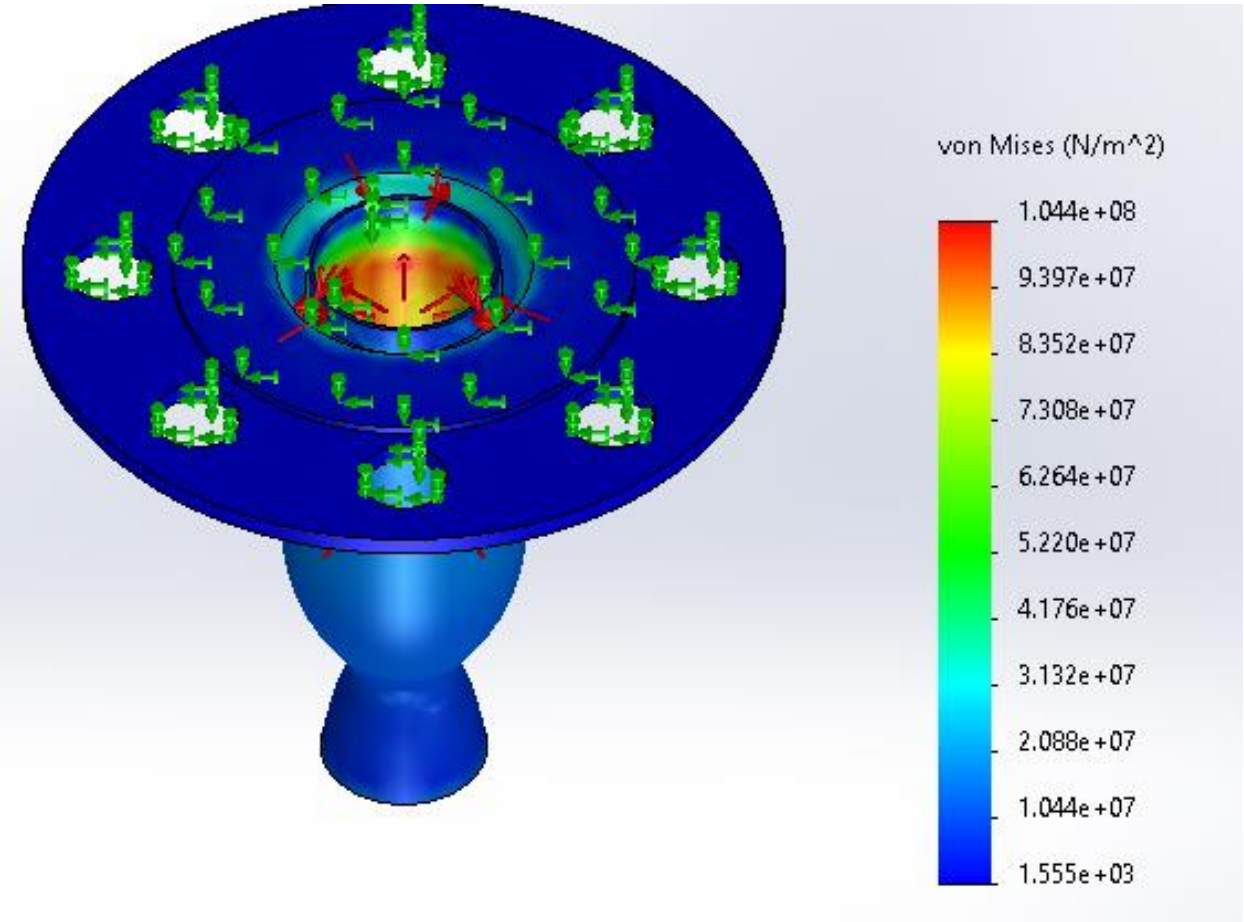

Figure 48: Solidworks preliminary structural analysis output

When analyzing the heated chamber for structural integrity the local axial temperature was found in Figure 40 to be 420 K or 150 °C. Note that there is a higher peak temperature of the system in the diverging section of the nozzle but the maximum expected stress in that area is much lower than peak expected stress due to the decrease in cross sectional area. Using the graph shown in Figure 49 the ultimate strength of $AlSi_{10}Mg$ at 150 °C is about 260 MPa and the yield strength appears to occur at 200 MPa. This leads to the estimated factor of safety of the engine to be 1.92. This would be the lowest factor of safety for the engine which suggests that it is a sufficient enough base model to be passed to ANSYS for finalized analysis.

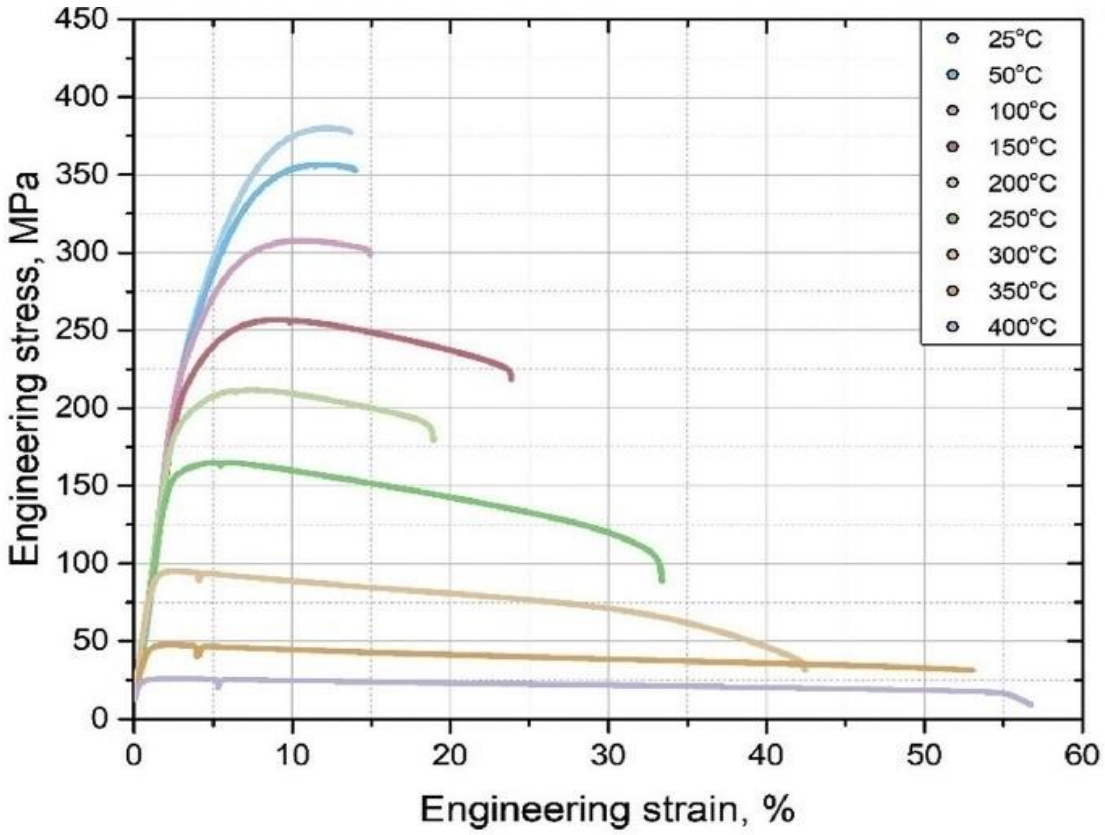

Figure 49: Stress strain curve of $AlSi_{10}Mg$ by temperature [40]

9.3 ANSYS Modeling

After the Solidworks model verified that the simplified model passed a preliminary pressure test the full chamber model was moved to ANSYS for a more thorough analysis. A pressure load of 730 psi was applied along all fuel facing surfaces including all plenums and film injection ports which were too small to test in Solidworks. In this scenario the internal face of the combustion chamber was again held at 14.7 psi to mimic the post fire low chamber pressure and high wall temperature scenario. Note that in reality the chamber pressure will likely be higher than the 14.7 psi ambient pressure due to the continued flow of coolant fuel after termination of the N_2O injection. The model with applied pressures is shown in Figure 50.

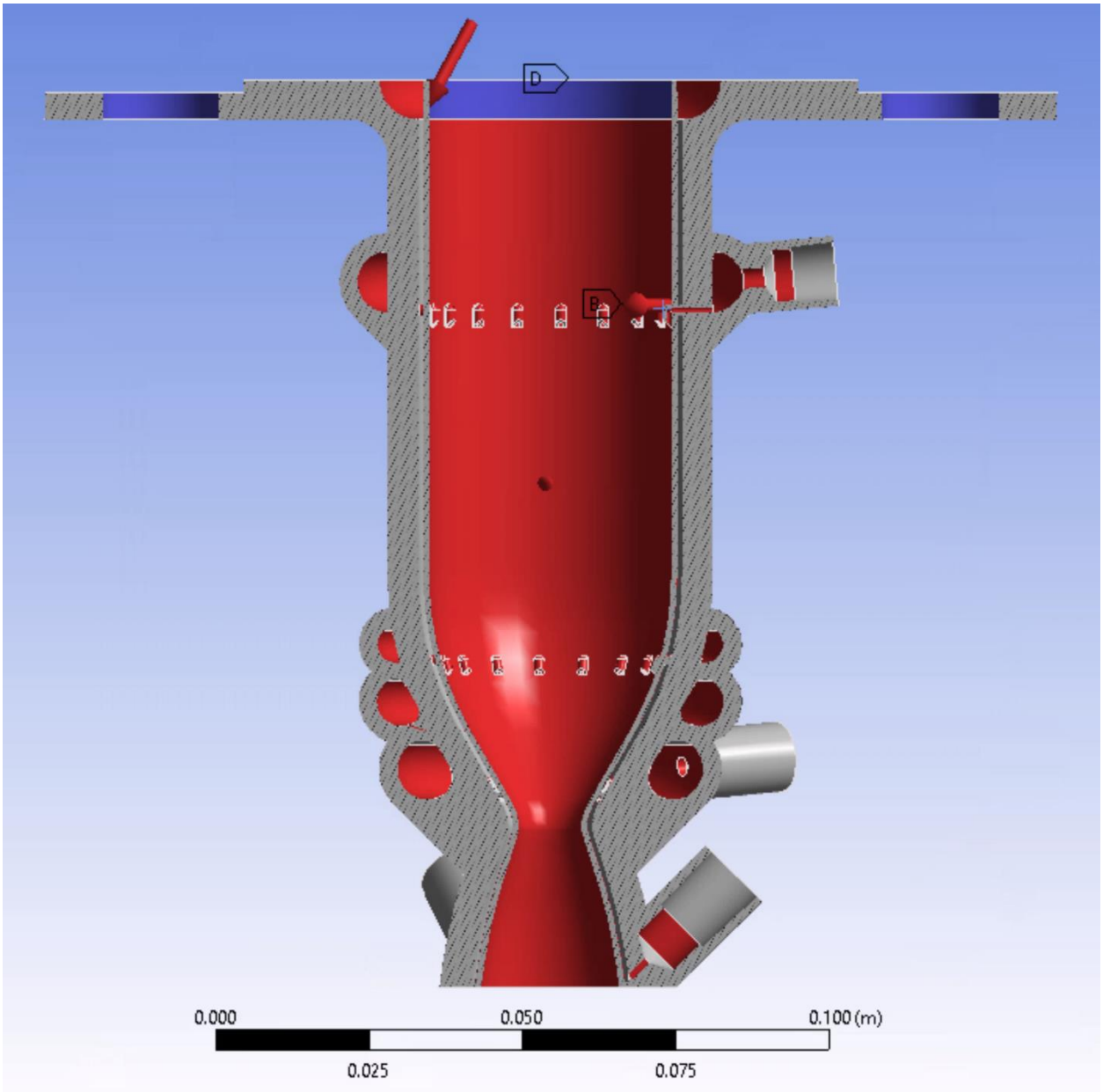

Figure 50:ANSYS structural simulation input cutaway

The resultant model with overexaggerated deformation is shown with structural stress in Figure 51.

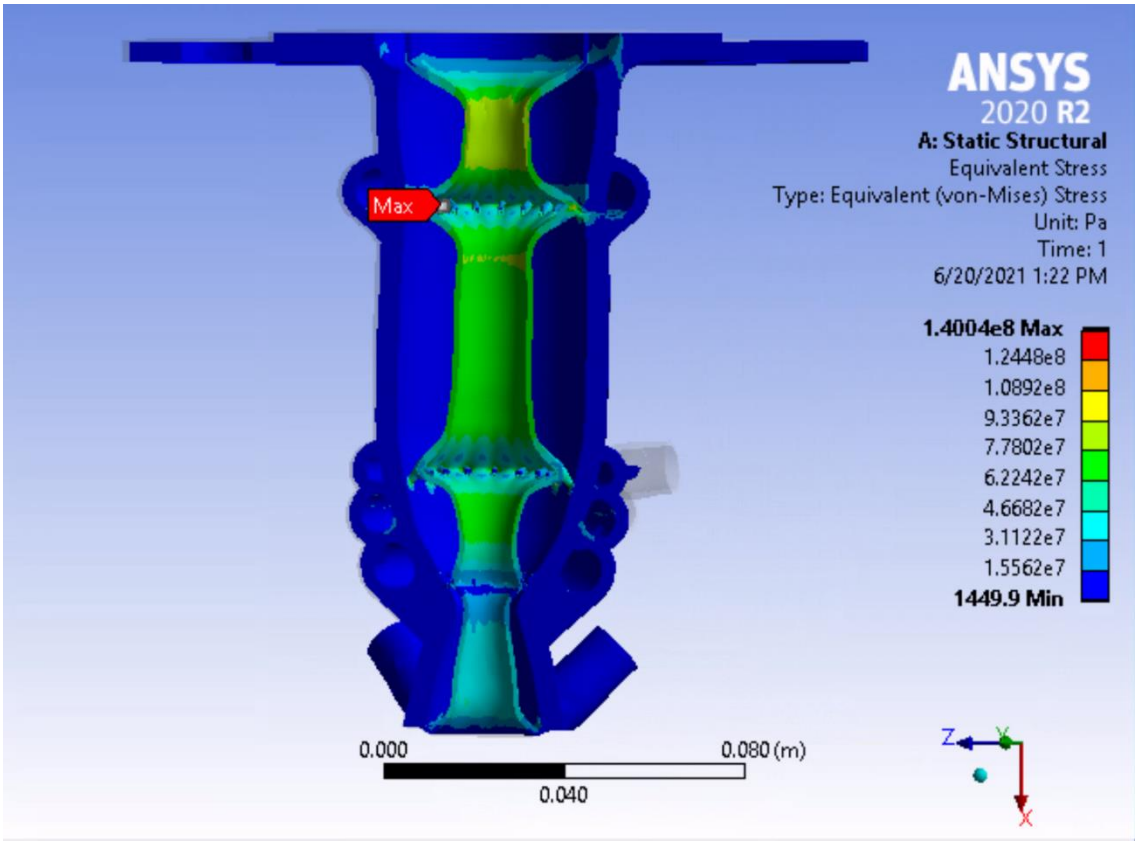

Figure 51: ANSYS structural simulation output cutaway

As expected, the film injection ports acted as a supporting ring along the chamber wall and locally decreased the stress in the wall. Separating the chamber wall into four sections between; the injector plate and the first set of on wall film coolant ports, the first and second set of film coolant ports, the second set of coolant ports and the wall separating the dump and regenerative cooling lines and the separating wall and the end of the nozzle. These sections yield average wall stresses of 82 MPa, 76 MPa, 65 MPa and 40 MPa respectively. The temperature and stress estimations coupled with the yield stresses shown in Figure 49 suggest that the system will not have a factor of safety lower than 2 at any location.

The high stress point, marked as “Max” in Figure 52, still falls within maximum stress bounds as the temperature of this section of the model is estimated to be 420 K by RPA.

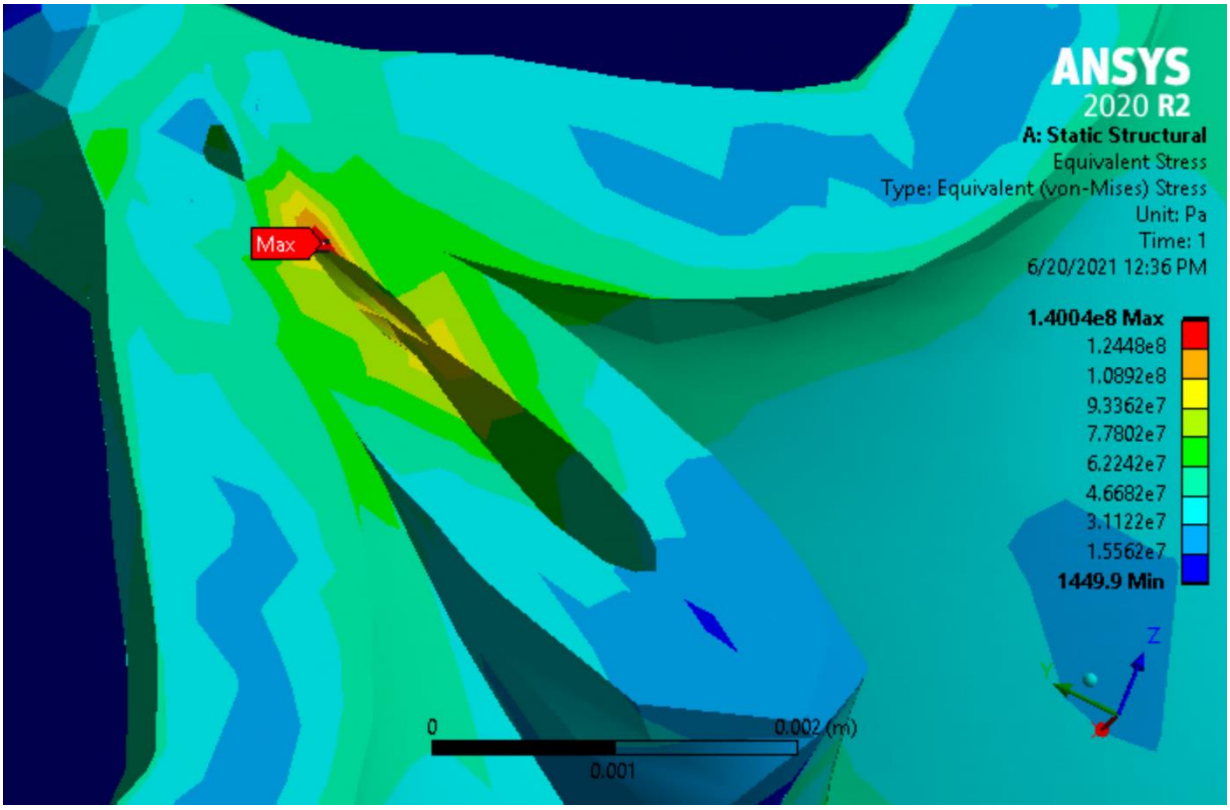

Figure 52: Maximum stress cutaway

Unfortunately, RPA does not take the small protrusions from the film injection sites into account when determining chamber surface temperature. In the event that film injection sites are determined to be a hot spot during testing, the film injection ports would have to be redesigned to have a lower profile inside of the combustion chamber. This maximum value is presenting inside of the film injection port which suggests that the local temperature along this inside face will be closer to the coolant temperature than that of the combustion boundary layer. As the film injection sites are a very small feature, this may be an artifact of the simulation and may not be representative of the real-life model. A short duration physical test would aid in determining if this local high stress point is actually a cause for concern.

9.4 Structural Considerations

A few other considerations that were not modeled should be taken into account, if possible, in future projects. The constant cycling of the engine will lead to engine fatigue over time and should be included when lifetime estimates of the engine are being created. Additionally, avoiding any cusps in the film injection routing should reduce stress concentrations

9.5 Cost

After the design work was completed, the last step was to estimate the cost of assembling and running the system for ground testing. This is broken into 4 main segments; cost of printing, post processing, manufacturing the remaining engine parts and plumbing/pressure vessels. This cost model will assume that the computers in a given lab can be equipped to interface through a system like LabView and will not be included.

The cost of printing the main combustion chamber was quoted using the AMPowerReport cost tool. This tool estimates the cost of an aluminum print of this volume with supports is between 2170 dollars and 2996 dollars. This cost range is determined by the specifications of the powder bed fusion machine that is used for manufacturing as the engine requires a high degree of precision which drives a higher price. The quoted price is likely to decrease in the next few years as additive manufacturing technology becomes more widespread and competition drives price down. Note that, NIST estimates that the cost of post processing an additively manufactured part accounts for about 8.4% of the total cost while the cost of printing the part attributes 80.9% of the total cost of an additively manufactured part [41]. The other 10.7% is attributed to the cost of assembly which will be ignored as assembly would be done by the university. This makes the assumed cost of post processing between 225 and 311 dollars.

The cost of the stock stainless steel to manufacture the injector plate assembly is 266 dollars for the flange section of the assembly and another 111 dollars for the stock of the internal injector components bringing the stock cost to 377 dollars. The injector costs would then increase dependent upon a university's choice of whether to manufacture the injector assembly in house or have it manufactured by a third party. The cost of getting those parts manufactured is estimated at 1,300 with a quote from the Protolabs automated quote system. Using the slowest delivery time reduced the cost of manufacturing by nearly 50%. Additionally, O-rings and RTV are fairly inexpensive therefore budgeting 50 dollars should be sufficient in budgeting.

The sizing of the nitrogen, nitrous oxide and fuel tank sizes will vary depending on how long a university chooses to run experiments but allocating 1,500 dollars should be enough to purchase fuel, nitrous oxide, and nitrogen tanks alongside a dump tank for any ethanol that is run though the dump cooling system. On top of this this cost is the plumbing and valves required to make the system run. The cost estimations and number of plumbing items are outlined in Table 13, where all values were obtained from Swagelok.com unless otherwise marked. The plumbing cost came to a total of 8,895 dollars. Note that these are cost estimates as specific plumbing parts will have costs vary with time.

Table 13: Plumbing Components Cost List

Part Name	Number of Parts	Unit Cost	Total Part Cost
Pneumatic Valve (low pressure)	5	300	1500
Pneumatic Valve (high pressure for Nitrogen feed line)	1	2000	2000
Regulator	5	500	2500
Check Valve	3	50	150
Vent Valve (NOS PowerShot purge valve)	1	175	1750
Hand Actuated Globe Valve	2	120	240
Pressure Relief Valve	4	200	800
Burst Disk	2	170	340
Pressure Sensor (Mouser 1000 psi pressure sensor)	10	65	650
Temperature Sensor (Jegs)	5	20	100
Filter	4	110	440

The summation of the above costs results in a total system setup cost of around 13,795 dollars when parts are manufactured in house and 15,095 dollars when manufacturing is passed to a third party. These estimated costs should fall within a reasonable budget for a university to put towards expanding their ground testing capabilities.

10 Conclusion

A step-by-step liquid engine design process that is capable of estimating the characteristic length of an engine using a showerhead injector was laid out in this thesis. The application of this design process is shown via the creation of the Hephaestus engine. Through the use of the nitrous oxide and an ethanol water mixture, the issues related to chemical storage were mitigated.

After setting design constraints and performing simple engine sizing calculations, most of the liquid engine design process centered around the estimation of characteristic length, which when found moves the remainder of the design process to supplementary software packages. The characteristic length estimation required breaking residence time into four parts, being droplet formation, droplet heating, droplet evaporation and combustion.

The solving of residence time required that, when any change was made to the combustion environment by introducing more fuel by way of film cooling or modification of the injector plate, the solution would be resolved. After several iterations of the residence time solution loop, the design point for characteristic length and injector geometry are able to be selected for a given design. The design process is laid out in section 5 to give clarity to the residence time loop and its relationship to the rest of the design process.

An example of the design process was shown via the development of the Hephaestus engine which had special design constraints as additive manufacturing was the planned manufacturing method. The model of Hephaestus was generated using the characteristic length, found using the design process from section 6, as an input to RPA which also performed heat transfer analysis. Once the RPA model held a sufficiently low heat a 3D model was created and put through stress testing to verify that it would be able to maintain structural integrity during an engine test.

10.1 Next Steps

This design, while fully functional in theory, could still use refinement before distribution to universities for lab use. This refinement is detailed in the theory and experimental sections.

10.1.1 Theory

The characteristic length determination segment of the engine design process is a realistic simplified model of residence time. To make the model more complex the assumption that the

injection into quiescent gas could be also modeled as an injection into a turbulent slow-moving gas. Unfortunately, at the time of writing, there is not a large pool of resources to generate an exact solution for injection into a combusting gas.

Alongside this is the assumption that the injected fluid created perfect spheres upon breakup needs to be reinvestigated as well. This, while not explicitly documented, could be investigated by creating a normal distribution of a spray pattern to express the non-uniformity of droplet formation as this will likely impact the final characteristic length and yield a range of possible characteristic length values. This would suggest a characteristic length would have an efficiency, expressing the ratio of injected fluid would completely combust before exiting the combustion chamber. This would be expected to decrease the characteristic length overall as the model laid out within this thesis makes assumptions that overestimate droplet formation time and diameter.

The final piece of theory that could be expanded upon is the introduction of heating to the system to begin at the injection of a fluid instead of once said fluid has become a droplet. This will result in a decrease in the heat up time of the injected fluid once a droplet had formed, as the fluid will already be at a higher bulk temperature.

10.1.2 Experimental

Hephaestus as currently designed is nearly ready for physical testing. While all components of the engine body and injection system are designed, the supporting plumbing, shown in the plumbing diagram in section 12.7, still need to be chosen and purchased. The entirety of Hephaestus was designed using only theory and many variables are typically determined using laboratory testing experimental verification of said values may prove to be useful. While the characteristic length and placement of the film coolant ports should be close to a function design, further design iterations may be needed if hotspots occur in the engine wall. Characteristic length should be

increased or decreased relative to the efficiency witnessed during testing. The underestimation of characteristic length is a much larger point of interest than the over estimation as an overestimation only results in a loss in efficiency while an underestimation will result in external combustion and possible damage to surrounding lab equipment. The spacing of film cooling ports can be tested by running short duration test fires with the time increasing between tests. After each test fire the system should be disassembled and searched for hot spots localized along the engine surface. When this occurs the space between the coolant ports should decrease and the number of ports should increase accordingly.

11 References

[1] ThermoFisher Scientific, "Safety Data Sheet Hydrazine and Hydrazine Hydrate," 11 July 2019. [Online]. Available: https://www.fishersci.com/store/msds?partNumber=AC296810050&productDescription=HYDRAZINE+HYDRATE+SOL+55%25+5ML&vendorId=VN00032119&countryCode=US&language=en. [Accessed 26 08 2021].

[2] S. H. Youngblood, "Dsign and Testing of a Liquid Nitrous Oxide and Ethanol Fueled Rocekt Engine," New Mexico Institue of Mining and Technology, Socorro, 2015.

[3] ESA, "3D-Printed Showerhead Injector," European Space Agency, 2014.

[4] G. P. Sutton and O. Biblarz, Rocket Propulsion Elements, Hoboken: John Wiley and Sons Inc., 2017.

[5] D. K. Huzel and D. H. Huang, Modern Engineering for Design of Liquid-Propellant Rocket Engines, Washington DC: American Institute of Aeronautics and Astonautics, 1992.

[6] M. L. Meyer and D. L. Linne, "Forced Convection Boiling and Critical Heat Flux of Ethanol in Electrically Heated Tube Tests," in *Aerospace Sciences Meeting & Exhibit*, Reno, Nevada, 1998.

[7] L. E. Bollinger, M. Goldsmith and A. W. Lemmon Jr., Liquid Rockets and Propellants, New York: Academic Press, 1960.

[8] R. W. Humble, G. N. Henry and W. J. Larson, Space Propulsion Analysis and Design, New York: McGraw-Hill, 1995.

[9] N. H. Naraghi, S. Dunn and D. Coats, "Dual Regenerative Cooling Circuits for Liquid Rocket Engines," Air Force Research Lab, Carson City, 2006.

[10] P. R. Grandl, S. E. Greene and T. Wammen, "Bimetallic Channell Wall Nozzle Development and Hot-fire Testing using Additively Mannufactured Laser Wire Direct Closeout Technology," in *AIAA/SAE/ASEE Joint Propulsion Conference*, Indianapolis, 2019.

[11] P. R. Gradl, C. Protz and T. Wammen, "Additive Manufcturing Development and Hot-fire Testing of Liquid Rocket Channel Wall Nozzles using Blown Powder Directed energy Deposition Inconel 625 and JBK-75 Alloys," in *AIAA/SAE/ASEE Joint Propulsion Conference*, Indianapolis, 2019.

[12] Q. Chen, G. Guillemot, C.-A. Gandin and M. Bellet, "Three-dimensional Finite Element Thermomechanical Modeling of Additive Manufacturing by Selective Laser Melting for Ceramic Materials," *Additive Manufacturing*, no. 16, pp. 124-137, 2017.

[13] P. Gradl, S. E. Greene, C. Protz, B. Bullard, J. Buzzell, C. Garcia, J. Wood, K. Cooper, J. Hulka and R. Osborne, "Additive Manufacturing of Liquid Rocket Engine Combustion Devices: A Summary of Process Developm,ents and Hot-Fire Testing Results," in *AIAA/SAE/ASEE Joint Propulsion Conference*, Cincinnati, 2018.

[14] Launcher, "LauncherSpace," Launcher, [Online]. Available: https://launcherspace.com/engine-2.

[15] Relativity, "RelativitySpace," Relativity, [Online]. Available: https://www.relativityspace.com/rockets. [Accessed 2020].

[16] Ursa Major Technologies, "UrsaMajorTechnologies," UrsaMajorTechnologies, [Online]. Available: https://www.ursamajortechnologies.com/engines. [Accessed 2021].

[17] N. N. Kumbhar and A. V. Mulay, "Post Processing Methods used to Improve Surface Finish of Products which are Menufactured by Additive Manufacturing Technologies: A Review," *Article of Professional Intrest*, 30 August 2016.

[18] P. R. Gradl, C. S. Protz, K. Cooper, D. Ellis, L. J. Evans and C. Garcia, "GRCop-42 Development and Hot-fire Testing Using Additive Manufacturing Powder Bed Fusion for Channel-cooled Combustion Chambers," in *AIAA Propulsion and Energy 2019 Forum*, Indianapolis, 2019.

[19] Renishaw, "Data Sheets Additive Manufacturing," 07 2015. [Online]. Available: https://www.renishaw.com/en/data-sheets-additive-manufacturing--17862. [Accessed 14 07 2021].

[20] NASA, "Chemical Equilibrium Applications software," NASA, Cleveland, 1996.

[21] C. F. Beaton and G. F. Hewitt, Physical Property Data for the Chemical and Mechanical Engineer, New York: Hemisphere Publishing Company, 1989.

[22] S. Tang, T. Liu, S. Duan, J. Guo and A. Tang, "Comparison of Growth Characteristics and Properties of CVD TiN and TiO2 Anti-Coking Coatings," *Processes*, vol. 7, no. 9, 2019.

[23] A. H. Lefebvre and V. G. McDonell, Atomization and Sprays, Boca Raton: CRC Press Taylor & Francis Group, 2017.

[24] COMSOL, "Do.Comsol.Com," [Online]. Available: https://doc.comsol.com/5.5/doc/com.comsol.help.cfd/cfd_ug_fluidflow_high_mach.08.27.html#1508110. [Accessed 14 07 2021].

[25] Dortmund Data Bank, "Surface Tension of Ethanol," [Online]. Available: http://www.ddbst.com/en/EED/PCP/SFT_C11.php. [Accessed 14 07 2021].

[26] J. A. Dean, Lange's Handbook of Chemistry, New York: McGraw-Hill, 1999.

[27] National Institute of Standards and Technology, "Water," 2011. [Online]. Available: https://webbook.nist.gov/cgi/cbook.cgi?ID=C7732185&Mask=4. [Accessed 14 07 2021].

[28] LibreTexts Chemistry, "Dalton's Law (Law of Partial Pressures)," LibreTexts, 15 August 2020. [Online]. Available: https://chem.libretexts.org/Bookshelves/Physical_and_Theoretical_Chemistry_Textbook_Maps/Supplemental_Modules_(Physical_and_Theoretical_Chemistry)/Physical_Properties_of_Matter/States_of_Matter/Properties_of_Gases/Gas_Laws/Dalton's_Law_(Law_of_Partial_Pre. [Accessed 27 August 2021].

[29] J. L. Monteith and M. H. Unsworth, Principles of Environmental Physics, Academic Press, 2007.

[30] Engineering Toolbox, "Air - Thermal Conductivity," The Engineering Toolbox, [Online]. Available: https://www.engineeringtoolbox.com/air-properties-viscosity-conductivity-heat-capacity-d_1509.html. [Accessed 14 07 2021].

[31] J. Clark, "Fractional Distillation of Non-ideal Mixture (Azeotropes)," LibreTexts, 15 Augut 2020. [Online]. Available: https://chem.libretexts.org/Bookshelves/Physical_and_Theoretical_Chemistry_Textbook_Maps/Supplemental_Modules_(Physical_and_Theoretical_Chemistry)/Equilibria/Physical_Equilibria/Fractional_Distillation_of_Non-ideal_Mixtures_(Azeotropes). [Accessed 15 August 2021].

[32] K. K. Kuo, Principles of Combustion, Hoboken: John Wiley and Sons Inc., 2005.

[33] C. P. S. T. Christopher Larkin, Interviewee, *Conversation on drill bit engagment.* [Interview]. May 2021.

[34] Parker, Parker O-Ring Handbook, Cleveland: Parker Hannifin Corperation, 2021.

[35] American Society of Mechanical Engineers, "B16.5-2003 Pipe Flanges and Flanged Fittings," American Society of Mechanical Engineers International, New York, 2003.

[36] A. G. Vorobyev, S. S. Vorobyeva, L. Zhang and E. N. Beliaev, Thermal State Calculation of Chamber in Small Thrust Liquid Rocket Engine for Steady State Pulsed Mode, Moscow: Chinese Journal of Aeronautics, 2019.

[37] C. L. Bradford, Design and CFD Optimization of Methane Regenerative Cooled Rocket Nozzles, El Paso: Digital Commons, 2011.

[38] Electro Optical Systems, "EOS.info," 05 2021. [Online]. Available: https://www.eos.info/03_system-related-assets/material-related-contents/metal-materials-and-examples/metal-material-datasheet/aluminium/material_datasheet_eos_aluminium-alsi10mg_en_web.pdf. [Accessed 14 07 2021].

[39] NASA, "NASA-SP-8087 Liquid Rocket Engine Fluid-cooled Combustion Chambers," NASA, 1972.

[40] N. E. Uzan, R. Shneck and N. Farge, "High-Temperature Mechanical Properties of AlSi10Mg Specimens Fabricated by Additive Manufacturing using Selective Laser Melting Technologies (AM-SLM)," *Additive Manufacturing,* vol. 24, pp. 257-263, 2018.

[41] National Institute of Standards, "Costs and Cost Effectiveness of Additive Manufacturing," U.S. Department of Commerce, 2014.

[42] T. W. Khan and I. Qamar, "Factors Affecting Characteristics Length of the Combustion Chamber of Liquid Propellant Rocket Engines," *Research Journal of Engineering and Technology,* vol. 38, no. 3, pp. 729-744, 2019.

12 Appendix

The appendix below provides the code used throughout this thesis as well as images from 3D modeling software and the design process flowchart in its entirety.

12.1 Code

```
%Alec Bluhm
%L STAR solving
%7/28/2020
```

12.1.1 House keeping

```
clear;
close all;
clc;
```

12.1.2 Assumptions

```
%Droplets are spherical
%Ambient heat transfer to droplets through radiation is negligable when
% compared to forced convection
%Temperature in droplet is homogenous
```

12.1.3 Constants

```
A_throat=3.5401e-4;%[m2]
r_t=.01066;%[m]
T_inj=324.45;%[K]

Mix=0.7;

%[g/mol,kg/m3]
water=[18.015,997*1000];
Ethanol=[46.07,789*1000];

M_den_each=[water(2)/water(1),Ethanol(2)/Ethanol(1)];%[mol/m3]
M_vol=M_den_each(1)*(1-Mix)+M_den_each(2)*Mix;%[mol/m3]
F_thrust_USA=100;%[lbf]
F_thrust=F_thrust_USA*4.44822;%[N]
```

12.1.4 NASA CEA VALUES

```
Mw_comb_old=25.740;%[g/mol] molar density of combusted gas
T_cc_old=3055.76;%[K]combustion Temperature
k_old=1.1429;%ratio of specific heats of combusted gas
rho_t_old=2.15;%[kg/m3]
rho_gas_old=3.4925;%[kg/m3]
Cp_cc_old=3.9602*1000;%[J/kg*K]
mu_air_old=0.00007702;%[] https://curiosityfluids.com/2019/02/15/air-properties-calculator/
T=3000 [K];P=3447400 [Pa]

Mw_comb=22.304;%[g/mol] molar density of combusted gas
T_cc=2343.63;%[K]combustion Temperature
k=1.2309;%ratio of specific heats of combusted gas
OFratio=3.75 ;
OFratio_NASA CEA=2.1647; %This value is the real OF ratio but it includes film coolant
rho_t=2.456;%[kg/m3]
rho_gas=3.9460;%[kg/m3]
Cp_cc=2.0122*1000;%[J/kg*K]

mu_air=0.00006740;%[] https://curiosityfluids.com/2019/02/15/air-properties-calculator/ T=2343
[K];P=3447400 [Pa]
```

12.1.5 Constants

```
Pe=14.1;%[psi]
Pc=500;%[psi]

mdot_NASA CEA= Mdot_Thrust(F_thrust,Mw_comb,T_cc,Pe,Pc,k);%[kg/sec]
md_fuel_NASA CEA=mdot_NASA CEA/(1+OFratio_NASA CEA);
md_ox_NASA CEA=mdot_NASA CEA-md_fuel_NASA CEA;

mdot= Mdot_Thrust(F_thrust,Mw_comb_old,T_cc_old,Pe,Pc,k_old);%[kg/sec]
md_fuel=mdot/(1+OFratio);
md_ox=mdot-md_fuel;
[At,rt] = Throat_area(F_thrust,k,Mw_comb,Pe,Pc,T_cc,rho_t);
```

12.1.6 Atomization Analysis

```
mu_H2O=1.301e-4;%[Pa*s] ref: https://www.engineeringtoolbox.com/water-dynamic-kinematic-
viscosity-d_596.html
mu_eth=1.42e-5;%[Pa*s] ref: https://www.engineeringtoolbox.com/ethanol-dynamic-kinematic-
viscosity-temperature-pressure-d_2071.html
%NOTE 1[Pa*s] = 1[kg/(m*s)]
mu_fuel=mu_H2O*(1-Mix)+mu_eth*Mix;%[kg/m*s]
rho_H2O=997;%[kg/m3]
rho_eth=789;%[kg/m3] both assuming incompressed after hitting liquid stage
rho_fuel=rho_H2O*(1-Mix)+rho_eth*Mix;%[kg/m3]
Mw_eth=46.069;%[g/mol]
Mw_H2O=18.01528;%[g/mol]
```

```
Mw_fuel=Mw_eth*Mix+Mw_H2O*(1-Mix);
mu_guess=exp(exp((rho_fuel*((T_inj)/(Mix*Mw_eth+Mw_H2O*(1-Mix))))))/10;
% Isp= 2369.3;%[m/sec]already multiplied by g0 in NASA CEA output

% Port_diameter=linspace(.0465,.1065)*0.0254;%[m] injection port diameters
Injection_diameter=linspace(.002,.003);%[m] injection port diameters
N=[2,4,6,8,10];%number of injection ports

for j=1:length (N)
 for i=1:length (Injection_diameter)
  A(i,j)=pi*(Injection_diameter(i)/2)^2/N(j);%[m2]
  Port_diameter(i,j)=Injection_diameter(i)/sqrt(N(j));%[m]
  V_inj(i,j)=md_fuel/(rho_fuel*A(i,j));%
  Re_inj(i,j) = Reynold(rho_fuel,V_inj(i,j),Port_diameter(i,j),mu_fuel);
 end
end
Port_diameter_plot=Port_diameter*1000;%[mm]
fig1=figure();
semilogy(Port_diameter,Re_inj,'o-')
ylabel('Reynolds number')
xlabel('Injection Port diameter [m]')
lgd=legend('2','4','6','8','10','Location','northeastoutside');
lgd.Title.String = ('Injector ports');
grid on
title('Injection Reynold''s number')
movegui(fig1,'center')
disp(['Reynolds numebr graph suggests all injection port diameters are going to be turbulent,
therefore ',...
 'jet breakup analysis should be performed with turbulent assumptions for internal
instability.'])
fig2=figure();
plot(Port_diameter,V_inj,'o-')
ylabel('Injection Velocity [m/s]')
xlabel('Injection port diameter [m]')
lgd=legend('2','4','6','8','10','Location','northeastoutside');
lgd.Title.String = ('Injector ports');
title('Injector Port Diameter vs Velocity')
grid on
movegui(fig2,'center')
% Surface Tension Estimations
Eth_ST_table=load('EthanolSurfaceTension.txt');%SOURCE:
http://ddbonline.ddbst.de/DIPPR106SFTCalculation/DIPPR106SFTCalculationCGI.exe
Eth_ST_table_temp=Eth_ST_table(:,1);%[K]
% Eth_ST_table_sigma=Eth_ST_table(:,2);%[mN/m]
Eth_ST_table_sigma=Eth_ST_table(:,2)/1000;%[N/m]
[Loc] = Search(Eth_ST_table_temp,T_inj);
if Eth_ST_table_temp(Loc<T_inj)
 spacing_set=(T_inj-Eth_ST_table_temp(Loc))/(Eth_ST_table_temp(Loc+1)-Eth_ST_table_temp(Loc));
 Sigma_ethanol=(Eth_ST_table_sigma(Loc+1)-
Eth_ST_table_sigma(Loc))*spacing_set+Eth_ST_table_sigma(Loc);%[mN/m]
else
 spacing_set=(T_inj-Eth_ST_table_temp(Loc-1))/(Eth_ST_table_temp(Loc)-Eth_ST_table_temp(Loc-1));
 Sigma_ethanol=(Eth_ST_table_sigma(Loc)-Eth_ST_table_sigma(Loc-
1))*spacing_set+Eth_ST_table_sigma(Loc-1);%[mN/m]
```

```
end

Water_ST_table=load('WaterSurfaceTension.txt');%SOURCE:
http://ddbonline.ddbst.de/DIPPR106SFTCalculation/DIPPR106SFTCalculationCGI.exe
Water_ST_table_temp=Water_ST_table(:,1);%[K]
% Water_ST_table_sigma=Water_ST_table(:,2);%[mN/m]
Water_ST_table_sigma=Water_ST_table(:,2)/1000;%[N/m]
[Loc] = Search(Water_ST_table_temp,T_inj);
if Water_ST_table_temp(Loc<T_inj)
 spacing_set=(T_inj-Water_ST_table_temp(Loc))/(Water_ST_table_temp(Loc+1)-
Water_ST_table_temp(Loc));
 Sigma_Water=(Water_ST_table_sigma(Loc+1)-
Water_ST_table_sigma(Loc))*spacing_set+Water_ST_table_sigma(Loc);%[N/m]
else
 spacing_set=(T_inj-Water_ST_table_temp(Loc-1))/(Water_ST_table_temp(Loc)-
Water_ST_table_temp(Loc-1));
 Sigma_Water=(Water_ST_table_sigma(Loc)-Water_ST_table_sigma(Loc-
1))*spacing_set+Water_ST_table_sigma(Loc-1);%[N/m]
end

Sigma_fuel=Sigma_ethanol*Mix+Sigma_Water*(1-Mix);%[N/m]

%Droplet diameter
Size_V_inj=size(V_inj);%size variable for loop
P_cc=34.474*100000;%[Pa];
R_gas=P_cc/(rho_gas*T_cc);
R_air=.287*1000;%[J/(kg*K)]
Scale_Factor=R_gas/R_air;
mu_gas=mu_air*Scale_Factor;

for i=1:Size_V_inj(1)
 for j=1:Size_V_inj(2)
  %mu=dynamic visc= [kg/m*s]
  %sigma= surface tension [kg/s2]
  %U=velocity [m/s]
  %rho=density [kg/m3]
  SMD(i,j)=300*Port_diameter(i,j)^.3*mu_fuel^.07*rho_fuel...
   ^-.648*Sigma_fuel^-.15*V_inj(i,j)^-.55*mu_gas^.78*rho_gas^-.052;%[m] AaS [134] EQ6.3
  MMD(i,j)=6*Port_diameter(i,j)*Re_inj(i,j)^-.15;
 end
end

figure
semilogy(A,SMD*1000,'o-')
xlabel('injection port area [m2]')
ylabel('Sauter Mean Diamter[mm]')
lgd=legend ('2','4','6','8','10','Location','northeastoutside');
lgd.Title.String = ('Injector ports');
grid on

figure
plot(A,SMD*1000,'o-')
xlabel('injection port area [m2]')
ylabel('Sauter Mean Diamter[mm]')
```

```
lgd=legend ('2','4','6','8','10','Location','northeastoutside');
lgd.Title.String = ('Injector ports');
grid on

figure
plot(Port_diameter_plot,MMD*1000,'o-')
xlabel('Injection port diamter [mm]')
ylabel('Median Mass Diamter[mm]')
lgd=legend ('2','4','6','8','10','Location','northeastoutside');
lgd.Title.String = ('Injector ports');
grid on
```

Reynolds numebr graph suggests all injection port diameters are going to be turbulent, therefore jet breakup analysis should be performed with turbulent assumptions for internal instability.

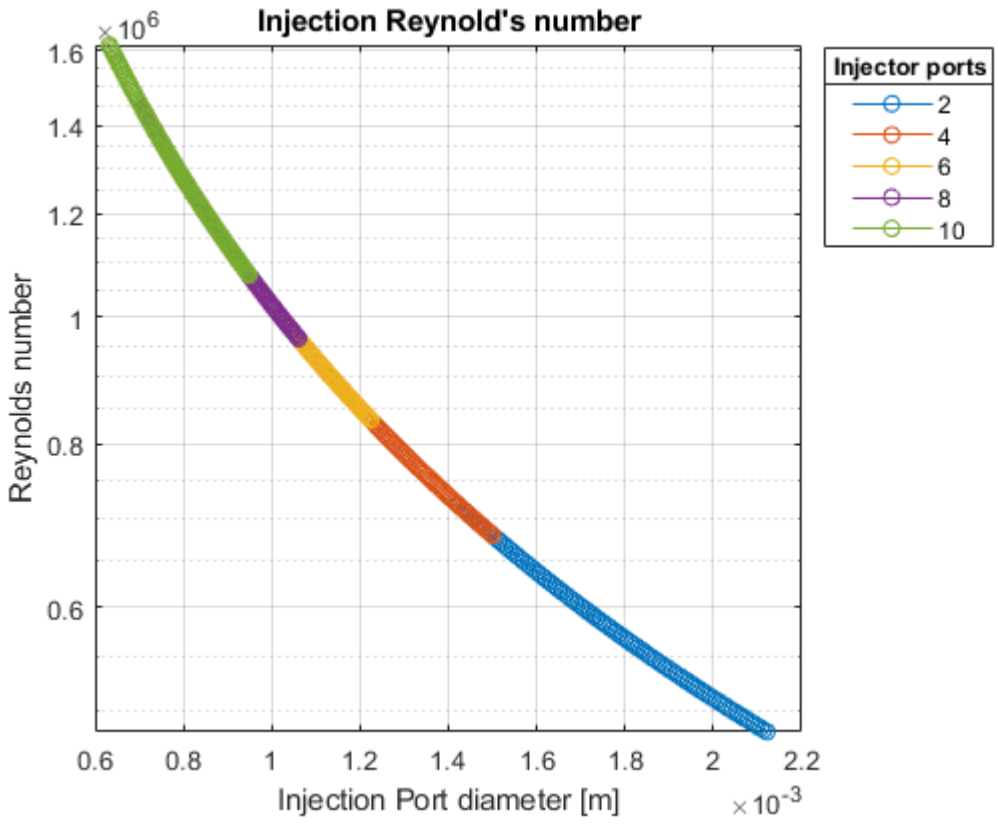

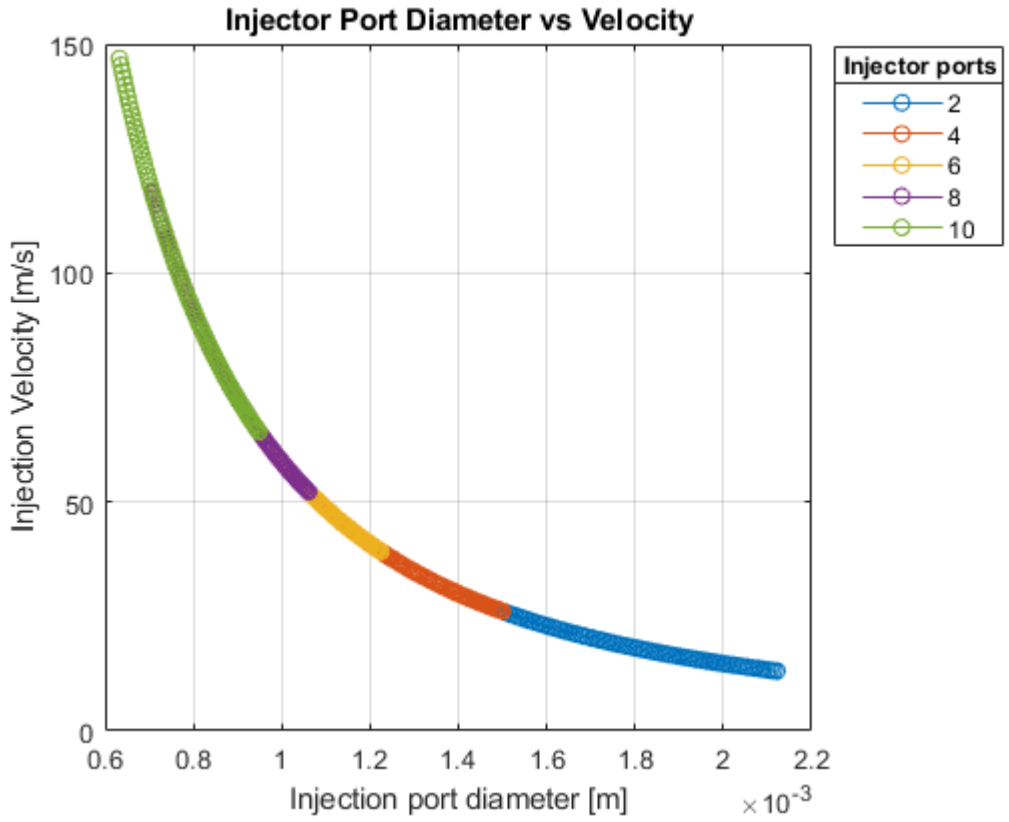
Injector Port Diameter vs Velocity
Injection Velocity [m/s]
150
100
50
0
0.6
0.8
1
1.2
1.4
1.6
1.8
2
2.2
Injection port diameter [m]
×10-3
Injector ports
2
4
6
8
10

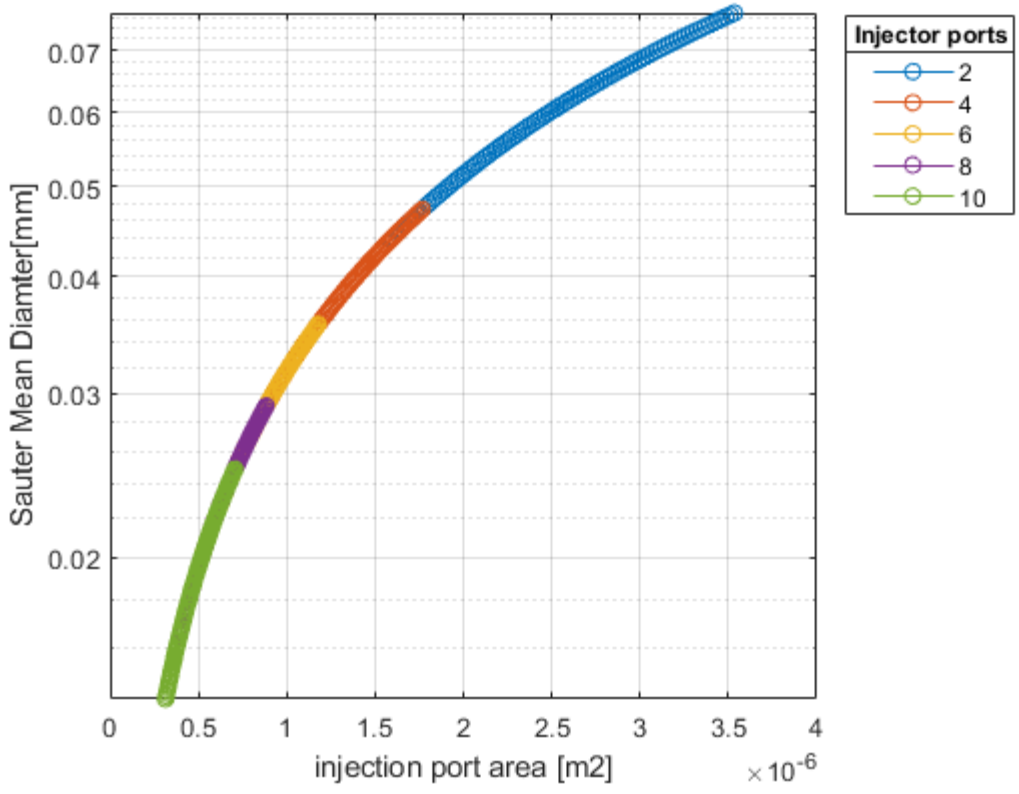
Sauter Mean Diamter[mm]
0.07
0.06
0.05
0.04
0.03
0.02
0
0.5
1
1.5
2
2.5
3
3.5
4
injection port area [m2]
×10-6
Injector ports
2
4
6
8
10

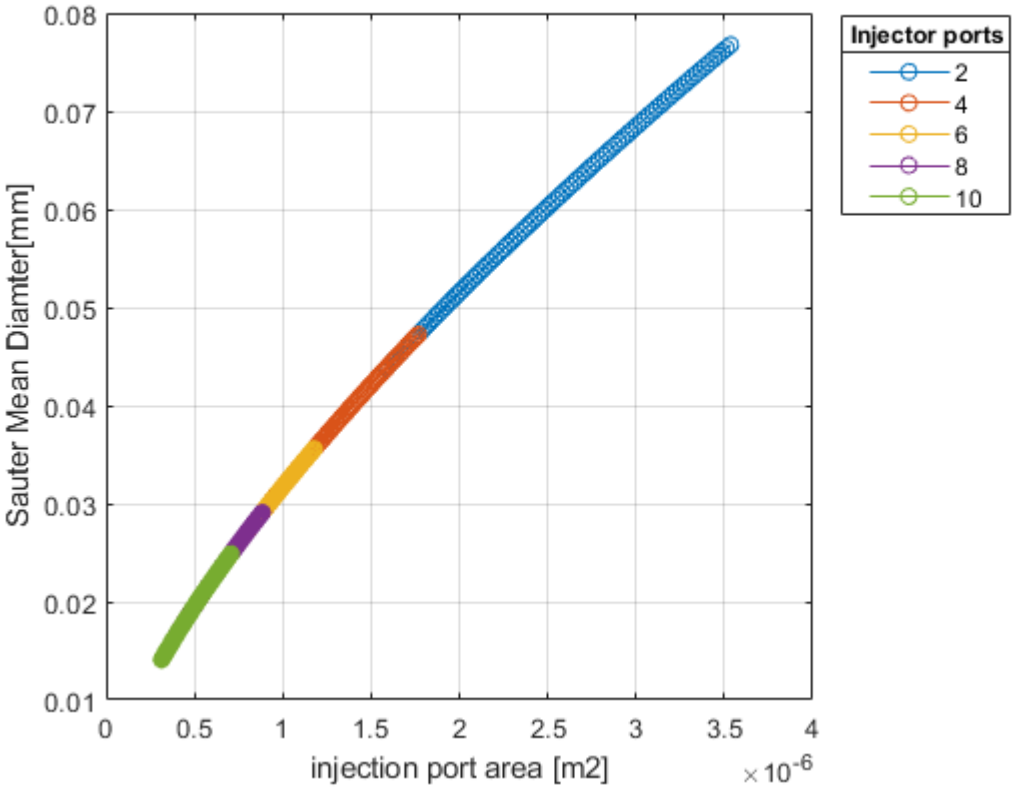
Injector ports
2
4
6
8
10
Sauter Mean Diamter[mm]
0.08
0.07
0.06
0.05
0.04
0.03
0.02
0.01
0
0.5
1
1.5
2
2.5
3
3.5
4
injection port area [m2]
×10-6

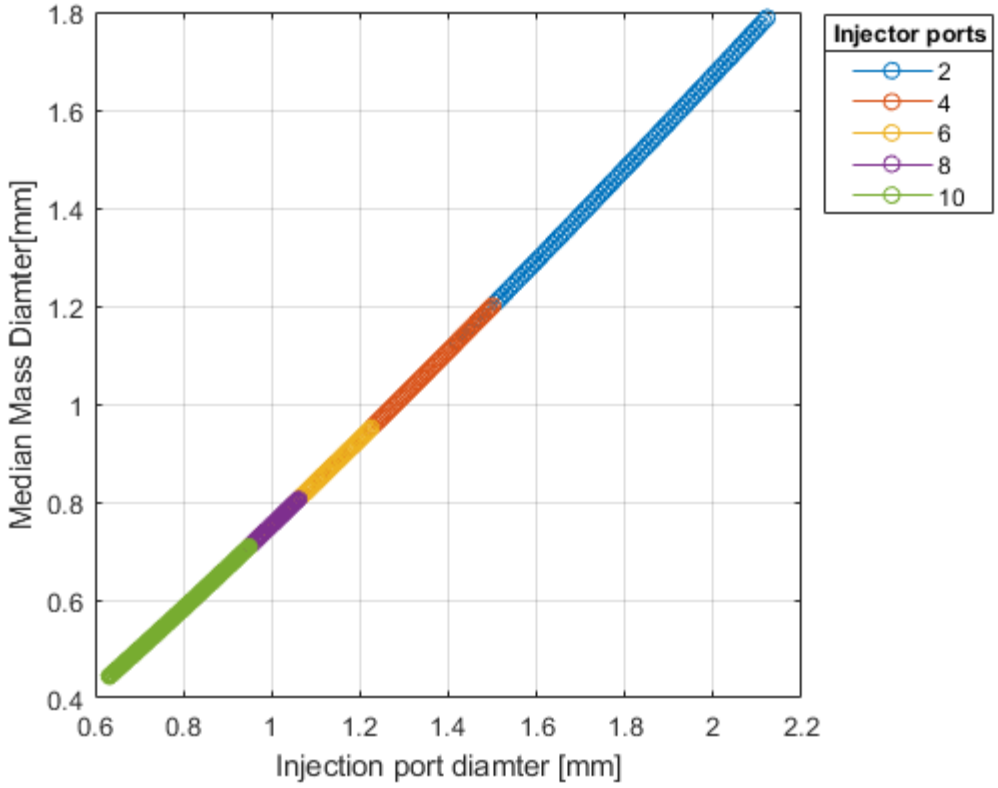
Injector ports
2
4
6
8
10
Median Mass Diamter[mm]
1.8
1.6
1.4
1.2
1
0.8
0.6
0.4
0.6
0.8
1
1.2
1.4
1.6
1.8
2
2.2
Injection port diamter [mm]

12.1.7 Jet Breakup Length

```
%Ambient pressure is inversly correlated with breakup length
for i=1:Size_V_inj(1)
 for j=1:Size_V_inj(2)
  We(i,j)=Weber(rho_fuel,V_inj(i,j),SMD(i,j),Sigma_fuel);
  Re(i,j)=Reynold(rho_fuel,V_inj(i,j),Port_diameter(i,j),mu_fuel);
  L(i,j)=538*Port_diameter(i,j)*We(i,j)^.5*Re(i,j)^(-5/8);%[m] Baron correlation of water breakup
data
  t_breakup(i,j)=L(i,j)/V_inj(i,j);%[s] time required for droplet formation to occur
  L(i,j)=L(i,j)*1000;%[mm] for plotting only
 end
end



figure
plot(Port_diameter_plot,L,'o-')
xlabel('Injection Port Diameter [mm]')
ylabel('Droplet breakup Distance[mm]')
lgd=legend('2','4','6','8','10','Location','northeastoutside');
lgd.Title.String = ('Injector ports');
title('Injection Port Diameter vs Droplet Breakup Distance')
grid on

figure
plot(Port_diameter_plot,t_breakup,'o-')
xlabel('Injection Port Diameter [mm]')
ylabel('Droplet breakup time [sec]')
lgd=legend('2','4','6','8','10','Location','northeastoutside');
lgd.Title.String = ('Injector ports');
title('Injection Port Diameter vs Droplet Breakup Time')
grid on
disp('Select droplet breakup location')
```

```
Select droplet breakup location
```

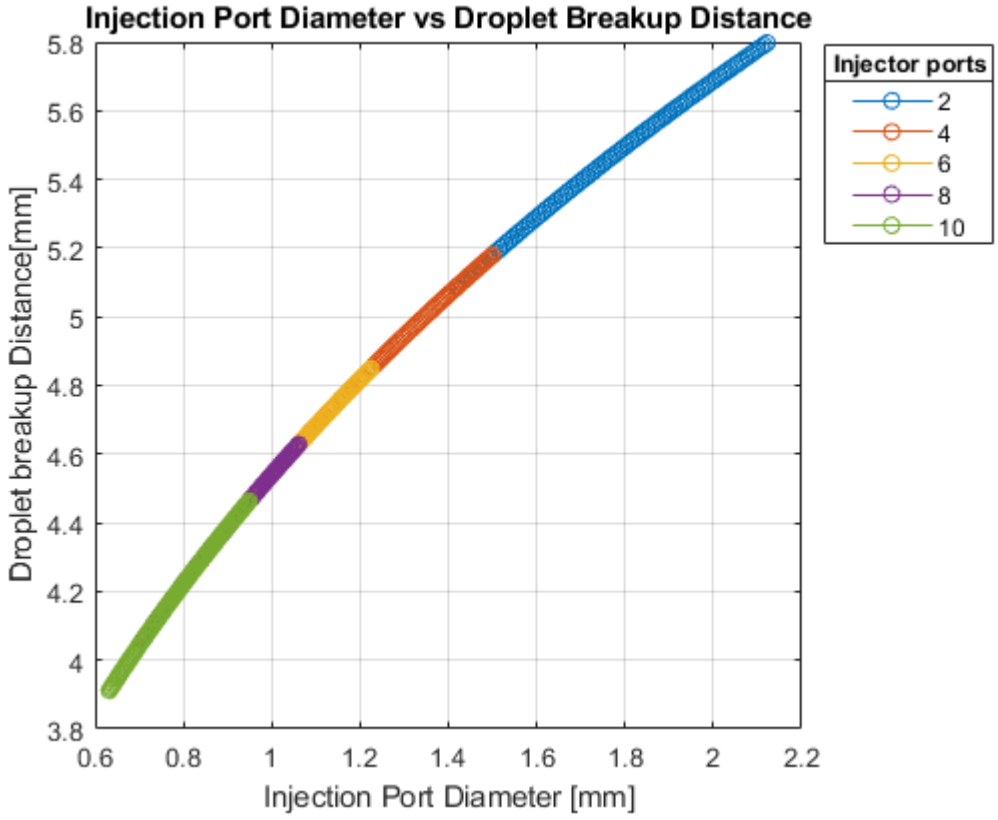
Injection Port Diameter vs Droplet Breakup Distance
Droplet breakup Distance[mm]
Injection Port Diameter [mm]
Injector ports
2
4
6
8
10
5.8
5.6
5.4
5.2
5
4.8
4.6
4.4
4.2
4
3.8
0.6
0.8
1
1.2
1.4
1.6
1.8
2
2.2

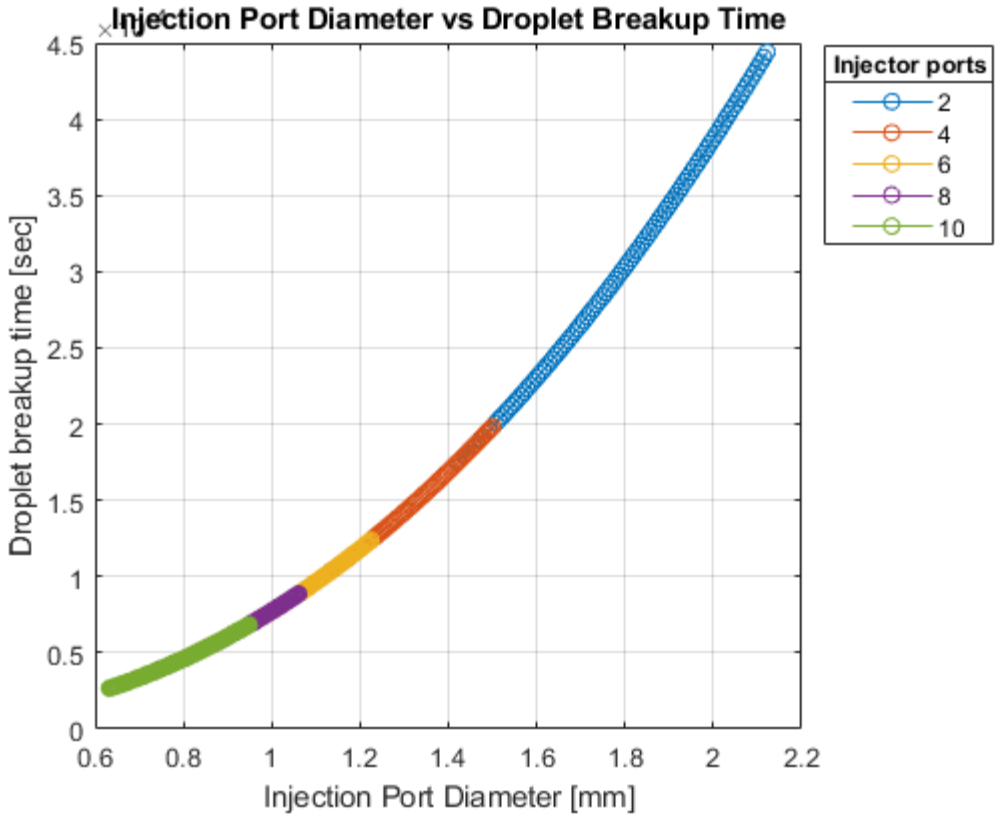
Injection Port Diameter vs Droplet Breakup Time
Droplet breakup time [sec]
Injection Port Diameter [mm]
Injector ports
2
4
6
8
10
4.5
4
3.5
3
2.5
2
1.5
1
0.5
0
0.6
0.8
1
1.2
1.4
1.6
1.8
2
2.2

12.1.8 Evaporation Analysis

```
[P_fs,P_fs_H2O,P_fs_eth]=Antoine(.7,500);
T_initial=[0,T_inj];
T=[T_inj,T_inj+.25];%[k] early estimate to get into while loop
Inj_port_Number=3;%corresponds with 6 ports

% D_droplet=SMD(Loc2,Inj_port_Number);%for now use the center value
T_droplet=T_inj;%[K]
```

12.1.9 Estimating convective heat transfer coefficient of the combusting gas

```
%vapor pressure calculations
A=4.92531;
B=1432.526;
C=-61.819;
P_Fs_ethanol=10^(A-(B/(T_droplet+C)));
P_Fs_ethanol=P_Fs_ethanol*10^5;%[Pa]
P_Fs_H2O=.61078*exp(17.27*(T_droplet-273.15)/(T_droplet-273.15+237.3));%[kPa]Vapor pressure
estimation by Tetens "Tetens, O. 1930. Über einige meteorologische Begriffe. Z. Geophys 6: 207-
309"
P_Fs_H2O=P_Fs_H2O*1000;%[pa]
P_Fs=P_Fs_ethanol*Mix+P_Fs_H2O*(1-Mix);%[Pa] fuel vapor pressure for mixed droplets
P_cc=500*6894.76;%[Pa]combustion pressure
%molar weights

Mw_N2O=44.013;%[g/mol]
%P_vapf=P_fs*exp((2*sigma*V_m)/(R_D*R*T_s));
GAMMA_fuel_surface=1/( 1+((P_cc)/P_Fs-1)*(Mw_comb/Mw_fuel) );%mass fraction of fuel vapor at
surface
B_M=GAMMA_fuel_surface/(1-GAMMA_fuel_surface);

Cp_eth=6.94;%[kJ/(kg*K)]ethanol Cp https://www.engineeringtoolbox.com/specific-heat-capacity-
ethanol-Cp-Cv-isobaric-isochoric-ethyl-alcohol-
d_2030.html#:~:text=At%20ambient%20pressure%20and%20temperature,v%20%2D%20will%20vary%20with%20te
mperature.
Cp_H2O=Interpolate(41.3685,20,2.635,50,4.74);%specific heat of water at constant pressure just
before injection
Cp_droplet=(Cp_eth*Mix+Cp_H2O*(1-Mix))*1000;%[J/kg*K]
Nu_cc=2*log(1+B_M)/B_M;%Atomization and sprays (8.29)

%thermal conduction of high temperature high pressure air
Temp=[400,600,800,1000,1200,1400,1600];%[C]
k=[50,60,71,80,90,100,110]/1000;%[W/m*K]
Output=polyfit(Temp,k,1);
k_cc_gas=polyval(Output,T_cc);%[J/(m*s*K)]

for i=1:Size_V_inj(1)
 for j=1:Size_V_inj(2)
  h_cc_gas(i,j)=Nu_cc*k_cc_gas/SMD(i,j);%[W/m2*K]
 end
```

```
end
figure
plot(Port_diameter,h_cc_gas,'o-')
xlabel('Injection Port Diameter [m]')
ylabel('Convective Heat Transfer Coefficient [W/m^2*K] ')
title('Droplet Convective Heat Transfer Coefficient Estimation')
grid on
lgd=legend('2','4','6','8','10','Location','northeastoutside');
lgd.Title.String = ('Injector ports');
```

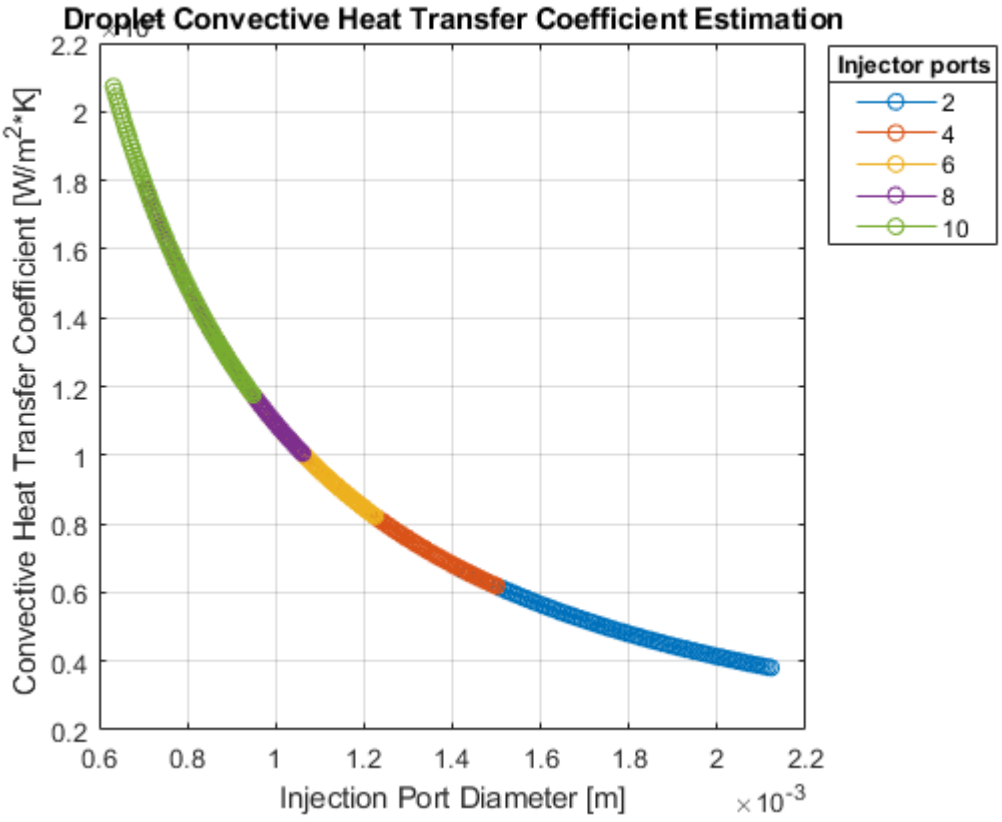

12.1.10Droplet Heat up

```
t_step=.0000001;%[sec] itteration step size
T_boil_H2O=514.9;%[K] at 500 psi
T_boil_eth=206+273.15;%[K] at 500 psi
T_boil=T_boil_eth*Mix+T_boil_H2O*(1-Mix);%[K]
for i=1:Size_V_inj(1)
 for j=1:Size_V_inj(2)
  m_drop(i,j)=pi*(SMD(i,j)/2)^3*4/3*rho_fuel;
 end
end


k=2;
t=[t_step,t_step*2];
```

```
% Change itteration temperature bound so that it turns off at boiling point
% while abs(T(i-1)-T(i))>1e-6%[K] temperature diffrence between itterations
for i=1:Size_V_inj(1)
 for j=1:Size_V_inj(2)
  d_drop=SMD(i,j);
  while T(k)<T_boil%[K] temperature diffrence between itterations
   k=k+1; %counting variable
   Qd(k)=Q_in(d_drop,h_cc_gas(i,j),T_cc,T(k-1))*t_step;%[W]
   T(k)=Qd(k)/(Cp_droplet*m_drop(i,j))+T(k-1);
   t(k)=k*t_step;%[second]
   if k> 1000000
    T(k)=T_boil+1;
   end
  end
  t_heatup(i,j)=t(end);%[sec]
  %   if i==50 && j==3
  %    GGGGG=5;
  %   end

  clear T Qd t
  t=[t_step,t_step*2];
  T=[T_inj,T_inj+.25];%[k] early estimate to get into while loop
  k=2;
 end

end

figure
semilogy(Port_diameter,t_heatup,'o-')
xlabel('Port Diameter')
ylabel('Droplet heatup time')
lgd=legend('2','4','6','8','10','Location','northeastoutside');
lgd.Title.String = ('Injector ports');
grid on

figure
plot(Port_diameter_plot,t_heatup,'o-')
xlabel('Port Diameter [mm]')
ylabel('Droplet heatup time [sec]')
lgd=legend('2','4','6','8','10','Location','northeastoutside');
lgd.Title.String = ('Injector ports');
grid on
```

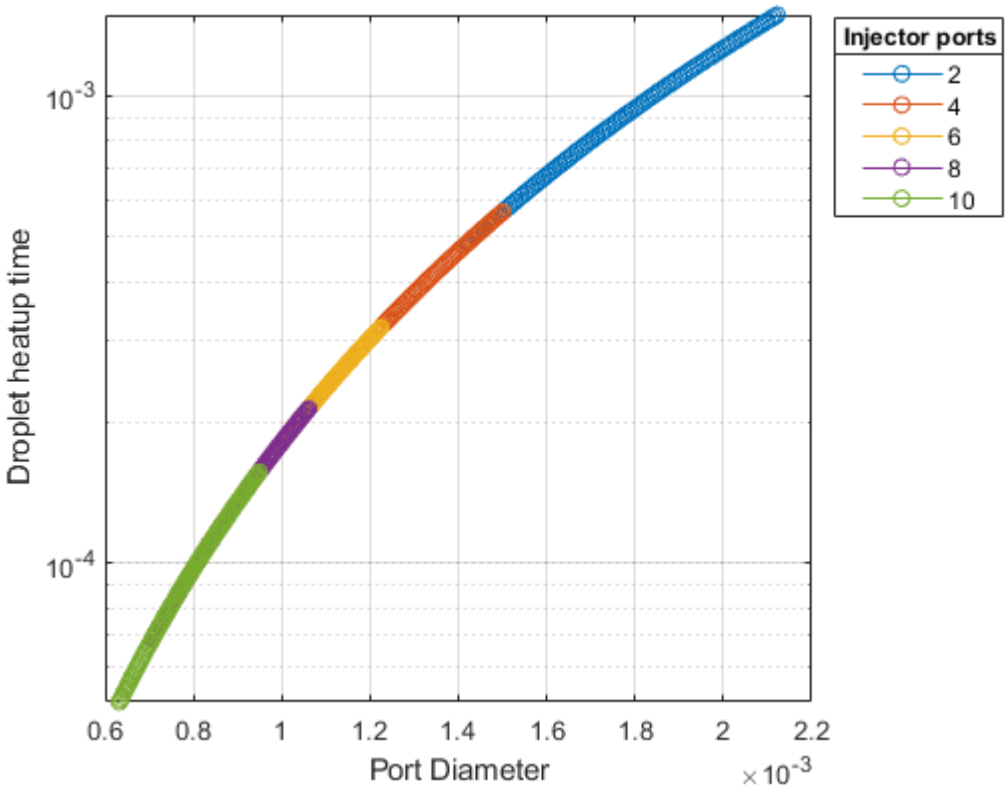
Injector ports
2
4
6
8
10
Droplet heatup time
10^{-3}
10^{-4}
0.6
0.8
1
1.2
1.4
1.6
1.8
2
2.2
Port Diameter
$\times 10^{-3}$

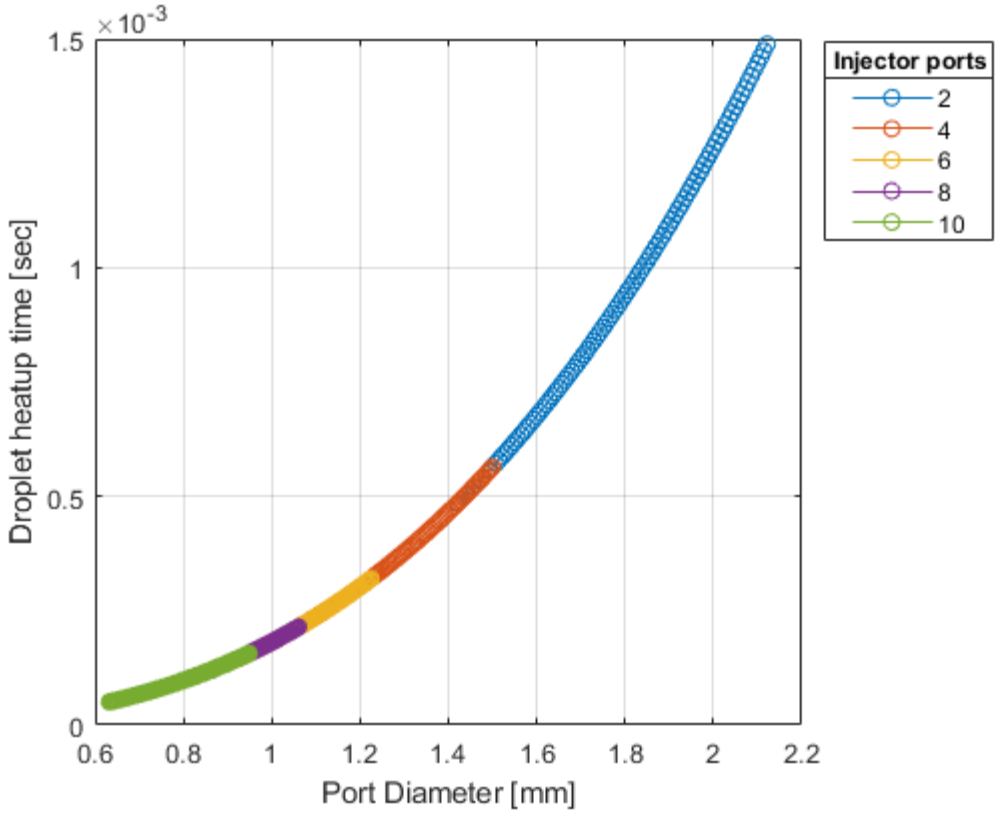
$\times 10^{-3}$
Injector ports
2
4
6
8
10
Droplet heatup time [sec]
1.5
1
0.5
0
0.6
0.8
1
1.2
1.4
1.6
1.8
2
2.2
Port Diameter [mm]

12.1.11Droplet Evaporation

```
m_drop = pi*(D_droplet/2)^3* 4/3*rho_fuel;
k=2;

% P_Fs_ethanol=10^(8.32109 - 1718.1 /(T_boil+ 234.52));%[mmHg] equation from "Lange's Handbook of
Chemistry 1967" pg
P_Fs_ethanol=10^(A-(B/(T_boil+C)));
P_Fs_H2O=.61078*exp(17.27*(T_boil-273.15)/(T_boil-273.15+237.3));%[kPa]Vapor pressure estimation
by Tetens "Tetens, O. 1930. Über einige meteorologische Begriffe. Z. Geophys 6: 207-309"

P_Fs_ethanol=P_Fs_ethanol*10^5;%[Pa]
P_Fs_H2O=P_Fs_H2O*1000;%[pa]

P_Fs=P_Fs_ethanol*Mix+P_Fs_H2O*(1-Mix);%[Pa] fuel vapor pressure for mixed droplets
%molar weights
GAMMA_fuel_surface=1/( 1+((P_cc)/P_Fs-1)*(Mw_comb/Mw_fuel) );%mass fraction of fuel vapor at
surface
B_M=GAMMA_fuel_surface/(1-GAMMA_fuel_surface);

Mw_N2O=44.013;%[g/mol]
Mw_comb=25.74;%[g/mol]
GAMMA_fuel_surface=1/( 1+((P_cc+P_Fs)/P_Fs-1)*(Mw_comb/Mw_fuel) );%mass fraction of fuel vapor at
surface
B_M=GAMMA_fuel_surface/(1-GAMMA_fuel_surface);

B=B_M;%steady state, in Atomization and sprays
lambda_steady=8*k_cc_gas*log(1+B)/(Cp_cc*rho_fuel);%Atomization and Sprays eq 8.25

for i=1:Size_V_inj(1)
 for j=1:Size_V_inj(2)
  m_droplet_loop=m_drop(i,j);
  D_droplet=SMD(i,j);
  k=2;
  t_e=0;%[sec]
  while m_droplet_loop>=0
   md_f_drop=pi/4*rho_fuel*lambda_steady*D_droplet(k-1);%2*pi*D_droplet*(
k/Cp_droplet)*log((1+B));%Check units
   m_droplet_loop=m_droplet_loop-md_f_drop*t_step;
   if m_droplet_loop>0
    D_droplet(k)=(m_droplet_loop/(rho_fuel*pi)*3/4)^(1/3)*2;%[m]
   else
    D_droplet(k)=0;
   end
   t_e(k)=t_e(k-1)+t_step;%[sec] time of evaporation
   k=k+1;
  end
  t_evap(i,j)=t_e(end);%[sec]
  clear D_droplet md_f_drop m_droplet_loop t_e
 end
end
figure
plot(Port_diameter_plot,t_evap,'-o')
```

```
ylabel('Evaporation Time [sec]')
xlabel('Droplet Diameter [mm]')
lgd=legend('2','4','6','8','10','Location','northeastoutside');
lgd.Title.String = ('Injector ports');
grid on
disp(['Droplet evaporation time = ',num2str(t_evap(end-1)),' [sec].'])
t_stay(3)=t_evap(end-1);
```

```
Droplet evaporation time = 0.0010092 [sec].
```

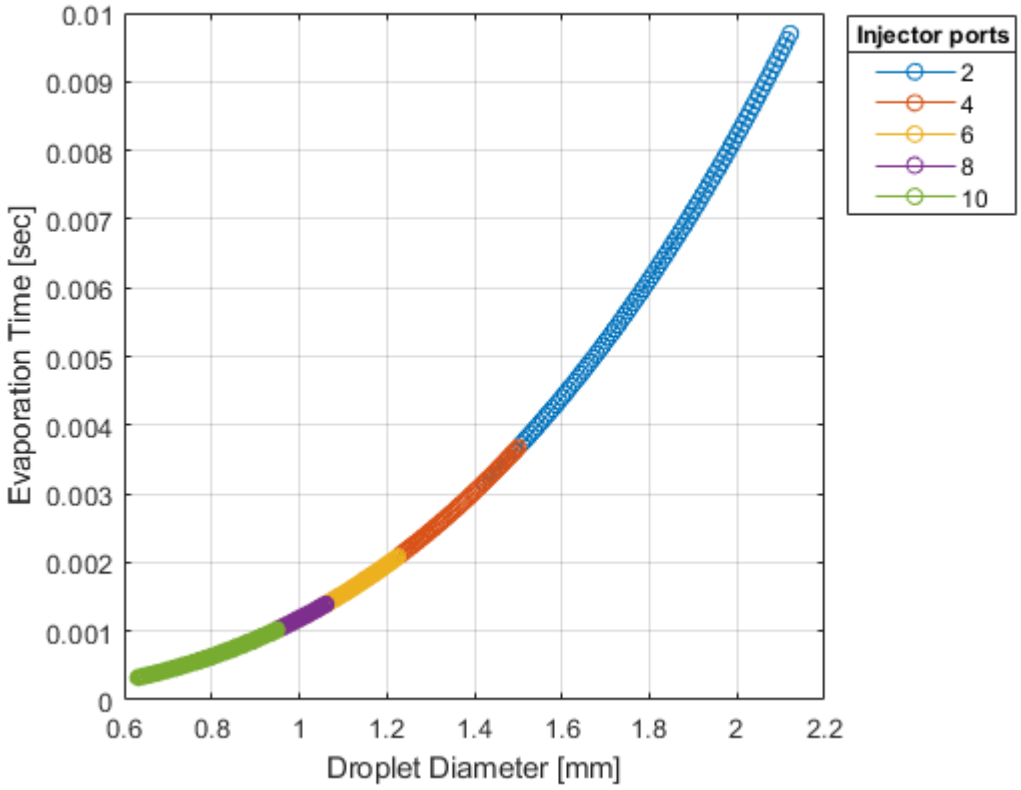

12.1.12L* solve

```
g=9.81;%[m/s2]
for i=1:Size_V_inj(1)
 for j=1:Size_V_inj(2)
  t_stay(i,j)=t_breakup(i,j)+t_heatup(i,j)+t_evap(i,j);
  L_star(i,j)=mdot_NASA CEA/rho_gas*t_stay(i,j)/At;%[m]
 end
end

figure
plot(Port_diameter_plot,t_stay,'-o')
xlabel('Port Diameter [mm]')
ylabel('Residence Time [sec]')
title('Combined Residence Time')
lgd=legend('2','4','6','8','10','Location','northeastoutside');
```

```
lgd.Title.String = ('Injector ports');
grid on

figure
plot(Port_diameter_plot,t_breakup,'-o')
xlabel('Port Diameter [mm]')
ylabel('Time [sec]')
grid on
lgd=legend('2','4','6','8','10','Location','northeastoutside');
lgd.Title.String = ('Injector ports');
title('Time of Droplet Breakup vs Port Diameter')

figure
plot(Port_diameter_plot,t_heatup,'-o')
xlabel('Port Diameter [mm]')
ylabel('Time [sec]')
grid on
lgd=legend('2','4','6','8','10','Location','northeastoutside');
lgd.Title.String = ('Injector ports');
title('Time of Heating vs Port Diameter')

figure
plot(Port_diameter_plot,t_evap,'-o')
xlabel('Port Diameter [mm]')
ylabel('Time [sec]')
grid on
lgd=legend('2','4','6','8','10','Location','northeastoutside');
lgd.Title.String = ('Injector ports');
title('Time of Evaporation vs Port Diameter')


figure
plot(Port_diameter_plot,L_star,'-o')
xlabel('Port Diameter [mm]')
ylabel('Characteristic Length [m]')
lgd=legend('2','4','6','8','10','Location','northeastoutside');
lgd.Title.String = ('Injector ports');
grid on

L_star(94,3);
```

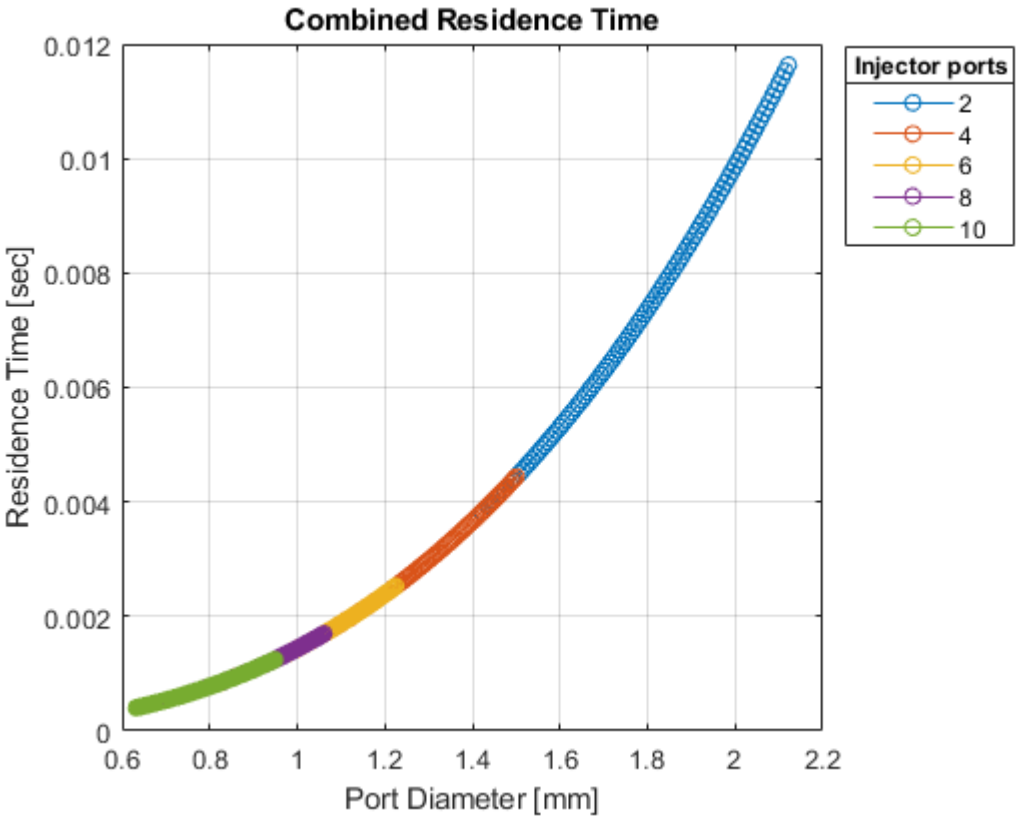
Combined Residence Time
Residence Time [sec]
Port Diameter [mm]
Injector ports
2
4
6
8
10
0.012
0.01
0.008
0.006
0.004
0.002
0
0.6
0.8
1
1.2
1.4
1.6
1.8
2
2.2

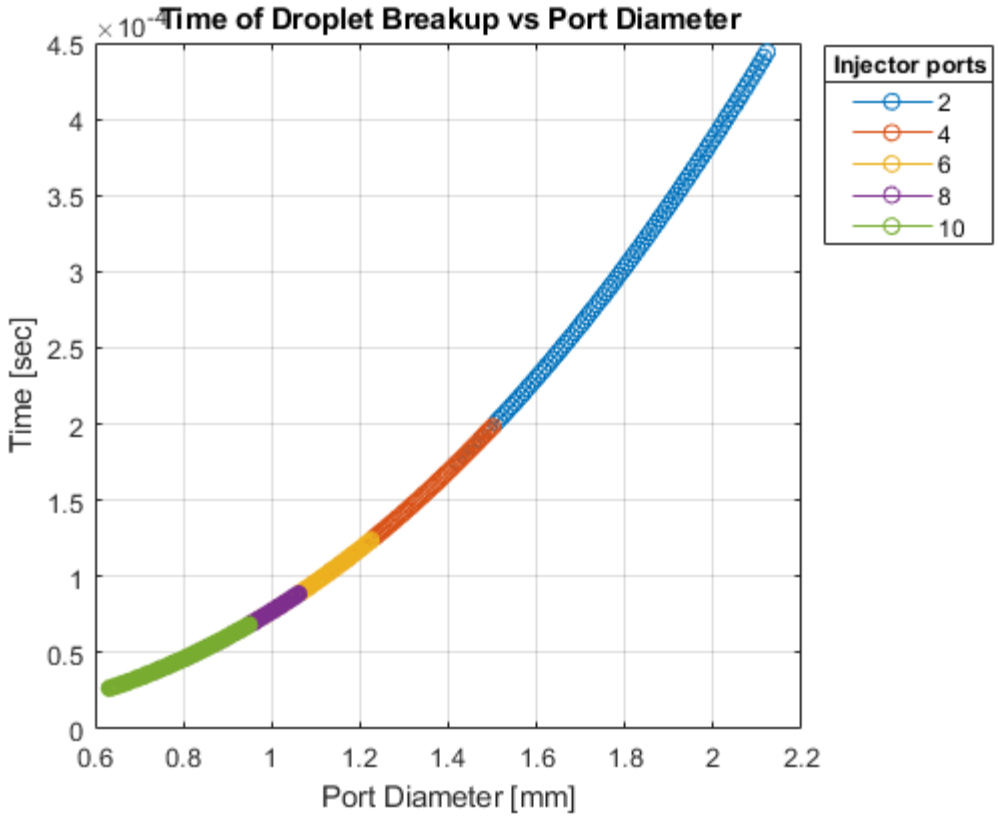
Time of Droplet Breakup vs Port Diameter
×10^-4
Time [sec]
Port Diameter [mm]
Injector ports
2
4
6
8
10
4.5
4
3.5
3
2.5
2
1.5
1
0.5
0
0.6
0.8
1
1.2
1.4
1.6
1.8
2
2.2

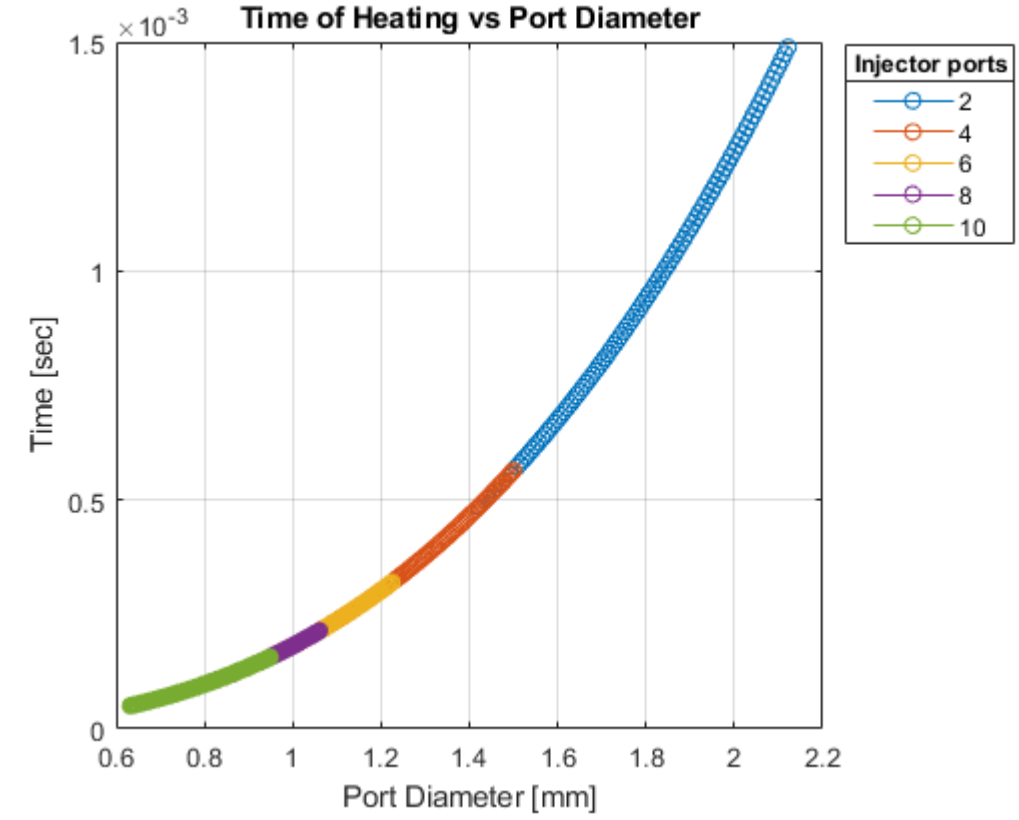
Time of Heating vs Port Diameter
×10^-3
1.5
1
0.5
0
Time [sec]
0.6
0.8
1
1.2
1.4
1.6
1.8
2
2.2
Port Diameter [mm]
Injector ports
2
4
6
8
10

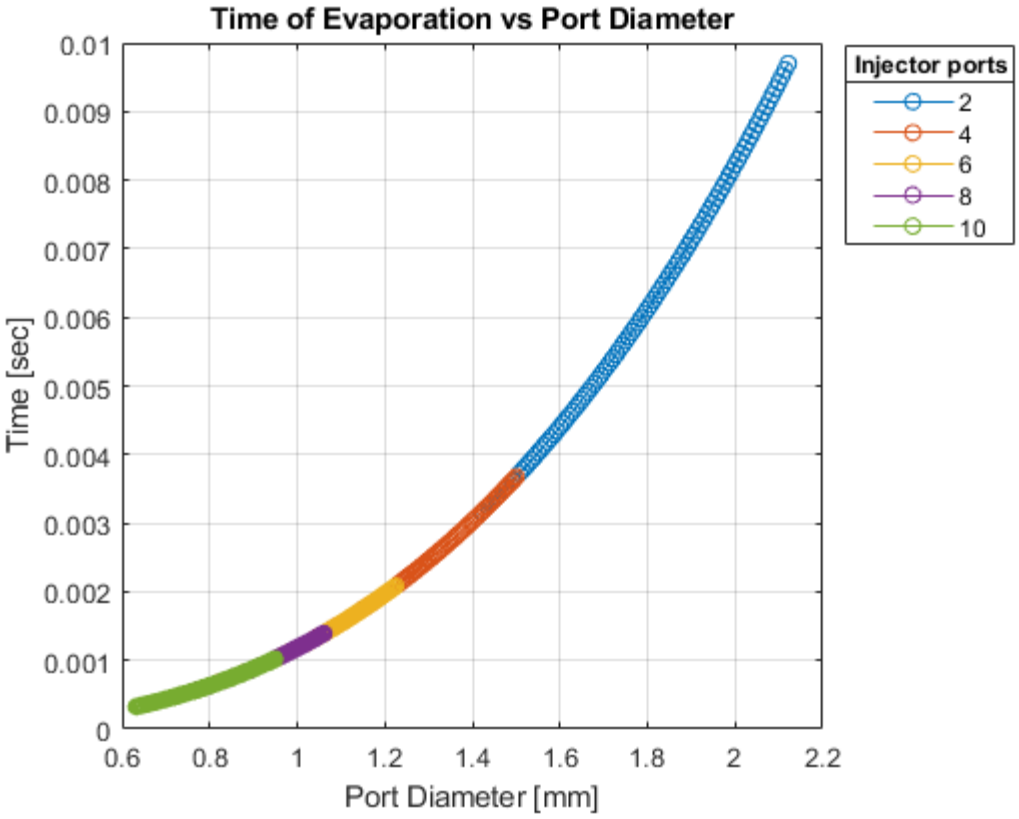
Time of Evaporation vs Port Diameter
0.01
0.009
0.008
0.007
0.006
0.005
0.004
0.003
0.002
0.001
0
Time [sec]
0.6
0.8
1
1.2
1.4
1.6
1.8
2
2.2
Port Diameter [mm]
Injector ports
2
4
6
8
10

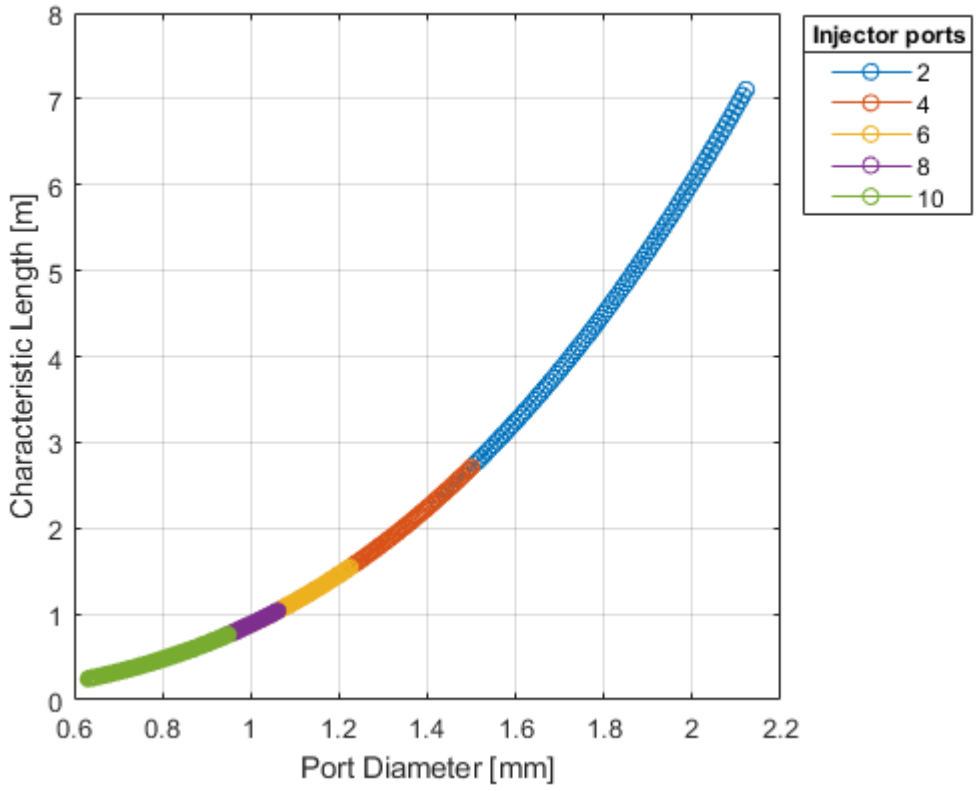

12.1.13Functions

```
function [Z] = Zsolve(mu_L,rho_L,sigma,d_orf)
% mu_L = liquid dynamic viscosity
% rho_L = lquid density
% sigma = surface tension
% d_orf = diameter of injection port

Z=mu_L/((rho_L*sigma*d_orf)^.5);
end

function [T_r,P_r] = Reduced_solve(flag,T,P)
%NOTE: INPUTS ARE KELVIN AND PASCALS
%solved for reduced temp and pressure
%flag=liquid identifier
%1==N2O
%2==Ethanol
%3==H2O
%P == [Pa]
%T == [K]
if flag == 1%N2O
 T_crit = 309.6;
 P_crit = 7.26e6;
elseif flag == 2 %Ethanol
 T_crit = 514;
 P_crit = 6.3e6;
```

```
elseif flag == 3 %H2O
 T_crit = 647;
 P_crit = 22.06e6;
else
 warning('No valid flag input')
end
T_r=T/T_crit;
P_r=P/P_crit;
end

function [Re] = Reynold(rho,V,D,mu)
%Calculates the reynolds number of a fluid in a pipe
%rho = fluid denisty [kg/m3]
%V = fluid velocity [m/s]
%D = pipe diamter [m]
%mu = fluid dynamic viscosity [kg/(m*s)]
Re=(rho*V*D)/mu;
end

function [We] = Weber(rho,v,L,sigma)
%rho== density
%v== velocity
%L== characeristic length (droplet diameter)
%sigma== surface tension
We=rho*v^2*L/sigma;%[unitless]
end

function [T_out]=Droplet_heating(T_droplet,D_droplet,rho_droplet,T_gas,rho_gas)
%ASSUMPTIONS:
%1.Drop is spherical
%2.Fuel is pure liquid with a well defined boiling point
%3.Ratiation heat transfer is negligible, not exactly true but this assumption will
%over estimate

%4.No heat was transfered to the droplet durring the breakup process

%from Atomization and sprays Page 218
%NOTE: these assumptions are valid unless the combution is at low pressure
%and the flame is very luminous.

Vol_drop=4/3*pi*(D_droplet/2)^3;%[m]
SA_drop=4*pi*(D_droplet/2)^2;%[m]
Lc=Vol_drop/SA_drop;%[m]


end

function [y] = Interpolate(x,x1,y1,x2,y2)
%This code does linear interpolation
y=y1+((x-x1)/(x2-x1))*(y2-y1);
end

function [At,rt] = Throat_area(F,k,M,P_e,P_cc,T_cc,rho_t)
%This code determines the throat area based on required thrusat and burn
```

```
%characteristics

%F=thrust[N]
%k=ratio of specific heats (assumed constant through length of chamber) [UL]
%M=molar mass [kg/mol]
%T_cc temperature in combustion chamber [K]
%rho_t= gas density in throat [kg/m3]
%P_e=exit pressure [Pa]
%P_cc=Combustion Pressure [Pa]
%R=specific gas constant
M=M/1000;%[g/mol] changes molar density from g/mol NASA output to kg/mol output
R_univ=8.314;%[J/mol*K]
R=R_univ/M;%[J/kg*K]
At=F/( sqrt((2*k)/(k-1)*R*T_cc*(1-(P_e/P_cc)^((k-1)/k)))*(sqrt(T_cc/(1+((k-
1)/2)))*rho_t*sqrt(R*k)) );
rt=sqrt(At/pi);
end

function [Ae,eps] = Nozzle_Expansion(At,k,Pc,Pe)
Ae=At*( (2/(k+1))^(1/(k-1))*(Pc/Pe)^(1/k)*((k+1)/(k-1)*( 1-(Pc/Pe)^((1-k)/k) ))^(-1/2) );%exit
area
eps=Ae/At;%nozzle expansion ratio
end

function [Mdot] = Mdot_Thrust(F,M,Tc,Pe,Pc,k)
%This function determines mass flow rate from the thrust enge engine
%conditions

%F=Thrust[N]
%M=molar mass[g/mol]
%Tc= combustion temperature [K]
%Pe/Pc=ratio of combustion pressure to exit pressure
%k=ratio of specific heats

M=M/1000;%[kg/mol]
R_=8.314;%[J/(mol*K)]
R=R_/M;%[J/(kg*K)]
Mdot=F/( sqrt( 2*k/(k-1)*R*Tc*(1-(Pe/Pc)^((k-1)/k)) ) );%[kg/sec]
end

function Q=Q_in(D,h,T_inf,T_surf)
Q=pi*4*(D/2)^2*h*(T_inf-T_surf);
end
```

12.1.14NASA CEA Output

```
**************************************************************************
***************

    NASA-GLENN CHEMICAL EQUILIBRIUM PROGRAM NASA CEA2, FEBRUARY
5, 2004
```

```
     BY BONNIE MCBRIDE AND SANFORD GORDON
  REFS: NASA RP-1311, PART I, 1994 AND NASA RP-1311, PART II,
1996


*************************************************************
***************

 ### NASA CEA analysis performed on Tue 27-Apr-2021 13:53:18

 # Problem Type: "Rocket" (Infinite Area Combustor)

 prob case=1234___________1791 ro equilibrium

 # Pressure (1 value):
 p,psia= 500
 # Chamber/Exit Pressure Ratio (1 value):
 pi/p= 34

 # Oxidizer/Fuel Wt. ratio (1 value):
 o/f= 2.1647

 # You selected the following fuels and oxidizers:
 reac
 fuel C2H5OH(L)   wt%= 70.0000 t,k= 303.000
 fuel H2O(L)   wt%= 30.0000 t,k= 303.000
 oxid N2O    wt%=100.0000 t,k= 303.000

 # You selected these options for output:
 # short version of output
 output short
 # Proportions of any products will be expressed as Mass
Fractions.
 output massf
 # Heat will be expressed as siunits
 output siunits

 # Input prepared by this script:/var/www/sites/NASA
CEArun.grc.nasa.gov/cgi-bin/NASA CEARU
 N/prepareInputFile.cgi

 ### IMPORTANT: The following line is the end of your NASA CEA
input file!
 end



    THEORETICAL ROCKET PERFORMANCE ASSUMING EQUILIBRIUM

   COMPOSITION DURING EXPANSION FROM INFINITE AREA COMBUSTOR

 Pin = 500.0 PSIA
```

```
 CASE = 1234___________

    REACTANT      WT FRACTION   ENERGY  TEMP
          (SEE NOTE)  KJ/KG-MOL  K
 FUEL  C2H5OH(L)     0.7000000 -276960.929 303.000
 FUEL  H2O(L)      0.3000000 -285464.615 303.000
 OXIDANT  N2O       1.0000000  82240.382 303.000

 O/F= 2.16470 %FUEL= 31.598572 R,EQ.RATIO= 1.518140
PHI,EQ.RATIO= 1.853647

     CHAMBER THROAT  EXIT
 Pinf/P   1.0000 1.7954 34.000
 P, BAR   34.474 19.202 1.0139
 T, K    2343.63 2097.60 1169.79
 RHO, KG/CU M 3.9460 0 2.4566 0 2.3265-1
 H, KJ/KG  -1553.77 -2037.72 -3782.50
 U, KJ/KG  -2427.41 -2819.35 -4218.32
 G, KJ/KG  -26855.2 -24683.0 -16411.4
 S, KJ/(KG)(K) 10.7958 10.7958 10.7958

 M, (1/n)   22.304 22.313 22.317
 (dLV/dLP)t  -1.00029 -1.00010 -1.00002
 (dLV/dLT)p  1.0071 1.0024 1.0002
 Cp, KJ/(KG)(K) 2.0122 1.9444 1.8585
 GAMMAs   1.2309 1.2383 1.2508
 SON VEL,M/SEC  1037.0 983.8 738.3
 MACH NUMBER  0.000 1.000 2.860

 PERFORMANCE PARAMETERS

 Ae/At      1.0000 4.9205
 CSTAR, M/SEC    1426.4 1426.4
 CF       0.6897 1.4802
 Ivac, M/SEC    1778.3 2317.7
 Isp, M/SEC     983.8 2111.3

 MASS FRACTIONS

 *CO    0.19596 0.19027 0.13235
 *CO2    0.11472 0.12365 0.21466
 *H    0.00003 0.00001 0.00000
 *H2    0.01262 0.01304 0.01722
 H2O    0.24105 0.23760 0.20041
 NH3    0.00001 0.00001 0.00001
 *NO    0.00003 0.00001 0.00000
 *N2    0.43534 0.43535 0.43536
 *OH    0.00024 0.00006 0.00000

 * THERMODYNAMIC PROPERTIES FITTED TO 20000.K
 NOTE. WEIGHT FRACTION OF FUEL IN TOTAL FUELS AND OF OXIDANT IN
TOTAL OXIDANTS
```

12.2 Injector Pressure Drop Estimation

```
%Alec Bluhm
%Pressure drop estimation
clear;
close all;
% clc;

md_fuel=.0393;%[kg/s]

rho_f=851.4;%[kg/m3] from L_star_solveV4_1

Injection_diameter_fuel=linspace(.002,.003,100);%[m] injection port diameters
N=[2,4,6,8,10];%number of injection ports

P_i_ox=800*6894.76;%[Pa] oxidizer initial pressure
P_i=730*6894.76;%linspace(550,750,10)*6894.76;%[Pa]


OF=3.75;
md_ox=md_fuel*OF;
rho_ox=1.22*1000;%[kg/m3]
Injection_diameter_ox=linspace(.002,.003,100)*3;%[m]
P2=500*6894.76;%[Pa]
for k =1:length(P_i)
 for j=1:length (N)
  for i=1:length (Injection_diameter_fuel)
   A_fuel(i,j,k)=pi*(Injection_diameter_fuel(i)/2)^2/N(j);%[m2]
   A_ox(i,j,k)=pi*(Injection_diameter_ox(i)/2)^2/(N(j)*2);%Assumes only matched pair of ox to
fuel ports
   Port_diameter_fuel(i,j,k)=Injection_diameter_fuel(i)/sqrt(N(j));%[m]
   Port_diameter_ox(i,j,k)=Injection_diameter_ox(i)/sqrt(N(j)*2);%[m]
   A_port_fuel(i,j,k)=pi*(Port_diameter_fuel(i,j,k)/2)^2;%[m2]
   A_port_ox(i,j,k)=pi*(Port_diameter_ox(i,j,k)/2)^2;%[m2]
   if Port_diameter_fuel(i,j,k) <= .001%Assuming L/D >3.0
    Cd_fuel(i,j,k)=.88; %From Sutton 279
   elseif Port_diameter_fuel(i,j,k) <= .00157%Assuming L/D >3.0
    Cd_fuel(i,j,k)=.89;
   else
    Cd_fuel(i,j,k)=.9;%From Sutton 279
   end
   if Port_diameter_ox(i,j,k) <= .001%Assuming L/D >3.0
    Cd_ox(i,j,k)=.88; %From Sutton 279
   elseif Port_diameter_ox(i,j,k) <= .00157%Assuming L/D >3.0
    Cd_ox(i,j,k)=.89;
   else
    Cd_ox(i,j,k)=.9;%From Sutton 279
   end
   P_f_fuel(i,j,k)=P_i(k)-( (md_fuel/(Cd_fuel(i,j)*A_port_fuel(i,j)))^2/(2*rho_f ));%adapted from
Sutton pg 281
   if P_f_fuel(i,j,k) < 0
    P_f_fuel(i,j,k)=0;
   end
```

```
   %    P_f_ox(i,j,k)=P_i(k)+(abs(P_i(k)-P_f_fuel(i,j,k)))*(rho_f/rho_ox)*...
   %     (OF*(Cd_fuel(i,j,k)/Cd_ox(i,j,k))*(A_fuel(i,j)/A_ox(i,j)))^2;
   P_f_ox(i,j,k)=P_i(k)+(
((OF*Cd_fuel(i,j)*A_port_fuel(i,j)/(Cd_ox(i,j)))^2*(rho_f*(P_f_fuel(i,j)-P_i)))/(
rho_ox*A_port_ox(i,j)^2 ) );%[Pa]
   if P_f_fuel(i,j,k) == 0
    P_f_ox(i,j,k)=0;
   end
   if P_f_fuel(i,j,k) < P2
    mdot_fuel(i,j,k)=0;
   else
    mdot_fuel(i,j,k)=A_port_fuel(i,j,k)*sqrt( (P_f_fuel(i,j,k)-P2)*2*rho_f);
   end

   if P_f_ox(i,j,k) < P2
    mdot_ox(i,j,k)=0;
   else
    mdot_ox(i,j,k)=A_port_ox(i,j,k)*sqrt( (P_f_ox(i,j,k)-P2)*2*rho_ox);
   end

  end
 end
end

disp('All outputs that fall below the black line are not possible with a chamber pressure of 500
psi')

figure
hold on
for i=1:length(P_i)
 plot(Port_diameter_fuel(:,:,i)*1000,mdot_fuel(:,:,i),'-o')
end
yline (md_fuel)
xlabel('Port Diameter [mm]')
ylabel('Mass Flow Rate [kg/s]')
lgd=legend('2','4','6','8','10','Nonfeasible line','Location','northeastoutside');
lgd.Title.String = ('Injector ports');
grid on
xticks(.6:.05:2.2)

figure
hold on
for i=1:length(P_i)
 plot(Port_diameter_ox(:,:,i)*1000,mdot_ox(:,:,i),'-o')
end
yline (md_ox)
xlabel('Port Diameter [mm]')
ylabel('Mass Flow Rate [kg/s]')
lgd=legend('4','8','12','16','20','Nonfeasible line','Location','northeastoutside');
lgd.Title.String = ('Injector ports');
grid on

figure
plot(Port_diameter_fuel*1000,P_f_fuel,'-o')
```

```
xlabel('Port Diameter [mm]')
ylabel('Pressure After Injection [Pa]')
title('Fuel')
yline(500*6897.76)
lgd=legend('2','4','6','8','10','Nonfeasible line','Location','northeastoutside');
lgd.Title.String = ('Injector ports');
grid on

figure
plot(Port_diameter_fuel*1000,P_f_fuel/6897.76,'-o')
xlabel('Port Diameter [mm]')
ylabel('Pressure After Injection [psi]')
yline(500)
lgd=legend('2','4','6','8','10','Nonfeasible line','Location','northeastoutside');
lgd.Title.String = ('Injector ports');
title('Ethanol/Water Mixture')
grid on

figure
plot(Port_diameter_ox*1000,P_f_ox/6897.76,'-o')
xlabel('Port Diameter [mm]')
ylabel('Pressure After Injection [psi]')
title('Oxidizer')
yline(500)
lgd=legend('4','8','12','16','20','Nonfeasible line','Location','northeastoutside');
lgd.Title.String = ('Injector ports');
grid on


N_input=input('Number of fuel injection ports: ');
N_input=N_input/2;
N_input_ox=input('Number of oxidizer injection ports: ');
N_input_ox=N_input_ox/4;

D_input=input('Requested Port Diameter [mm]: ');
D_input=D_input/1000;%[m] sets to scale of solved diameters
Loc=Search(Port_diameter_fuel(:,N_input),D_input);

if P_f_fuel(Loc,N_input)<= 500*6894.76
 warning ('Pressure after chosen injector setup is too low')
 warning(['Post injector pressure is',num2str(P_f_fuel(N_input,Loc)),' [psi]'])
end
disp(['Closest fuel port diameter to requested diameter is ',num2str(Port_diameter_fuel
(Loc,N_input)*1000),' [mm]'])
disp(['Closest oxidizer port diameter to requested diameter is ',num2str(Port_diameter_ox
(Loc,N_input_ox)*1000),' [mm]'])
disp(['the supply pressure is ',num2str(P_i),' [Pa] or ',num2str(P_i/6894.76),' [psi].'])
```

12.2.1 Functions

```
function [Loc] = Search(Search_index,input_value)
%This function returns a location for the closest value in a search index
```

```
%compared value. Use single column to search.
for i=1:length(Search_index)
 Diff(i)=abs(Search_index(i)-input_value);
end
[~,Loc]=min(Diff);
if Loc==length(Search_index)
 warning('Closest value is at end of matrix, possibly not representative')
end
end
```

12.3 Coolant Port Sizing

```
%Alec Bluhm
%5/6/2021
%Film coolant port/slot sizing
```

12.3.1 House keeping

```
clear;
close all;
clc;
```

12.3.2 Constants and Analysis

```
mdot=.2086;%[kg/sec] total engine mass flow rate
md_film=[.05,.05,.028]*mdot;%[kg/sec]
rho=851.4;%[kg/m3] fuel density
Mix=.7;
M1_H2O=1482;%[m/s] speed of sound in liquid water at room temperautre
M1_ethanol=1159;%[m/s] speed of sound of liquid ethanol at room temperature
M1_fuel=M1_ethanol*Mix+M1_H2O*(1-Mix);%[m/s]
V_inj_max=M1_fuel*.3;%[m/s] point at which incompressible fluid is no longer a valid assumption
V_inj=linspace(V_inj_max*.001,V_inj_max*.05,1000);
Port_spacing=.3*25.4;%[mm] from NASA SP8124 pg 88
Circ=pi*2*[19.75,19.75,17.23];%[mm] where 19.75 is the circumfrence at that point
Port_Number=Circ/Port_spacing;
Port_round=round(Port_Number);
for i=1:3
 if Port_round(i) < Port_Number(i)
  Port_Number(i)=Port_round(i)+1;
 else
  Port_Number(i)=Port_round(i);
 end
end


for i=1:length(V_inj)
 for j=1:length(md_film)
  A_film_inj(i,j)=md_film(j)/(rho*V_inj(i))*1000*1000;
 end
```

```
end
figure
semilogy(A_film_inj,V_inj)
xlabel('Port Total Injection Area [mm^2]')
ylabel('Film Injeciton Velocity [m/s]')
lgd=legend(num2str(md_film(1)),num2str(md_film(2)),num2str(md_film(3)),'Location','northeastoutsi
de');
lgd.Title.String = ('Film mdot');
grid on

for i=1:length(V_inj)
 for j=1:length(md_film)
  slot_height(i,j)=A_film_inj(i,j)/Circ(j);
  Port_area(i,j)=A_film_inj(i,j)/Port_Number(j);
  Port_diameter(i,j)=sqrt(Port_area(i,j)/pi)*2;
 end
end
figure
plot(A_film_inj,slot_height)
xlabel('Injection Film Area [mm^2]')
ylabel('Slot height [mm]')
lgd=legend(num2str(md_film(1)),num2str(md_film(2)),num2str(md_film(3)),'Location','northeastoutsi
de');
lgd.Title.String = ('Film mdot');

figure
plot(V_inj,slot_height)
xlabel('Injection Velocity [m/s]')
ylabel('Slot height [mm]')
lgd=legend(num2str(Circ(1)/2/pi),num2str(Circ(2)/2/pi),num2str(Circ(3)/2/pi),'Location','northeas
toutside');
lgd.Title.String = ('Injection Circumference [mm]');
grid on

figure
plot(V_inj,Port_diameter(:,2:3))
xlabel('Injection Velocity [m/s]')
ylabel('Port Diameter [mm]')
lgd=legend(num2str(Port_Number(2)),num2str(Port_Number(3)),'Location','northeastoutside');
lgd.Title.String = ('Number of Injector Ports');
grid on
```

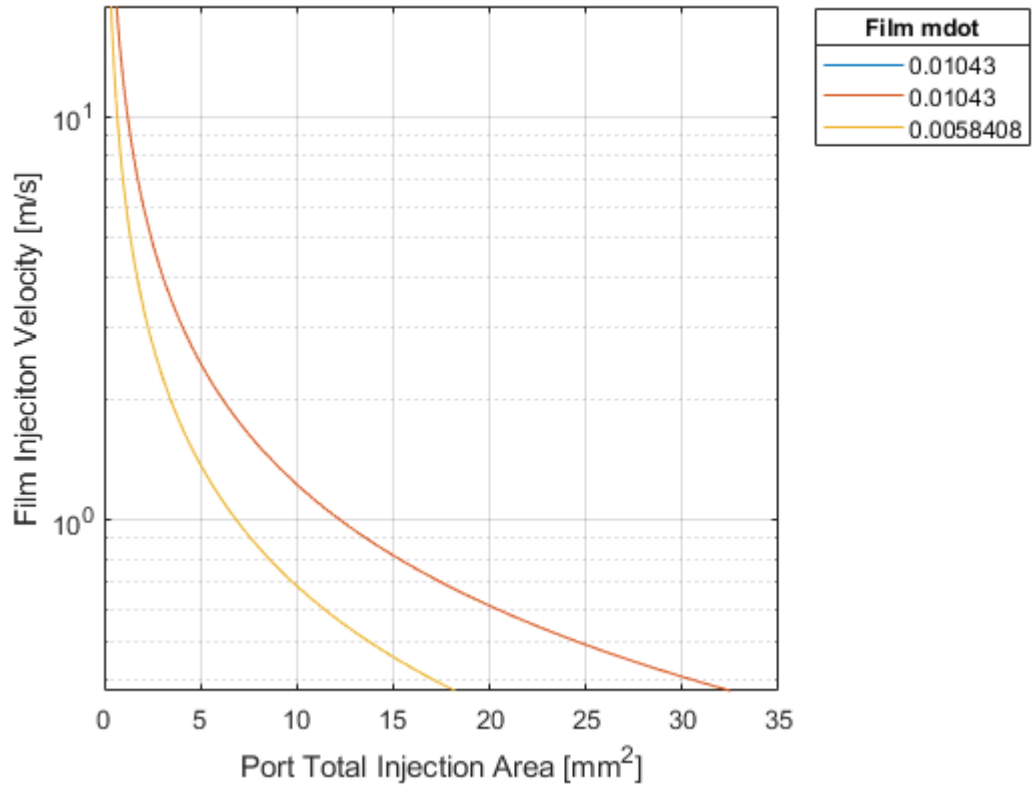
Film mdot
0.01043
0.01043
0.0058408
Film Injeciton Velocity [m/s]
10^1
10^0
0
5
10
15
20
25
30
35
Port Total Injection Area [mm^2]

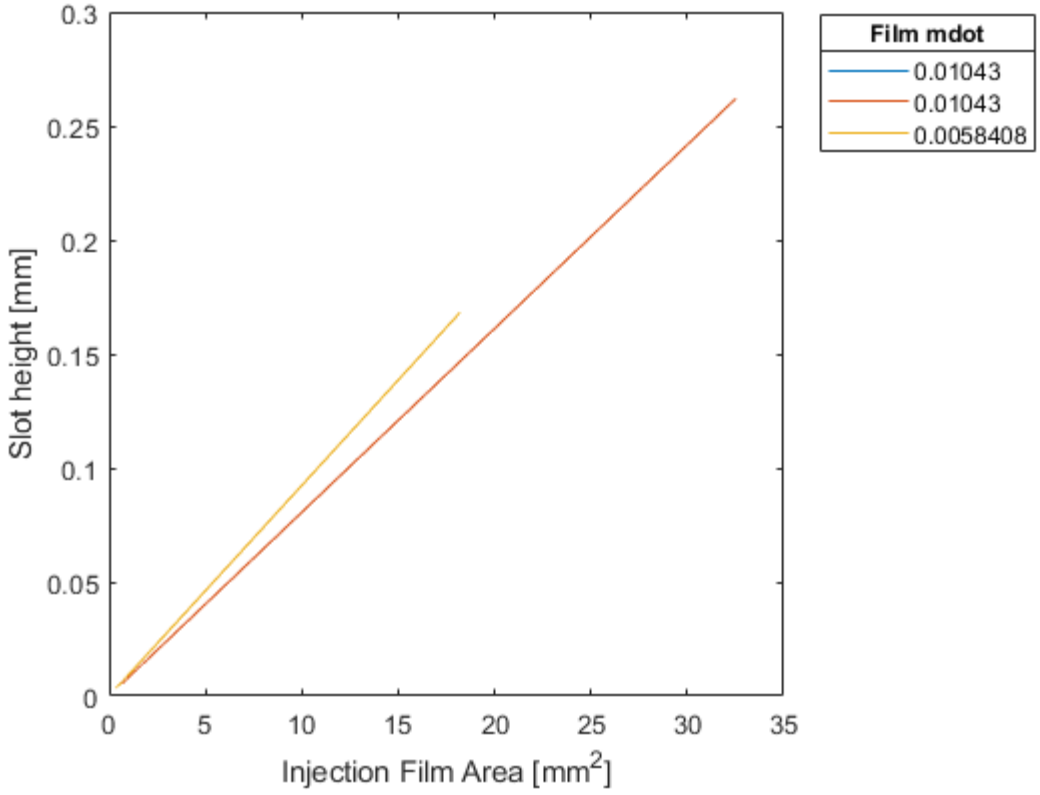
Film mdot
0.01043
0.01043
0.0058408
Slot height [mm]
0.3
0.25
0.2
0.15
0.1
0.05
0
0
5
10
15
20
25
30
35
Injection Film Area [mm^2]

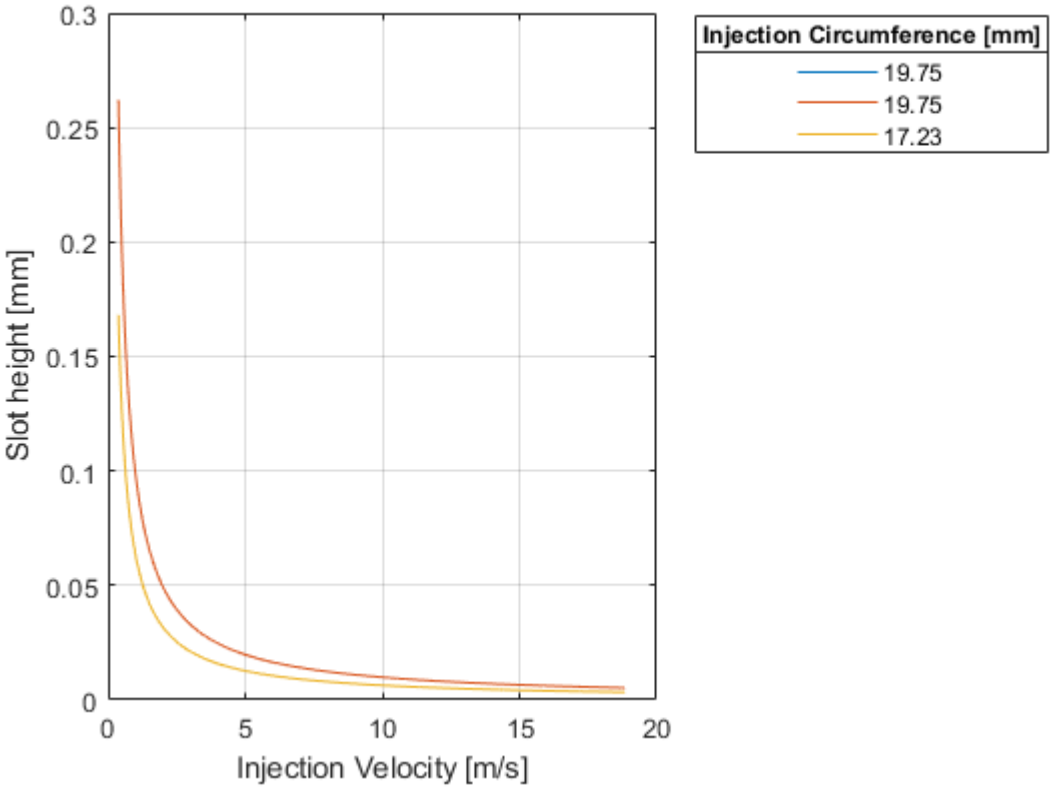
Injection Circumference [mm]
19.75
19.75
17.23
Slot height [mm]
0.3
0.25
0.2
0.15
0.1
0.05
0
0
5
10
15
20
Injection Velocity [m/s]

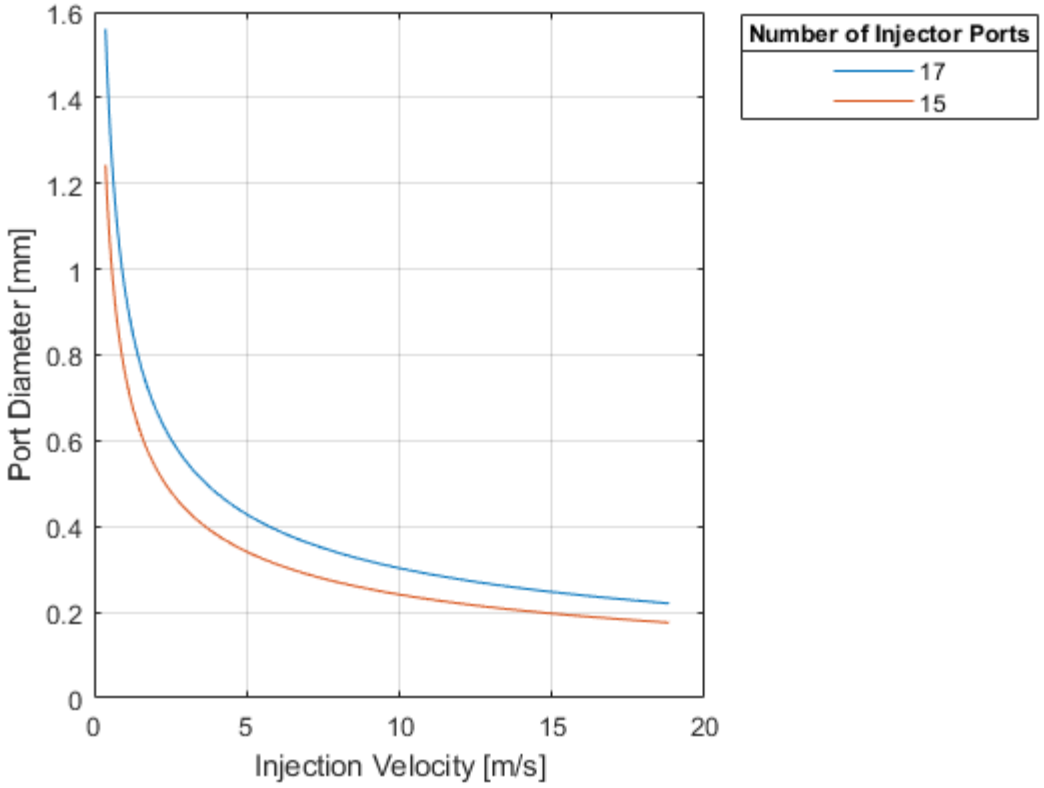
Number of Injector Ports
17
15
Port Diameter [mm]
1.6
1.4
1.2
1
0.8
0.6
0.4
0.2
0
0
5
10
15
20
Injection Velocity [m/s]

12.4 Ethanol Viscosity Visualization

```
%Alec Bluhm
%Ethyl alcohol viscosity by temp

clear;
close all;
clc;
warning off

Temp=[273,293,303,323,343,513];%[K] Values from DDBT
mu=[.00177,.0012,.001,.0007,.0005,15.14e-6];%[kg/m*s] dynamic viscoity
T_crit=240.75+273.15;%[K] critical tempreature of ethanol

P=polyfit(Temp,mu,4);
Temp_plot=linspace(Temp(1),T_crit);
mu_plot=polyval(P,Temp_plot);

figure
semilogy(Temp,mu,'x-')
hold on
grid on
xlabel('Temperature [K]')
ylabel('Viscosity [kg/m*s]')
title('Ethanol Viscosity')
```

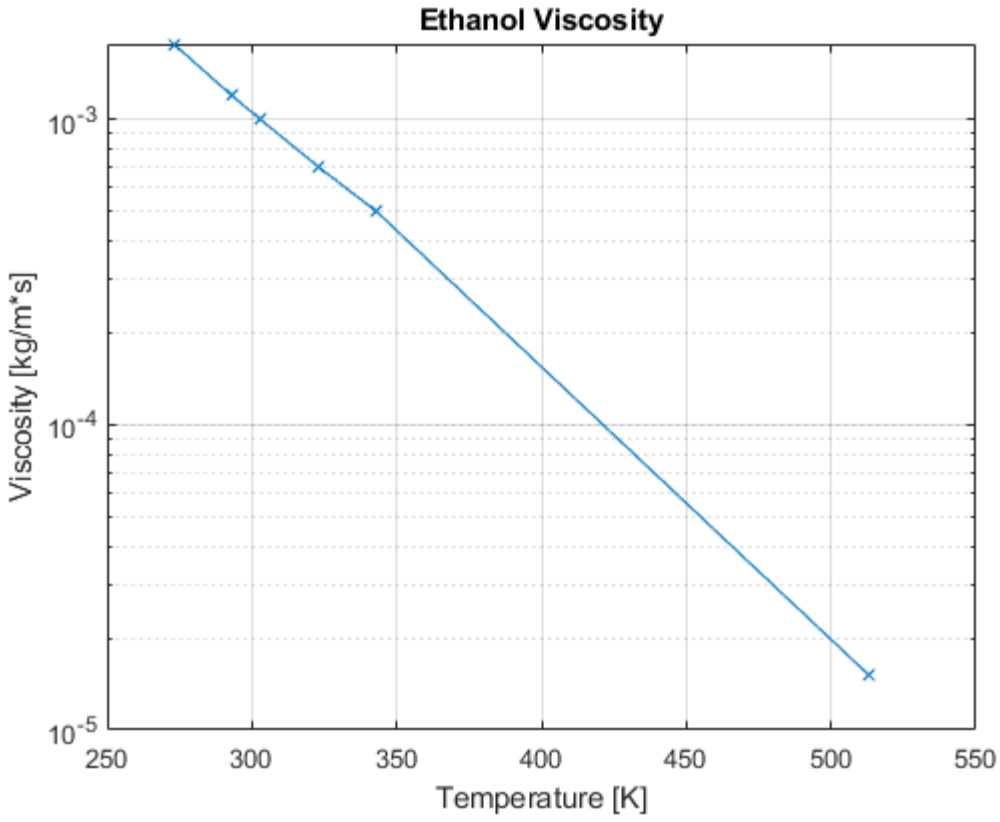

12.5 General Use Functions

The functions below are all used in larger scripts.

12.5.1 Gas Side Heat Transfer

```
function [hg1,hg2] =
Gas_side_heat_coeff(Dt,A,Twg,T_nozz,P_nozz,k,M,R,Cp,c_star,mu,Pr,rho_free,V_free,flag)
%this code outputs 3 estimations for the hot gas heat coefficient. all
%equations applied are from Modern Engineering for Design of
%Liquid-Propellant Rocket Engines

% _-_ denotes a pull from NASA CEA or RPA
%|_| denotes a selection in code
%___ denotes solved in this function

%variable definitions
%_-_ rho_free=free stream gas density
%_-_ V_free=free stream gas velocity
%_-_ mu=dynamic viscosity
%_-_Cp= specific heat at constant pressure
%_-_ k=ratio of specific heats
%|_| Twg=hot gas side local chamber wall temperature
%___Tc_ns= nozzle stagnation temperature
%___ Pr= prandlt number
%|_| Dt= hydraulic diameter of the throat
%_-_ c_star= characteristic velocity
%_-_ R=nozzle radius of curavture at throat
%|_| A=area along chamber axis
%___ At=area at throat
%g= acceleration due to gravity ??? CHECK THIS
%sigma=Correction factor for property variations across the boundry layer
%_-_ M= local speed of sound
%Mol= molecular weight
%_-_ T_nozz=temperature at nozzle throat

%Variable setting from input
At=pi*(Dt/2)^2;%[m2] area of the throat

%theory
Tc_ns=T_nozz*(1+(k-1)/2*M^2);%calculates nozzle stagnation temperature
Pc_ns=P_nozz*(1+(k-1)/2*M^2)^(k/(k-1));
%Estimates Pr and mu if unknown values
if Pr==0 && mu==0
 Pr=4*k/(9*k-5);
 mu=Pr*k/Cp;
 disp('Prandlt number and dynamic viscosity approximation used.')
elseif Pr==0 && mu ~=0
 Pr=mu*Cp/k;%[]Specific heat at constant pressure
end
if mu ==0
 Mol=input('Input molecular weight of combusting gasses then press enter: ');
 T__=input('Input local temperature: ');
```

```
 mu=46.6e-10*Mol^.5*T__^.6;% where M and Tcc are the molecular weight and local temperature
 disp('Dynamic viscosity approximaiton used.')
end

if flag == 1
 %Converts inputs to imperial becuase the equation is designed for
 %imperial input
 Dt=Dt*.0254;%[in]
 Twg=Twg*1.8;%[R] converts Kelvin to Rankine
 T_nozz=T_nozz*1.8;%[R] converts Kelvin to Rankine
 R=R*.0254;%[in]
 Cp=Cp/4186;%[BTU/(lbm*F)] from J/(kg*C)
 c_star=c_star*3.28084;%[ft/s] from [m/s]
 mu=mu*0.6672*12;%[lbm/(in*s)] from [Pa*s]
elseif flag == 0
else
 disp('Input a valid flag command, 1=metric input, 0= imperial input')
end
g= 32.174;%[ft/s2]
sigma=1/( (.5*(Twg/Tc_ns)* (1+(k-1)/2*M^2)+.5 )^.68 * (1+(k-1)/2*M^2)^.12 );%correction factor
for property variations
hg1=( .026/Dt^.2*(mu^.2*Cp/Pr^.6) *(Pc_ns*g/c_star)^.8*(Dt/R)^.1 )*(At/A)^.9*sigma;%
NOTE:(mu^.2*Cp/Pr^.6) is "ns" (nozzle stagnation)
hg1=hg1*1055*1550*1.8;%[J/(m2*s*K)] converted from [BTU/(in2*s*R)]
%estimation
if V_free ==0
 disp('hg2 not applicable for stationary flow')
end
hg2=(rho_free*V_free)^.8;
end
```

12.5.2 Heat Transfer Combined

```
function [H] = HeatTrans_full(h_gc,t,k,h_c)
%This code outputs an overall heat transfer coefficient for a Combustion
%chamebr gas to wall to coolant set.
%h_gc = gas side thermal conductance
%t = chamber wall thickness (assumed to be constant)
%k = thermal conductivity of chamebr wall
%h_c = thermal conductance of the coolant

%MODERN ENGINEERING FOR DESIGN OF LIQUID-PROPELLANT ROCKET ENGINES (pg. 89)

H=1/((1/h_gc)+(t/k)+(1/h_c) );%Overall thermal conductance of the system
end
```

12.5.3 Mass flow Rate Calculation from Thrust

```
function [Mdot] = Mdot_Thrust(F,M,Tc,Pe,Pc,k)
%This function determines mass flow rate from the thrust and engine
%conditions
```

```
%F=Thrust[N]
%M=molar mass[g/mol]
%Tc= combustion temperature [K]
%Pe/Pc=ratio of combustion pressure to exit pressure
%k=ratio of specific heats


M=M/1000;%[kg/mol]
R_=8.314;%[J/(mol*K)]
R=R_/M;%[J/(kg*K)]
Mdot=F/( sqrt( 2*k/(k-1)*R*Tc*(1-(Pe/Pc)^((k-1)/k)) ) );%[kg/sec]
end
```

12.5.4 Bernoulli's Equation Solver

```
%Alec Bluhm
%Bernoulli solve
%5/17/2021

clear;
close all;
clc;
P1=800*6894.76;%[Pa]
P2=linspace(P1*(9/10),P1,1000);
rho=851.4;%[kg/m3]
for i=1:length(P2)
 Del_P(i)=P1-P2(i);%[Pa]
 Del_P_(i)=(P1-P2(i))/6894.76;%[psi]
 V2(i)=sqrt(((Del_P(i))*2)/rho);%[m/s]
end
figure
plot(Del_P_,V2)
grid on
xlabel('Change In Pressure [Psi]')
ylabel('Injection Velocity [m/s]')
```

```
title('Bernoulli"s equaiton Solution for fluid velocity vs Pressure Drop')
```

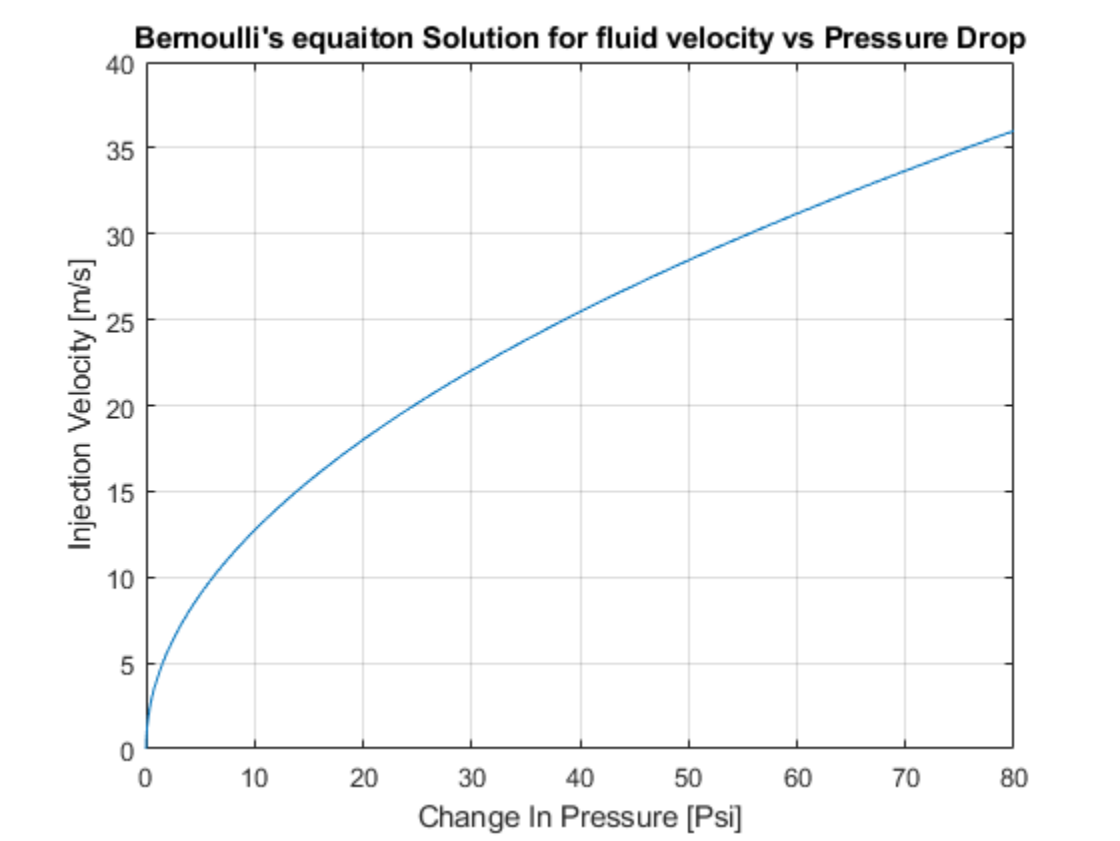

12.5.5 Antonie's Equation

```
function [P_fs,P_fs_H2O,P_fs_eth]=Antoine(Mix,T_s)
%Estimates fuel droplet vapor pressure
%Mix= mixture raito by mass
%A,B,C == constants derived for use in this equation
%T_s == droplet surface temperature input:[K]
%NOTE: using a lumped model, the surface temperature will also be the
%internal temperature
%P_fs== pressure on fuel surface [mmHg]


T_s=T_s-273;%[C] converts kelvin input to Celcius

if T_s<77 || T_s>243
 warning ('Temperature out of range for ethanol input')
 flag=1;
end
if T_s<99 || T_s>374
 warning ('Temperature out of range for water input')
 flag=1;
end
%Constants source:
```

```
%http://ddbonline.ddbst.com/AntoineCalculation/AntoineCalculationCGI.exe?component=Ethanol
%http://ddbonline.ddbst.com/AntoineCalculation/AntoineCalculationCGI.exe?component=Water
A_eth=7.68117;
B_eth=1332.04;
C_eth=199.2;
A_H2O=8.14019;
B_H2O=1810.94;
C_H2O=244.485;

A=A_eth*Mix+A_H2O*(1-Mix);
B=B_eth*Mix+B_H2O*(1-Mix);
C=C_eth*Mix+C_H2O*(1-Mix);

P_fs_eth=10^(A_eth-B_eth/(C_eth+T_s));%[mmHg]
P_fs_H2O=10^(A_H2O-B_H2O/(C_H2O+T_s));%[mmHg]
P_fs=10^(A-B/(C+T_s));%[mmHg]
end
```

12.5.6 Fluid Characteristics equations

```
function [Re] = Reynold(rho,V,D,mu)
%Calculates the reynolds number of a fluid in a pipe
%rho = fluid denisty [kg/m3]
%V = fluid velocity [m/s]
%D = pipe diamter [m]
%mu = fluid dynamic viscosity [kg/(m*s)]
Re=(rho*V*D)/mu;
end

function [Pr] = Prandtl(mu,Cp,k)
%Solve for the prandtl number of a fluid
%mu = dynamic viscoisty
%Cp = specific heat at constant pressure
%k = thermal conductivity

Pr=(mu*Cp)/k;
end

function [Sc] = Schmidt(mu,rho,D)
%Solves for the Schidt number of a fluid
%mu = Dynamic viscosity
%rho = fludi density
%D = Diffusivity
Sc=mu/(rho*D);
end

function [We] = Weber(rho,v,L,sigma)
%rho== density
%v== velocity
%L== characeristic length (droplet diameter)
%sigma== surface tension
```

```
We=rho*v^2*L/sigma;%[unitless]
end
```

12.6 Solidworks Models

The following are images of the created Solidworks model for the system designed in the thesis.

12.6.1 Full Assembly

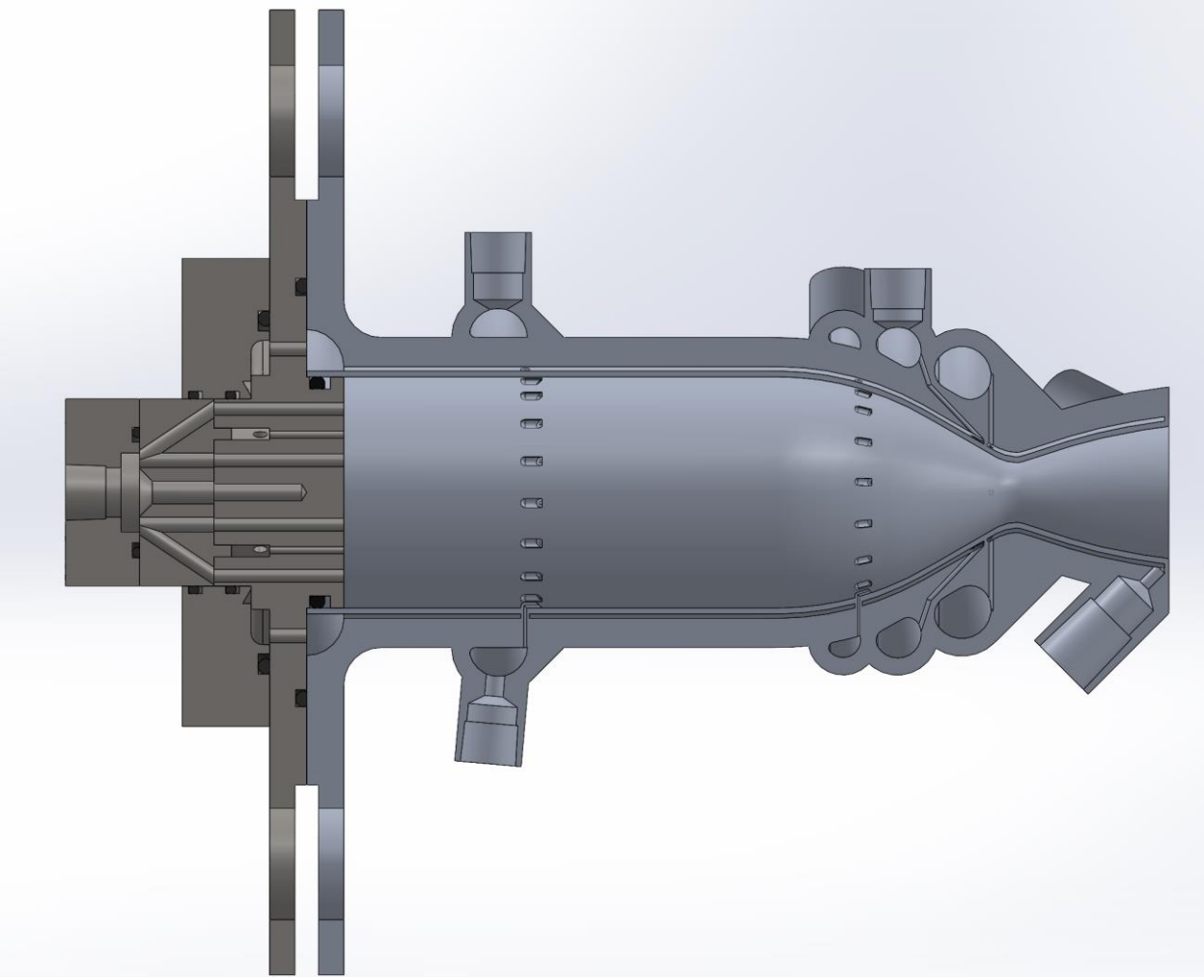

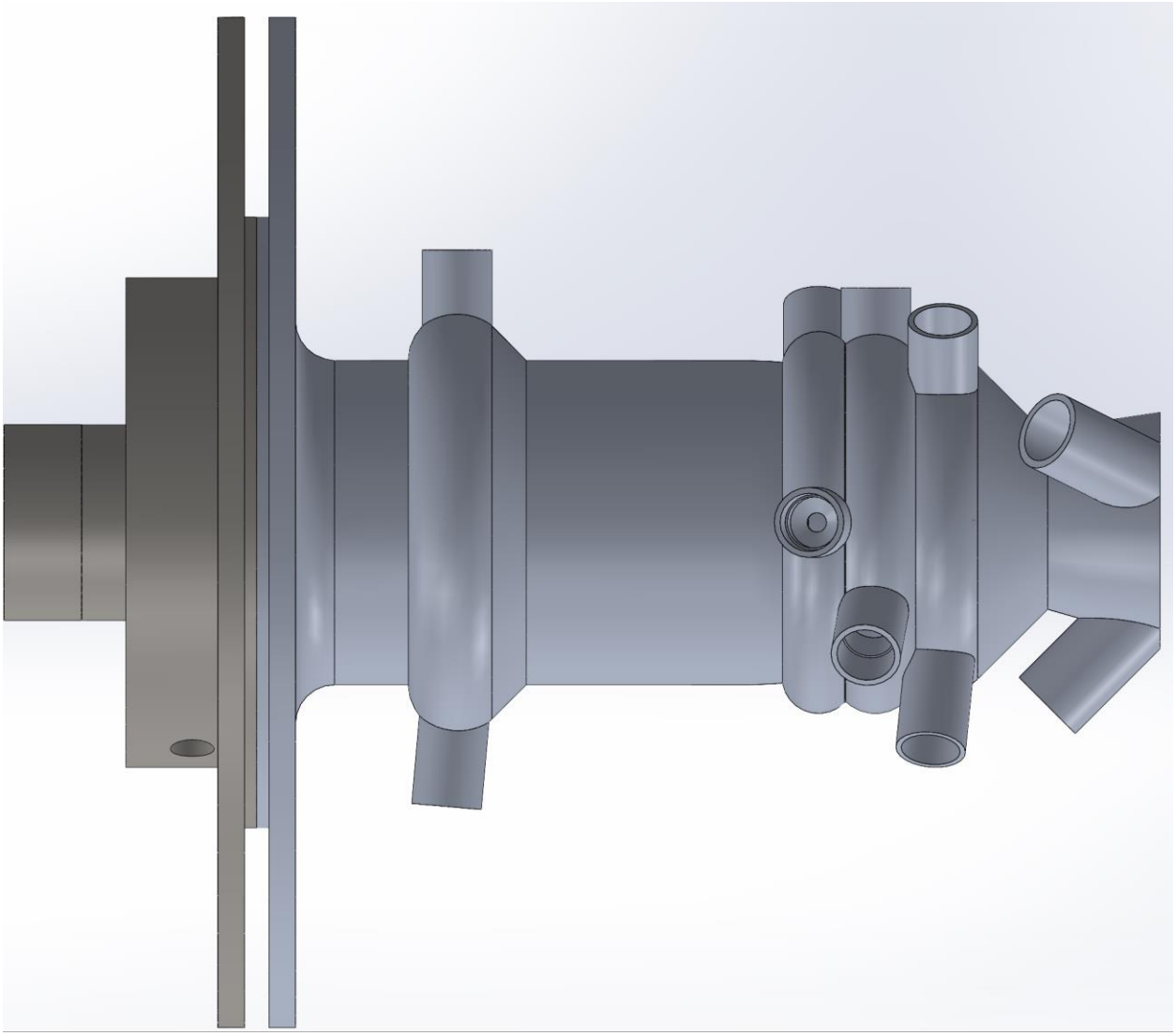

12.6.2 Injector Plate

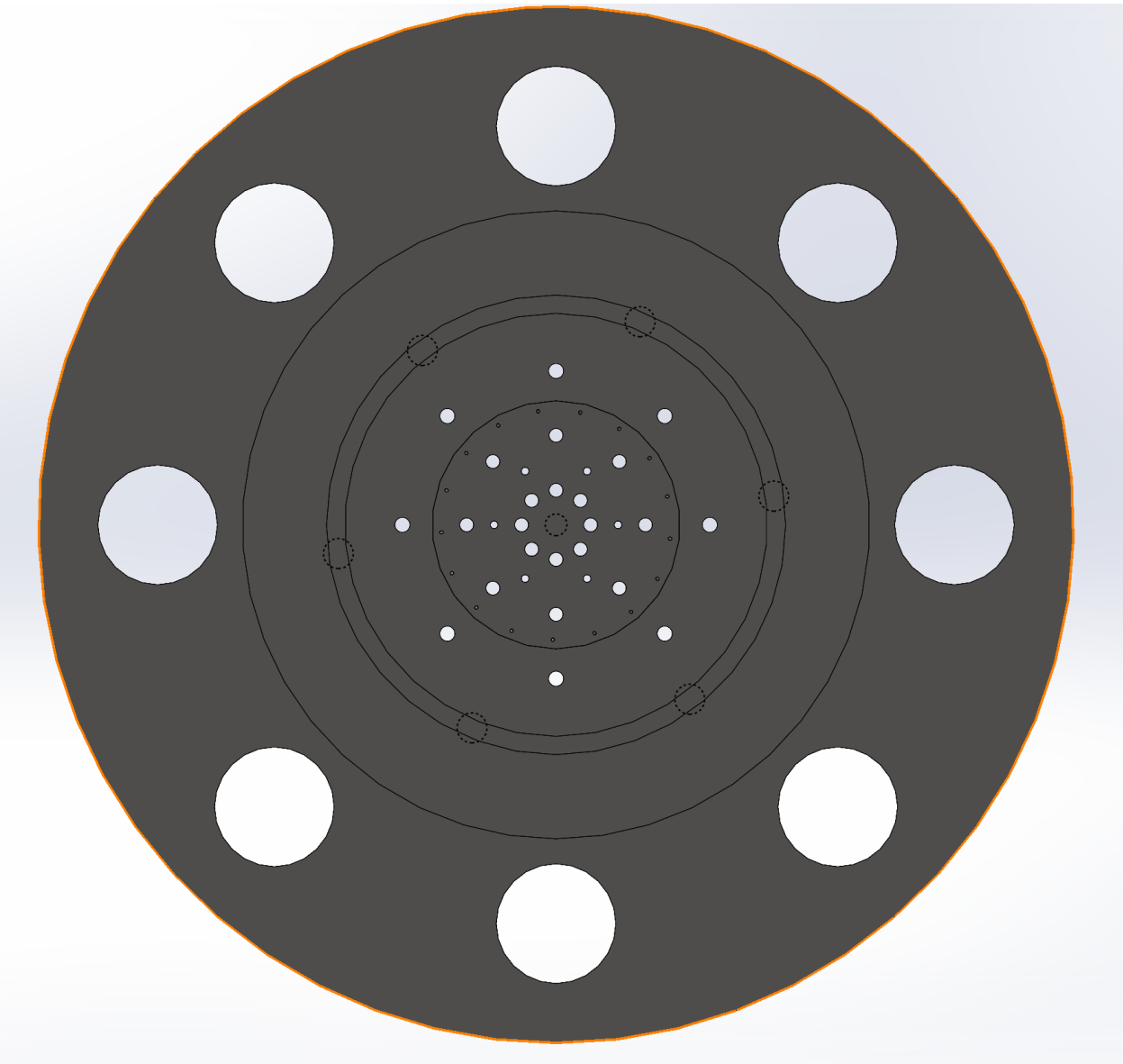

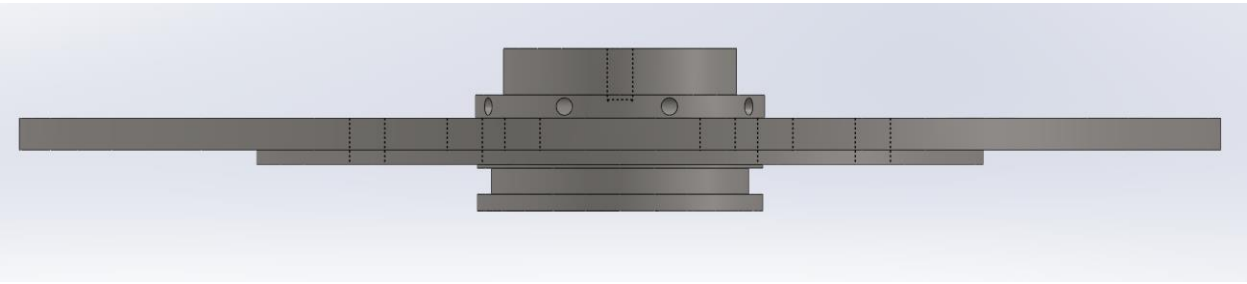

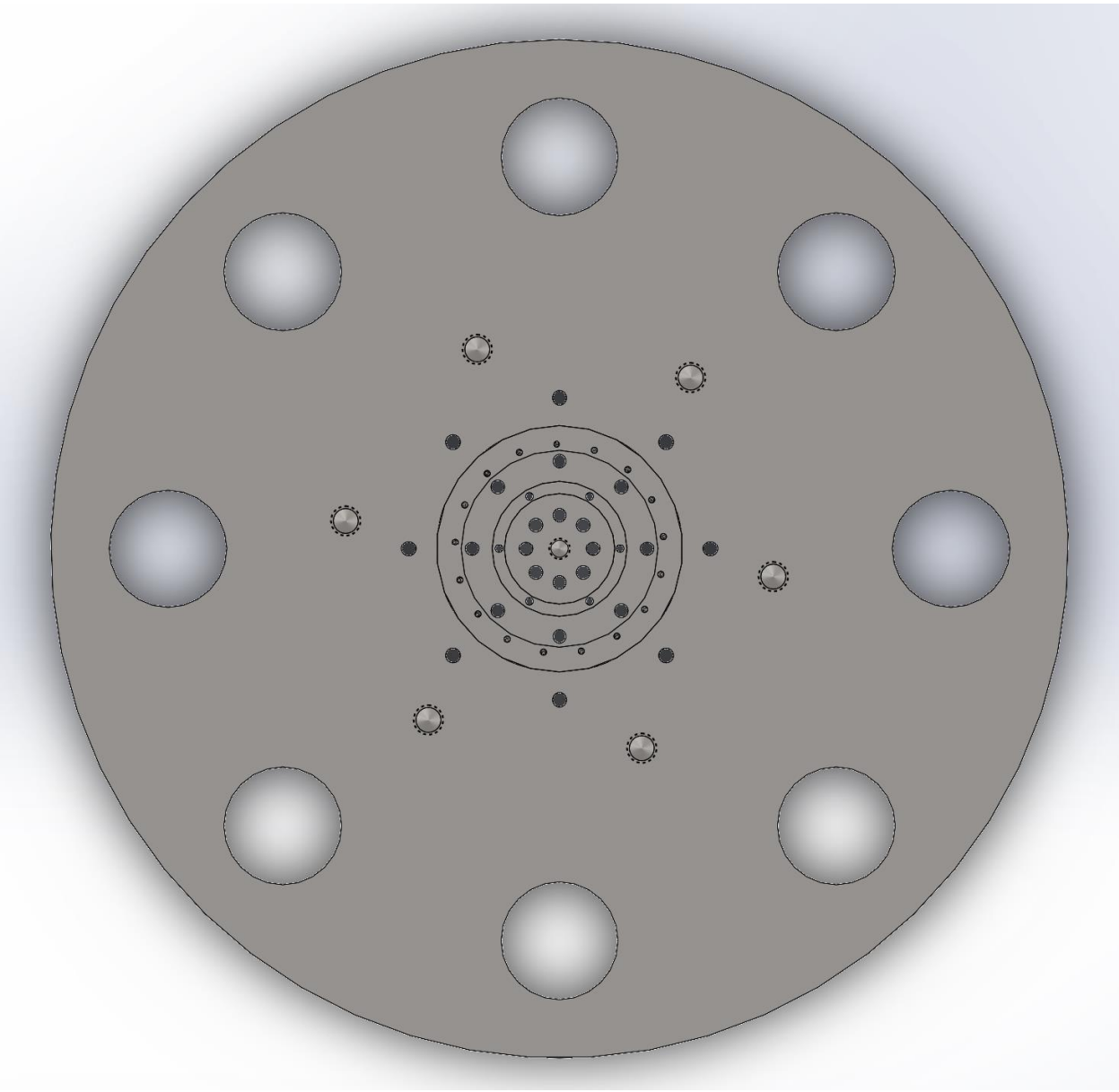

12.6.3 Film Coolant Manifold

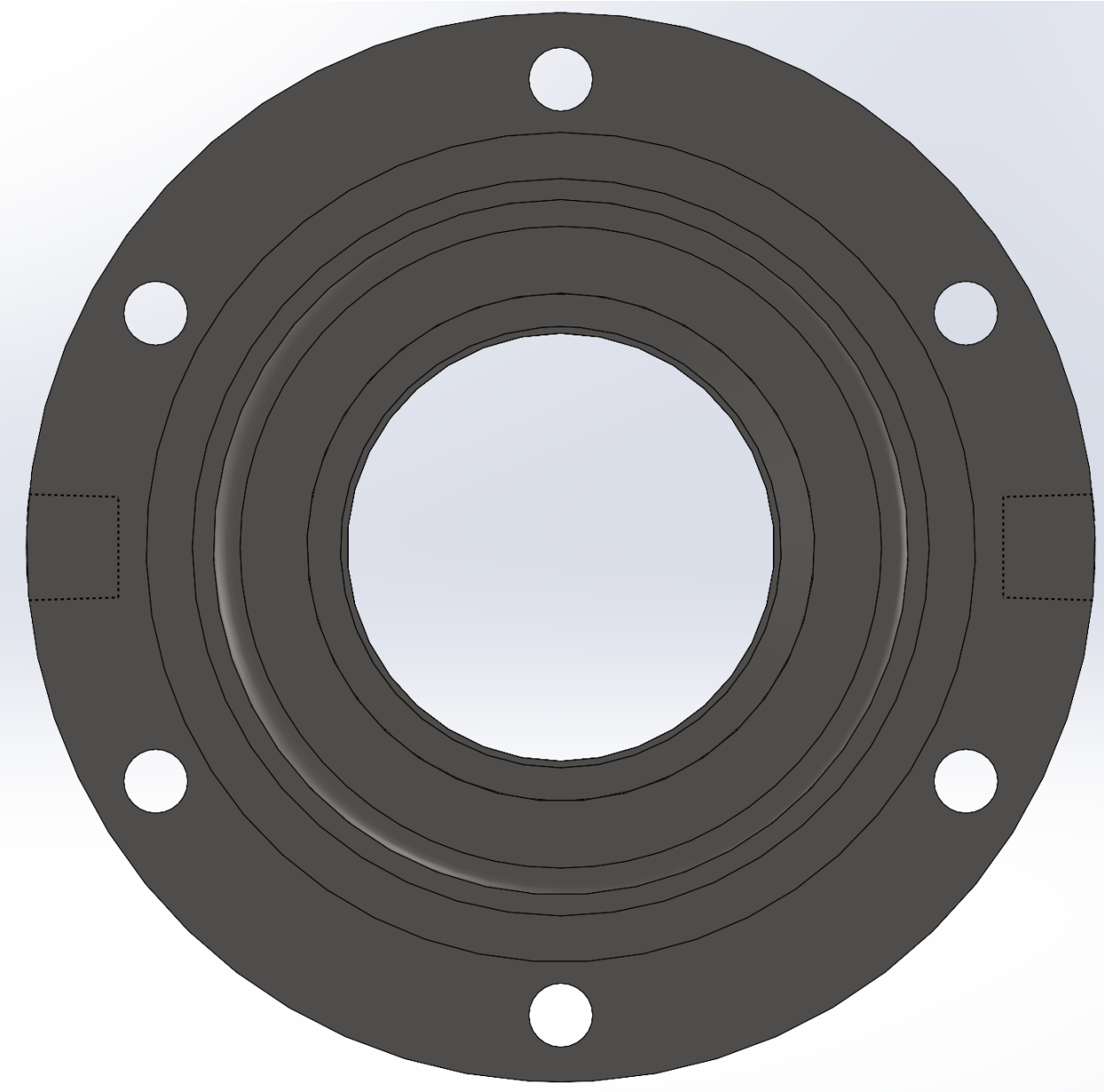

12.6.4 N_2O Manifold Part 1

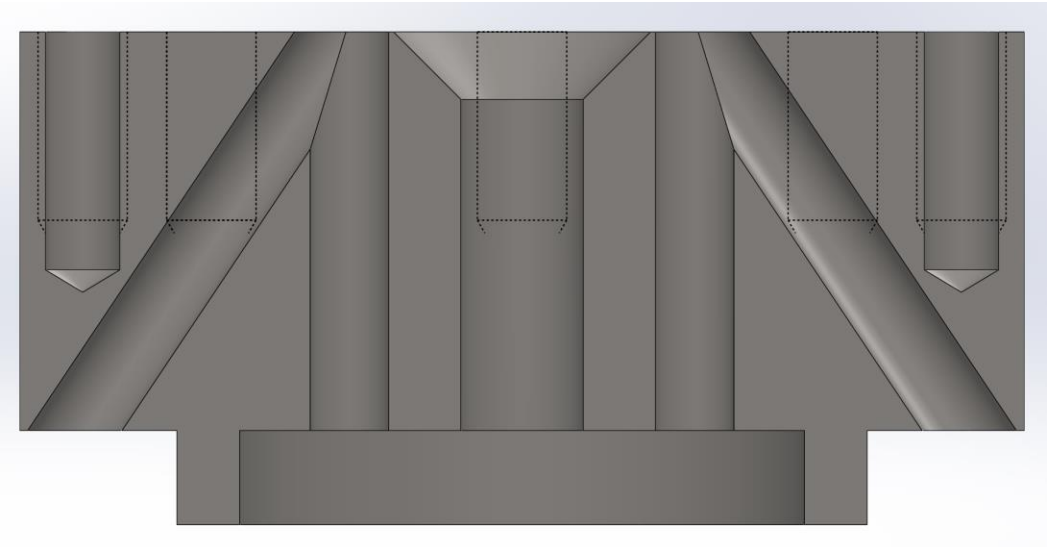

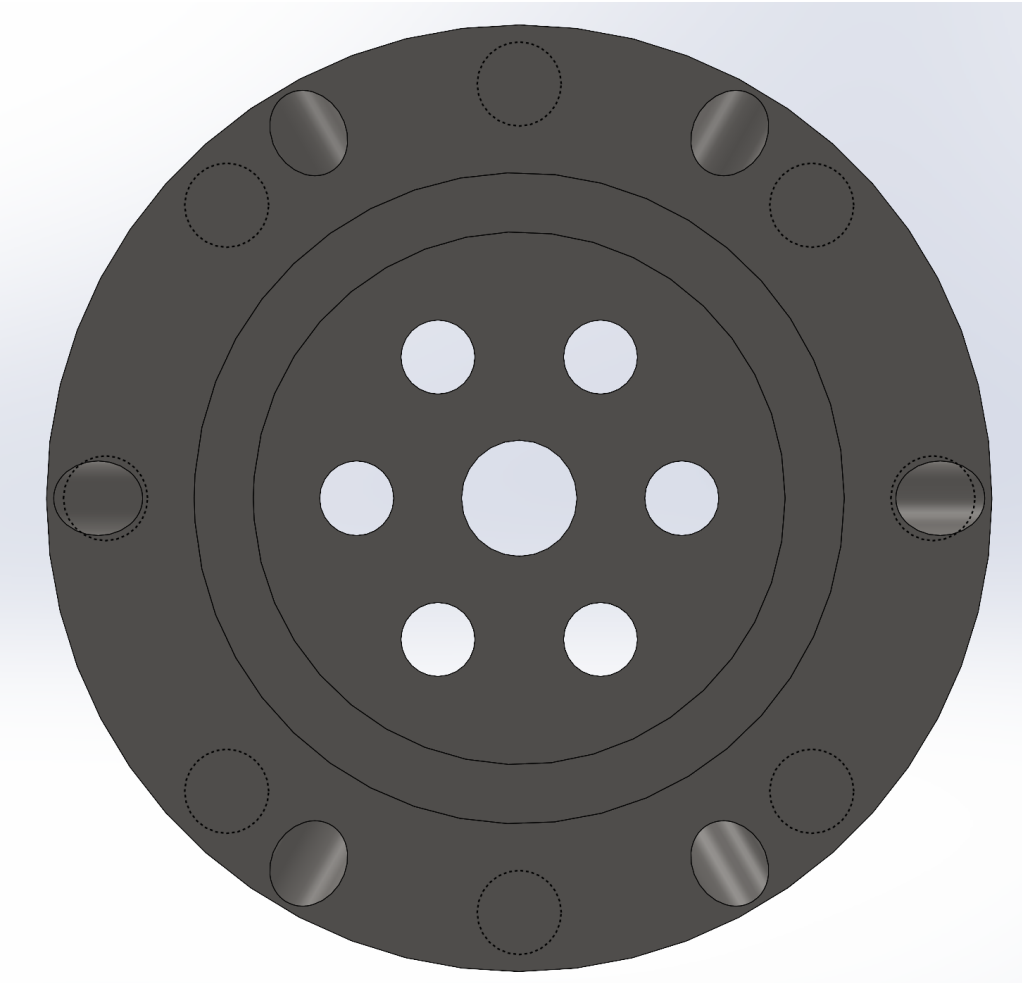

12.6.5 N_2O Manifold Part 2

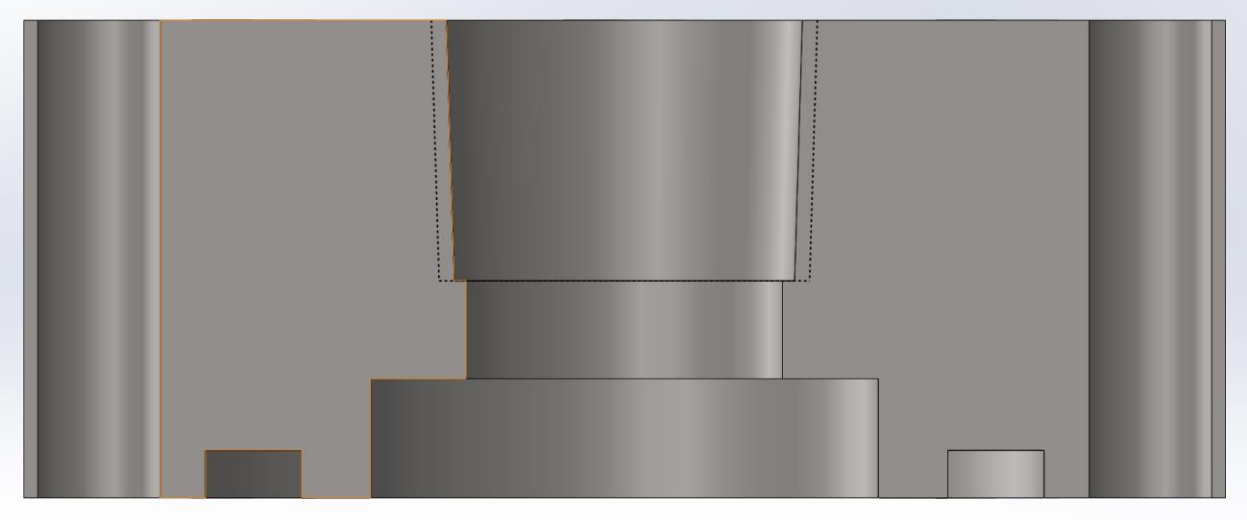

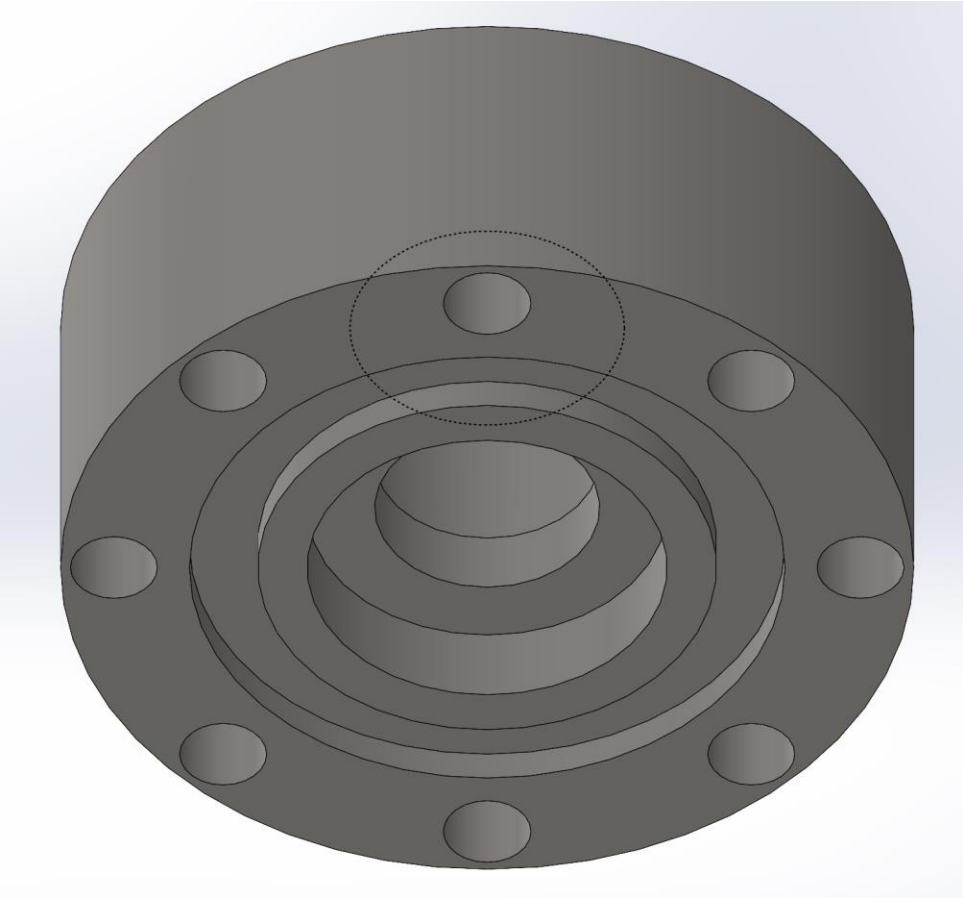

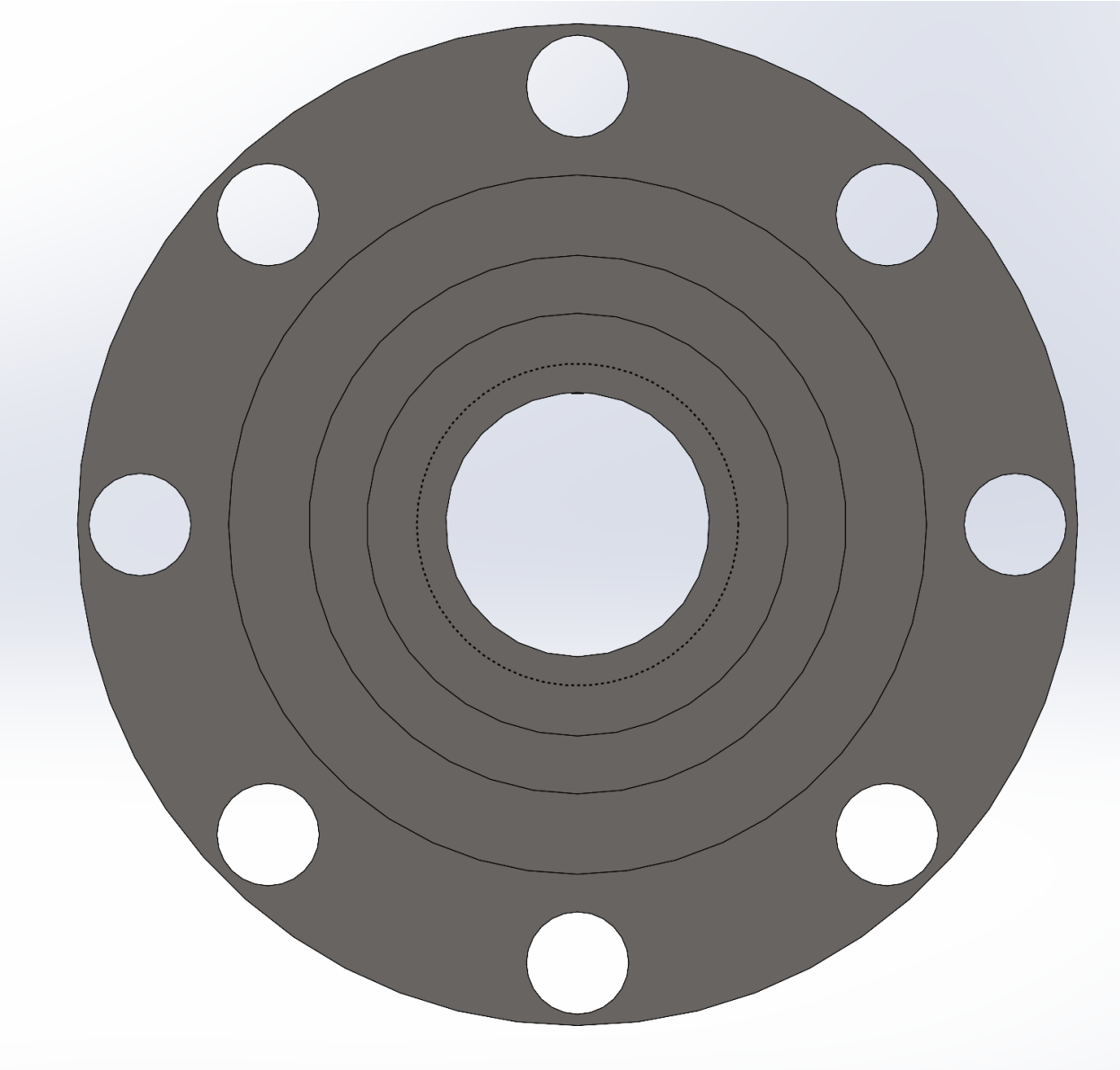

12.7 Plumbing Diagram

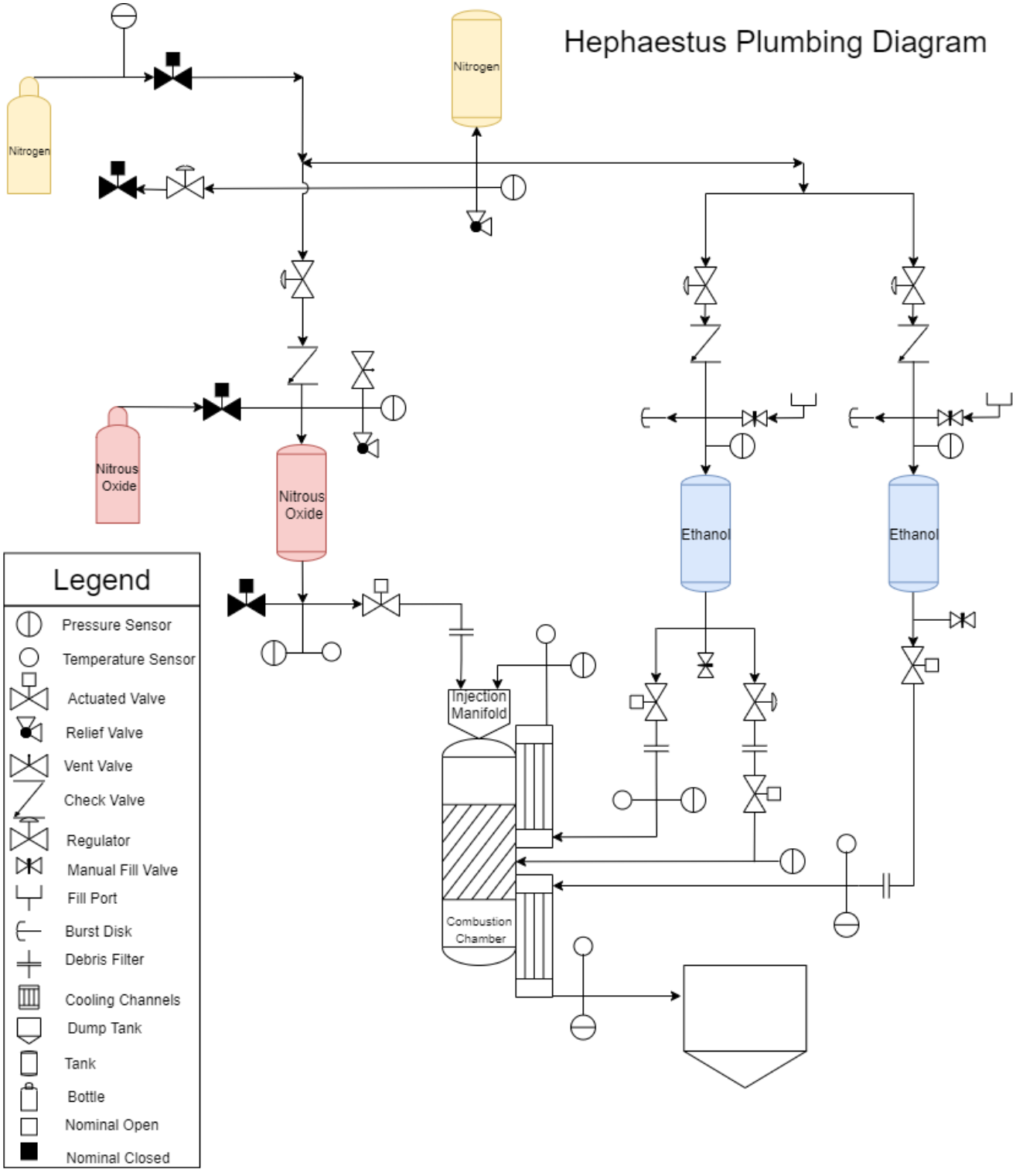

12.8 Design Process Flowchart

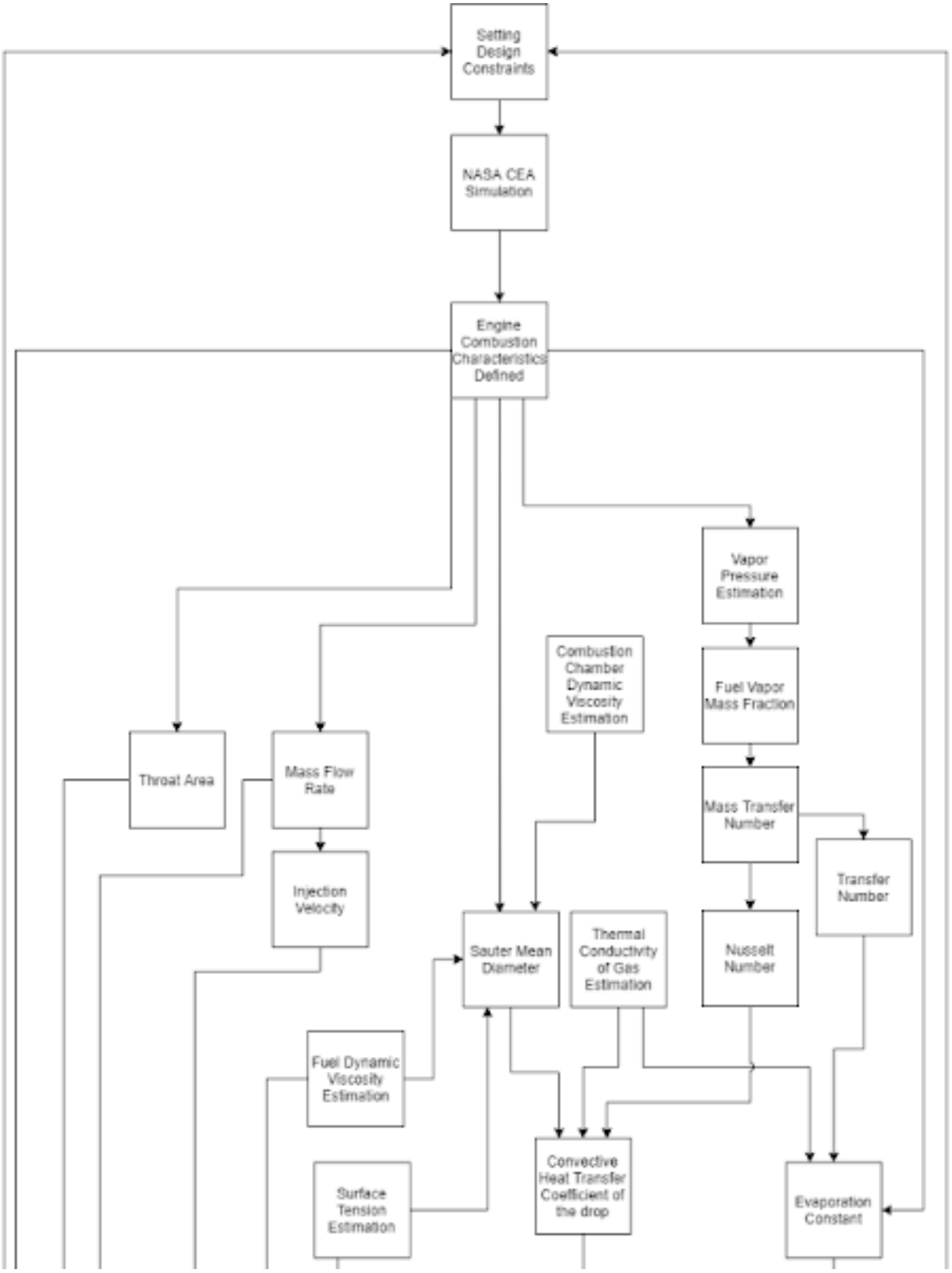

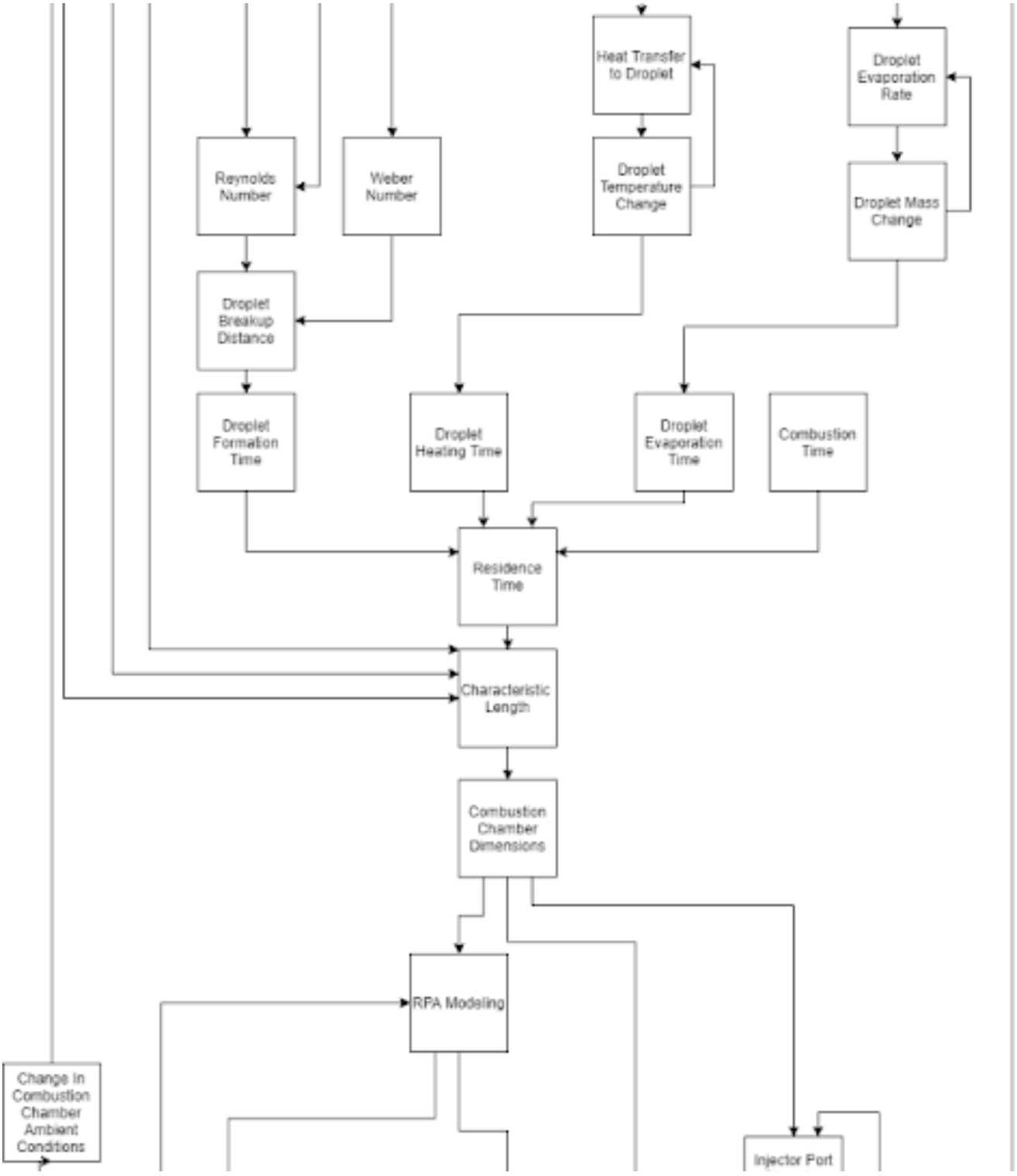
Heat Transfer to Droplet
Droplet Evaporation Rate
Reynolds Number
Weber Number
Droplet Temperature Change
Droplet Mass Change
Droplet Breakup Distance
Droplet Formation Time
Droplet Heating Time
Droplet Evaporation Time
Combustion Time
Residence Time
Characteristic Length
Combustion Chamber Dimensions
RPA Modeling
Change in Combustion Chamber Ambient Conditions
Injector Port

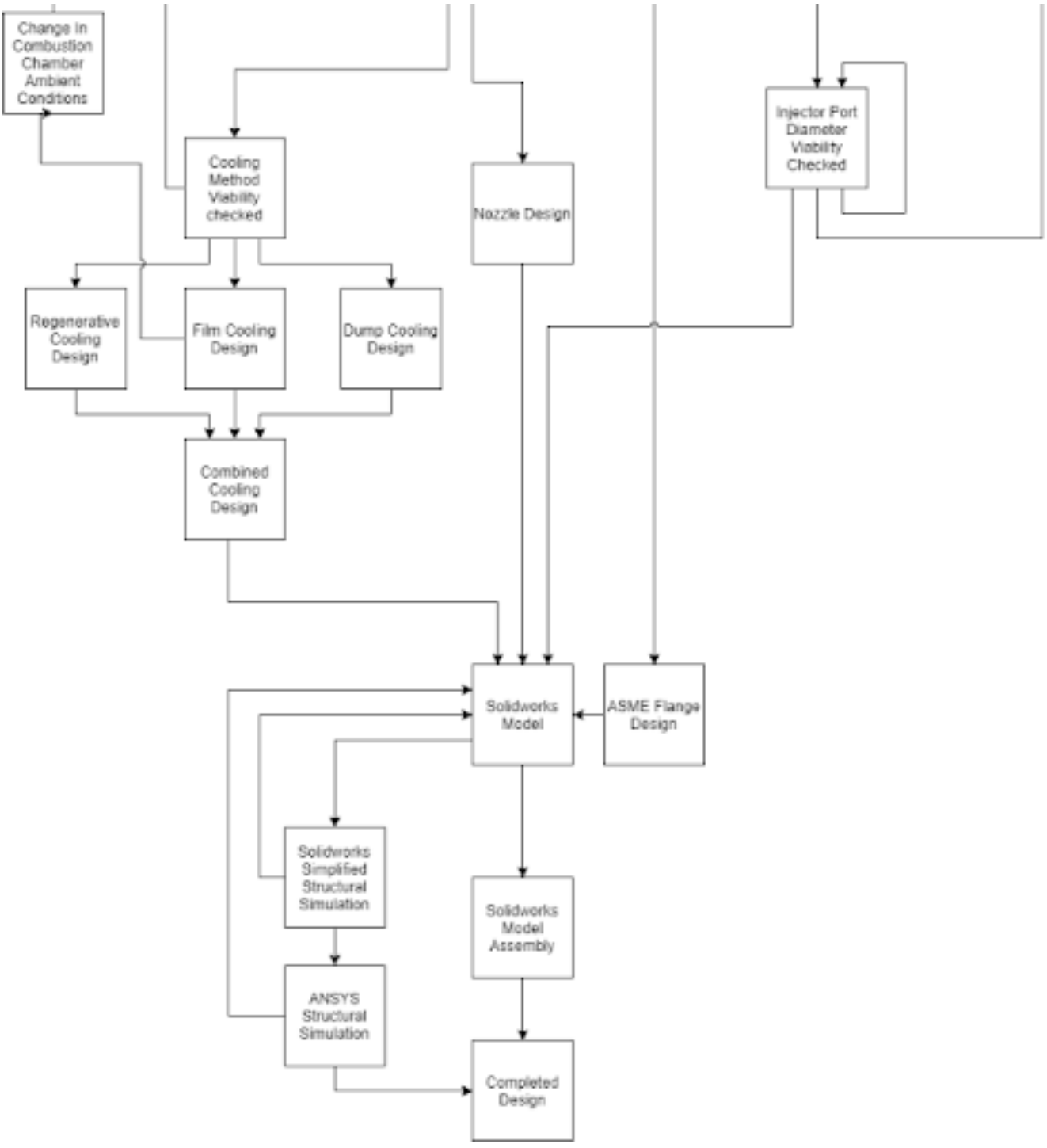
Change In Combustion Chamber Ambient Conditions
Cooling Method Viability checked
Nozzle Design
Injector Port Diameter Viability Checked
Regenerative Cooling Design
Film Cooling Design
Dump Cooling Design
Combined Cooling Design
Solidworks Model
ASME Flange Design
Solidworks Simplified Structural Simulation
Solidworks Model Assembly
ANSYS Structural Simulation
Completed Design